A NUMERICAL STUDY OF BUBBLE DEFORMATION IN STEADY AXISYMMETRIC FLOWS

Thesis by

Gregory Ryskin

In Partial Fulfillment of the Requirements

for the Degree of

Doctor of Philosophy

California Institute of Technology

Pasadena, California

1983

(Submitted January 11, 1983)

Acknowledgments

I wish to express my gratitude to my adviser, Professor L. Gary Leal; I would like also to thank the faculty members and students in Chemical Engineering and Applied Mathematics, communication with whom was helpful in my work.

Abstract

This work is devoted to the development and application of the numerical technique suitable for solution of the free-boundary problems, i.e. those in which the shape of the boundary should be determined as a part of the solution. The technique is based on a finite-difference solution of the equations of the problem on an orthogonal curvilinear coordinate system, which is also constructed numerically and always adjusted so as to fit the current boundary shape. The same orthogonal mapping approach may also be used to construct orthogonal coordinates fitted to boundaries of known but complicated shapes.

The technique is applied to two classical problems of fluid mechanics -- deformation of a gas bubble rising through a quiescent fluid due to buoyancy, and deformation of a gas bubble in a uniaxial extensional flow. For the rising bubble, the shapes and flow fields are computed for Reynolds numbers $1 \leq R \leq 200$ and Weber numbers up to 20 at the lower Reynolds numbers and up to 10 at Reynolds numbers 50, 100 and 200. The most interesting results of this part are those demonstrating the phenomenon of flow separation at a smooth free surface. This phenomenon does not appear to have been theoretically predicted before, in spite of its importance for understanding the mechanics of free-surface flows.

In the case of a bubble in a uniaxial extensional flow, the computations show that at Reynolds numbers of order 10 and higher the deformation of a bubble proceeds in a way qualitatively different from the low Reynolds number regime studied previously; the bubble bursts at a relatively early stage of deformation never reaching the highly elongated

shapes observed and predicted at low Reynolds numbers. It is shown also that for this problem the solution at Reynolds number of order 100 is already quite close to the potential flow solution which can be easily obtained using the present technique.

Table of Contents

Table of Contents (continued)

Table of Contents (continued)

Introduction

Free boundary problems, i.e. those in which the shape of the boundary is not known in advance but should be determined as a part of the solution, are abundant in chemical engineering. The classical examples of such problems are found in fluid mechanics where the free boundary is usually a gas-liquid or liquid-liquid interface. This class of problems is becoming tractable now, with the advent of the computer. Most of the published work in the field has been based on the finite-element discretization of the domain of solution. The present study offers an alternative approach in which the equations of the problem are written in a curvilinear orthogonal coordinate system, always adjusted so as to fit the current boundary shape, and then solved by a finite-difference technique. The orthogonal coordinate system is also constructed numerically, using the technique of orthogonal mapping described in Chapter 1. It should be noted that this technique may also be used to construct boundary-fitted orthogonal coordinates in cases when the shape of the boundary is known but does not conform to classical coordinates of mathematical physics (Cartesian, cylindrical, spherical, ellipsoidal, etc.). Problems of this type are, of course, even more ubiquitous than the free boundary ones.

The rest of the present work is devoted to application of this technique to a classical problem of fluid mechanics — deformation of a gas bubble in a fluid flow. Gas bubbles are encountered in many technological processes and their behavior has been the subject of

numerous investigations; however, only limited theoretical understanding could be achieved without a technique capable of predicting large deformations in nonlinear flows (the creeping flow regime can be efficiently investigated by the boundary-integral technique). The present technique is limited to axisymmetric problems; two of the more interesting cases in this category — a bubble rising through a quiescent fluid under the action of buoyancy and a bubble in uniaxial extensional flow — are investigated here.

Chapter 2 contains an overview of the application of orthogonal mapping to free-surface problems, with the emphasis on implementation of stress boundary conditions. Namely, in the vorticity-stream function formulation adopted here the condition of zero tangential stress is used to obtain the boundary values of vorticity at the interface, while the balance between normal stress and surface tension forces is used to drive the shape of the free surface to its equilibrium configuration.

In Chapter 3 the results for the rising bubble problem are presented and discussed. These include the drag, the bubble shape and the details of the velocity field for Reynolds numbers from 0.5 to 200 and Weber numbers up to 20 at the lower Reynolds numbers and up to 10 at Reynolds number equal to 50, 100 and 200. Perhaps the most interesting results of this chapter are those demonstrating the phenomenon of flow separation at a smooth free surface. This phenomenon does not appear to have been theoretically predicted before, in spite of its importance for understanding the mechanics of free-surface flows.

The problem of a bubble in a uniaxial extensional flow is treated in Chapter 4. The computations show that at Reynolds numbers of order

10 and higher the deformation of a bubble proceeds in a way qualitatively different from the low Reynolds numbers regime that has previously been studied in the creeping flow limit by G. I. Taylor, A. Acrivos and others; the bubble bursts at a relatively early stage of deformation, never reaching the highly elongated shapes observed and predicted at low Reynolds numbers. It is shown also that for this problem the solution at Reynolds number of order 100 is already quite close to the potential flow solution which can be easily obtained using the present technique.

CHAPTER I

Orthogonal Mapping

by

G. Ryskin and L. G. Leal

Department of Chemical Engineering
California Institute of Technology
Pasadena, California 91125

J. Comput. Phys. (in press)

Abstract

A technique of orthogonal mapping is proposed for constructing boundary-fitted *orthogonal* curvilinear coordinate systems in 2D. The mapping is defined by the *covariant* Laplace equation, and constraints on the components of the metric tensor of the curvilinear coordinates are used to achieve orthogonality and to control the spacing of coordinate lines. Two different methods of implementing the mapping are presented. The first, termed the *strong constraint* method, is intended primarily for problems in which the boundary shape is not known in advance, but is to be determined as a part of the solution (e.g. free boundary problems in fluid mechanics). The second, termed the *weak constraint* method, is designed for the construction of an orthogonal mapping with a *prescribed boundary correspondence*, i.e. the production of boundary-fitted orthogonal coordinates for a domain of given shape with a prescribed distribution of coordinate nodes along the boundary.

The method is illustrated by numerical examples, and it is shown that the problem of mapping infinite domains can be treated by mapping the infinite domain onto a finite one using a simple conformal transformation and then applying the orthogonal mapping technique developed here to the finite domain. The possibility of obtaining analytical solutions for the mapping functions is discussed. The Appendices contain connection (Christoffel) coefficients which provide a convenient means for deriving equations of a physical problem for the constructed coordinates in terms of physical components, using a slight extension of Cartesian tensor notation.

1. Introduction

The construction of a curvilinear coordinate system in which a boundary of arbitrary shape is represented by a coordinate line or surface is an important problem of applied mathematics. The best-known approach to this problem is typified by the method of Thompson *et al.* [1,2], who also review previous research. In Thompson *et al.*'s method [2], the transform relations $\xi(x,y)$ and $\eta(x,y)$ between Cartesian coordinates x,y and "boundary-fitted" curvilinear coordinates ξ,η, are assumed to satisfy elliptic equations of the form

$$\frac{\partial^2 \xi}{\partial x^2} + \frac{\partial^2 \xi}{\partial y^2} = P(\xi,\eta)$$

$$\frac{\partial^2 \eta}{\partial x^2} + \frac{\partial^2 \eta}{\partial y^2} = Q(\xi,\eta) \qquad (1)$$

where the functions $P(\xi,\eta)$ and $Q(\xi,\eta)$ are chosen (essentially by trial and error) to control the spacing and configuration of coordinate lines in the domain of interest. It is suggested that "sums of decaying exponentials" provide a convenient form for P and Q, but the choice is otherwise *ad hoc*. To actually carry out the transformation, a set of coupled, nonlinear partial differential equations is derived for $x(\xi,\eta)$ and $y(\xi,\eta)$ from (1) by direct interchange of dependent and independent variables, and these equations are then solved numerically. Though undoubtedly useful, Thompson *et al.*'s approach has the severe drawback, when applied to the numerical solution of differential equations from mathematical physics, of yielding a *nonorthogonal* coordinate system. In addition, the only control over spacing and configuration of coordinate lines is exercised by the *ad hoc* choice of $P(\xi,\eta)$ and $Q(\xi,\eta)$.

We consider the development of a method to generate orthogonal (boundary-fitted) coordinates. With this objective, the first and classical candidate in 2D is, of course, conformal mapping. Indeed, efficient methods for numerical construction of

conformal mappings have been developed (see [3,4] and references therein); however, as Fornberg [3] points out, conformal mappings are ill-conditioned in the sense that very small changes in the shape of the domain can dramatically alter the position of mapped boundary points. Also, the density of boundary points (placed uniformly in the ξ,η plane) may vary by several orders of magnitude along the boundaries of the original x,y domain. Examples given by Fornberg [3] (see Figs. 1 and 7 of his paper) show clearly that conformal mapping can yield coordinate grids which are completely unsuitable for numerical solution of partial differential equations.

The problem with conformal mapping is that the ***dual*** requirements of orthogonality and equality of the scale factors (so that a small square in the ξ,η plane is mapped onto a square in the physical x,y plane) are too restrictive. Hung and Brown [5] and Pope [6] have attempted to alleviate this problem by constructing orthogonal mappings in which the ratio of scale factors is not unity but rather some (adjustable) constant throughout the domain. However, the use of a constant ratio of scale factors is still too restrictive for a generally applicable transformation technique, and Mobley and Stewart [7] have thus suggested construction of an orthogonal mapping by nonuniform stretching of the conformal coordinates. The coordinates of Mobley and Stewart are thus a pair of variables, each of which is a monotonic function of a respective conformal variable. By eliminating the "intermediate" conformal variables, Mobley and Stewart obtained generating equations for their transformation functions. As will be seen in sections 2 and 4, this procedure can lead to basically the same types of grids as the "strong constraint" subclass of the present method and the generating equation of Mobley and Stewart is just a covariant Laplace equation, though this important fact could not be recognized in the framework of their approach. Most recently, Haussling and Coleman [8] have attempted to produce orthogonal coordinate grids in two dimensions with prescribed nodal correspondence on all boundaries, using a pair of differential constraints on the mapping functions $x(\xi,\eta)$, $y(\xi,\eta)$ which are equivalent to

our orthogonality constraint $g_{12} = 0$ (see section 2 below). The single constraint of orthogonality is, however, insufficient to completely specify a mapping in two-dimensions, and the resulting procedure exhibits a number of problems including nonorthogonal mesh. One example, which is treated successfully by the method outlined in the present paper (see Figs. 7 and 8), led to a completely unacceptable mesh in Haussling and Coleman [8].

Other recent attempts to construct orthogonal coordinates have been based on solving first order partial differential equations of the Cauchy-Riemann type as an initial value problem. Starius [9] used this idea to construct an orthogonal coordinate mesh in a strip near a given boundary, but was forced to use a different grid in the interior of his domain with interpolation between the two grids then required in the region of overlap. Following an earlier approach by Potter and Tuttle [10], Davies [11] used the same idea to construct a second set of coordinate lines orthogonal to a first set which was to be specified on an *a priori* basis, e.g. a set coincident with pathlines of the fluid in a semi-Lagrangian code. However, the application of this initial value approach is not generally suitable for the construction of a coordinate system for the complete domain, since it is usually necessary to specify conditions on all boundaries, and the generating equation should thus be elliptic.

In the present paper, a "covariant" approach is suggested for the generation of orthogonal mappings. Simple considerations from vector and tensor analysis are used in section 2 to establish the *covariant* Laplace equation as the generating elliptic equation for the transformation functions $x(\xi,\eta)$ and $y(\xi,\eta)$. The properties of the resulting coordinate system are then determined by constraints on the components of its metric tensor. We consider three types of application. In the first, the boundary shape is to be determined as part of the solution of the problem, and we develop the so-called "strong constraint method" to determine the mapping. This case is discussed in section 4. In the second type of application, the shape of the domain is known, and in the

third, the spacing of boundary nodes is also specified, i.e. the complete boundary correspondence is prescribed. For these cases, we have developed the "weak constraint method", which is discussed in section 5. Finally, a brief comparison with the classical method of conformal mapping is given in section 6. A preliminary presentation of our technique of orthogonal mapping was given in [12], and an application of the "strong constraint method" to calculate the shapes of gas bubbles rising through a viscous fluid is summarized in [13].

2. Equations Defining the Mapping

A most important first step in the development of a mapping between a Cartesian and a "boundary-fitted" curvilinear coordinate system is to determine the equations to be satisfied by the transform functions $x(\xi,\eta)$ and $y(\xi,\eta)$. Fortunately, this is extremely simple even if the resulting "boundary-fitted" coordinates are required to have predetermined properties such as orthogonality, provided the well-known covariant point of view is adopted, according to which any physical or geometrical law must be expressible in a form that does not depend on the choice of a particular coordinate system (see, e.g. section 12.5 of [14]).

In particular, a covariant, coordinate-free form of the equations for x and y follows directly from the trivial observation that x, as a Cartesian coordinate in the physical space, is obviously a linear scalar function of position and the same is true of y. Thus, grad(x) and grad(y) are constant valued vector fields, and it follows that

$$\text{div grad}(x) = 0$$

$$\text{div grad}(y) = 0 \qquad (2)$$

everywhere, with div grad being the covariant Laplace operator ∇^2. As is well known, this operator can be written in explicit form for any particular coordinate system ξ^1,ξ^2,

including the one we want to construct, provided only that we know the components of the metric tensor $g_{\alpha\beta}$ which define the length of a line element according to the relation

$$ds^2 = g_{\alpha\beta} d\xi^\alpha d\xi^\beta \ .$$

Here, the Greek indices equal 1 or 2 in 2D and summation on the repeated indices is implied.

The obvious question, then, is how the metric tensor is to be determined before the coordinate system is constructed. The answer is that the development of an appropriate coordinate transformation must begin by specifying the metric tensor — and it is this specification which determines the properties of the resulting coordinate system. For example, if the nondiagonal components of $g_{\alpha\beta}$ are zero, the coordinate system ξ^1,ξ^2 is orthogonal. If, in addition, the diagonal components are all equal to 1, the system is Cartesian, etc. Now, whatever physical problem is being considered, there are always m *degrees of freedom* (where m = 2 in 2D and m = 3 in 3D) in choosing the mapping functions [e.g. the functions $x(\xi,\eta),y(\xi,\eta)$ in 2D]. The essential idea pursued in the remainder of this paper is to "use" these available degrees of freedom to impose m constraints on the components of the metric tensor in order to build the desired properties into the constructed coordinate system.

Although the metric tensor (being symmetric) generally has three independent components in 2D (and six in 3D), the m constraints referred to above are the maximum number that can be imposed if the space described by the resulting coordinate system is to be *Euclidean* ("flat"). Mathematically, the condition that the space is Euclidean is equivalent to requiring the Riemann curvature tensor of the coordinate system to be zero (see [14]). The Riemann tensor, which is a function of the metric tensor and its first and second derivatives, has only one independent component in 2D (which is proportional to the Gaussian curvature), and the restriction to a Euclidean space thus

imposes a single constraint on $g_{\alpha\beta}$, reducing the number of freely specifiable constraints to two. In 3D, the Riemann tensor has six independent components, but they are linked by the differential *Bianchi identities* (see [14]), leaving only three "flatness" constraints on the metric tensor. Consequently, the number of freely specifiable constraints on $g_{\alpha\beta}$ in 3D is three. Note that an explicit consideration of the "flatness" constraints is not necessary. If a solution of Eqs. (2) exists (thus defining a transformation from ξ,η to the Cartesian coordinates x,y), the space described by ξ,η is guaranteed to be Euclidean because Cartesian coordinates may be introduced only in a Euclidean space. In other words, the condition that the Riemann tensor be zero is just a condition of integrability for Eqs. (2) (see [15], section 39) — and so will be satisfied automatically when a solution of (2) is obtained.

It is, of course, not clear that the degrees of freedom in choosing the mapping functions $x(\xi,\eta),y(\xi,\eta)$ can always be utilized as constraints on the metric tensor. In particular, it is not evident that mapping functions can always be found connecting some particular domains in the x,y and ξ,η planes which satisfy prescribed constraints on the metric tensor. To prove that this is indeed possible for arbitrary constraints would amount to a major result in theoretical mathematics, and is beyond the scope of the present work. However, for the particular pair of constraints in 2D;

$$g_{12} = 0 \quad \text{and} \quad \frac{g_{22}}{g_{11}} = 1$$

which define conformal mapping, the proof is, in fact, well known: it is the celebrated Riemann Mapping Theorem. This fact provides some theoretical support for the present approach, though we do not restrict ourselves to conformal maps.

The most obvious (and useful) constraint in the general case is to set all of the nondiagonal components of $g_{\alpha\beta}$ equal to zero, thereby ensuring that the resulting coordinate system is orthogonal. Since the number of independent nondiagonal components is 1 in 2D and 3 in 3D, it is evident that this is always possible in two- or three-

dimensional systems. In fact, in the important 2D case, one additional degree of freedom is still left. For m > 3, on the other hand, the orthogonality constraint cannot be satisfied — an arbitrary space of more than three dimensions does not generally admit an orthogonal coordinate system — see Eisenhart [16]. We restrict our attention to orthogonal systems in two dimensions in the remainder of this paper.[1]

The metric tensor for 2D orthogonal coordinates ξ,η can be written as

$$g_{\alpha\beta} = \begin{bmatrix} h_1^2 & 0 \\ 0 & h_2^2 \end{bmatrix}$$

where index 1 corresponds to ξ, and index 2 to η. Recall now that there is one degree of freedom left in 2D after setting $g_{12} = 0$, and we propose using this to impose an additional constraint on the scale factors h_1 and h_2. A simple and useful constraint is to specify the ratio of the scale factors as a function of ξ and η, i.e. $f(\xi,\eta) \equiv h_2/h_1$. The ratio h_2/h_1 has a clear geometrical significance — it specifies the ratio of the sides of a small rectangle in the x,y plane which is an image of a small square in the ξ,η plane. It is therefore natural to call $f(\xi,\eta)$ the distortion function. By judicious choice of the distortion function, one can control the spacing of a computational grid in the x,y plane, which is the image of a uniform grid in the ξ,η plane (say, on a unit square). This should be particularly useful in problems involving disparate length scales in different directions (e.g. a boundary layer-like structure). Although the distortion function could, in principle, be adjusted automatically during the course of numerical solution to reflect the evolving gradients of the solution, such an algorithm would be expensive and has not been implemented in the current study.

The condition $f(\xi,\eta) = 1$, which corresponds to conformal mapping, is obviously a major restriction on the class of possible mappings; an adjustable function of two variables $f(\xi,\eta)$ evidently provides much greater flexibility while orthogonality is still maintained. Indeed, the "stiffness" of the conformal mapping, which makes it ill-suited for

the present purposes (see section 1), is due to this unnecessary restriction $f(\xi,\eta) = 1$. To a lesser degree, the same is true for other methods in which $f(\xi,\eta) = \text{const}$ (Hung and Brown [5], Pope [6]). We note in passing that in 3D no freedom is left after specification of the three orthogonality constraints $g_{12} = g_{13} = g_{23} = 0$, and so orthogonal mapping in 3D is likely to be as "stiff" as conformal mapping in 2D.

Equations (2) can now be written explictly in the ξ,η coordinates using the conditions

$$g_{12} = 0$$

$$\frac{h_\eta}{h_\xi} \equiv \frac{h_2}{h_1} \equiv \frac{(g_{22})^{1/2}}{(g_{11})^{1/2}} = f(\xi,\eta)$$

and the well-known formula for the two-dimensional covariant Laplace operator in orthogonal coordinates, which is

$$\nabla^2 = \frac{1}{h_\xi h_\eta}\left[\frac{\partial}{\partial\xi}\left(\frac{h_\eta}{h_\xi}\frac{\partial}{\partial\xi}\right) + \frac{\partial}{\partial\eta}\left(\frac{h_\xi}{h_\eta}\frac{\partial}{\partial\eta}\right)\right] .$$

The generating equations are thus[2]

$$\frac{\partial}{\partial\xi}\left(f\frac{\partial x}{\partial\xi}\right) + \frac{\partial}{\partial\eta}\left(\frac{1}{f}\frac{\partial x}{\partial\eta}\right) = 0$$

$$\frac{\partial}{\partial\xi}\left(f\frac{\partial y}{\partial\xi}\right) + \frac{\partial}{\partial\eta}\left(\frac{1}{f}\frac{\partial y}{\partial\eta}\right) = 0 \qquad (3)$$

The solution of these equations with appropriate boundary conditions (to be discussed later) will provide the transformation from Cartesian coordinates x,y to an orthogonal curvilinear coordinate system ξ,η provided the mapping actually exists for the particular boundary shape[3]. The scale factors, h_ξ and h_η, that are required in the governing equations of the physical problem, can be computed easily from the standard formulae of tensor analysis

$$h_\alpha^2 \equiv g_{\alpha\alpha} = \delta_{\beta\gamma}\frac{\partial x^\beta}{\partial \xi^\alpha}\frac{\partial x^\gamma}{\partial \xi^\alpha} = \left[\frac{\partial x}{\partial \xi^\alpha}\right]^2 + \left[\frac{\partial y}{\partial \xi^\alpha}\right]^2 \tag{4}$$

Of course, only one of the scale factors needs to be computed from (4) as the second one can be obtained from $h_\eta/h_\xi = f(\xi,\eta)$.

Three types of application should be distinguished:

1. The shape of the domain is not known in advance, but is to be determined as a part of the solution of a physical problem (e.g., free boundary problems in fluid mechanics).

2. The shape of the domain is known, but the distribution of the coordinate nodes along the boundary is not specified and may be determined by the mapping.

3. The shape of the domain is known and the distribution of coordinate nodes is specified along all boundaries, i.e. the complete boundary correspondence is prescribed.

The two methods, considered in the rest of the paper [the "strong constraint" method (section 4) and "weak constraint" method (section 5)] are not equally suitable for these problems. The strong constraint method (which includes conformal mapping as a special case) works well for problems of the first type, and might, in principle, be also applied to problems of type 2. The strong constraint method cannot be used to solve problems of the third type. The weak constraint method, on the other hand, is particularly well suited to problems of the third type, and thus also can be used conveniently for the second category by simply prescribing some reasonable boundary correspondence.

Since problems of types 2 and 3 are more common than those of type 1, the weak constraint method is likely to be the more important of the two methods of mapping.

3. Application to an Infinite Domain

In order to actually apply Eqs. (3) to the calculation of a boundary-fitted coordinate system, it is necessary to specify the distortion function f and determine boundary conditions for the functions $x(\xi,\eta)$ and $y(\xi,\eta)$. As a preliminary, however, we consider here the aplication to an infinite domain. Since the present investigation was originally motivated by the fluid mechanics problem of flow past a deformable bubble (or drop), we shall use this problem for illustration purposes in this and subsequent sections. In the case of a bubble, the interior flow can be ignored and it is therefore only necessary to develop boundary-fitted coordinates for the region exterior to the bubble. The objective, for a given bubble shape, is an orthogonal mapping $X(\xi,\eta)$,$Y(\xi,\eta)$ which maps the unit square $0 \leq \xi \leq 1$ and $0 \leq \eta \leq 1$ onto the exterior of the bubble. A "reasonable" correspondence of the boundaries for this case is sketched in Fig. 1a, with $\xi = 1$ being the bubble surface, $\xi = 0$ corresponding to "infinity" and η varying from 0 to 1 as the bubble surface is traversed from the trailing to leading axis of symmetry. Note that the ξ,η coordinate system, as sketched, will yield (after rotation about the x-axis) a left-handed three-dimensional coordinate system ξ,η,φ if the sense of rotation is such that the cylindrical coordinates x,y,φ (where $y \geq 0$) are right-handed, but this presents no real problems and will actually be very useful in the case of a viscous drop where the matching of an exterior and interior coordinate system is most convenient when one is right-handed and the other left-handed. One should only remember that in a left-handed coordinate system all the expressions which involve the Levi-Civita alternating symbol ε_{ijk} (e.g. cross product and curl) change sign.

The first problem, and one whose resolution is of some general interest, is the mapping of an infinite domain by numerical solution of equations (3) subject to some suitable boundary conditions. Since numerical solution cannot produce functions $X(\xi,\eta)$ and $Y(\xi,\eta)$ which reach infinite values, it is necessary to introduce some modification into the problem. One obvious possibility would be to simply truncate the X,Y domain at a large, but finite distance. However, a more satisfactory resolution is to combine a

numerically generated orthogonal mapping from ξ,η to a ("fictitious") auxiliary domain in which $x(\xi,\eta)$ and $y(\xi,\eta)$ are finite, followed by a conformal mapping from this finite auxiliary domain to the infinite, "physical" domain in the X,Y space.

From the properties of conformal mapping it follows immediately that the ξ,η coordinates in the physical X,Y space will be orthogonal; moreover, the scale factors H_ξ,H_η for these coordinates will be related to the scale factors h_ξ,h_η of the auxiliary mapping via simple formulae

$$H_\xi = |F'|h_\xi \ , \ H_\eta = |F'|h_\eta$$

where F is the analytic function which defines the conformal mapping, i.e. $X + iY = F(x + iy)$.

One especially simple and convenient conformal mapping (of the so-called second kind since it reverses orientation) which transforms from a finite to infinite domain is the inversion

$$F(w) = \frac{1}{\bar{w}} \ ; \quad X + iY = \frac{1}{x-iy} \tag{5}$$

which leads to

$$X = \frac{x}{r^2} \ , \ Y = \frac{y}{r^2} \ , \ H_\xi = \frac{h_\xi}{r^2} \ , \ H_\eta = \frac{h_\eta}{r^2} \ . \tag{6}$$

where

$$r^2 = x^2 + y^2 \ .$$

A qualitative sketch of the auxiliary mapping $x(\xi,\eta),y(\xi,\eta)$, which, when combined with (5) and (6), will yield an orthogonal, boundary-fitted coordinate system outside a bubble (or any particle), is seen in Fig. 1b. The point x=y=0 corresponds to infinity in the X,Y plane and is an image of the line $\xi = 0$, i.e. the mapping is singular here. The distortion function $f(\xi,\eta)$ should thus be equal to 0 at $\xi = 0$ (a concentration point of the coordinate system). Other factors concerning the choice of $f(\xi,\eta)$ will be discussed

later.

4. Mapping by the Strong Constraint Method

a. Choice of the Distortion Function and Boundary Conditions

Let us now turn to the application of orthogonal mapping, beginning with the simplest case from a conceptual point of view, in which the distortion function $f(\xi,\eta)$ is specified completely throughout the ξ,η domain. In anticipation of the alternative approach outlined in section 5, the method of mapping associated with this condition will be called the "strong constraint method". It is especially convenient when the shape of the domain must be determined as a part of the solution of the problem (e.g. the shape of a bubble in flow at finite Reynolds number), but cannot be used when the boundary correspondence is completely specified, where the "weak constraint" method of section 5 must be adopted.

The most appropriate form for the distortion function depends on the domain of interest and any special features of the physical problem which must be resolved. Consider, for example, a bubble in a uniform fluid flow. The auxiliary domain has already been sketched in Fig. 1b, and we have noted that $f(0,\eta)$ should be 0. If one does not need the distortion to vary along the boundary $\xi = 1$, one can simply choose $f(\xi,\eta)$ to be the same as for polar coordinates, i.e. $f = \pi\xi$. Such a choice would, of course, produce polar coordinates if the shape of the boundary $\xi = 1$ were a semicircle with its center at x=y=0, though very different coordinates will be produced when the shape of the boundary is noncircular. One potential advantage of equating $f(\xi,\eta)$ with the distortion function for some classical, "separable" coordinate system (such as polar coordinates), is that it may be possible to construct analytical expressions for the mapping functions, $x(\xi,\eta)$ and $y(\xi,\eta)$ — see section 4c below. On the other hand, if one wants the computational grid to be denser in the region downstream of the bubble (say, to resolve the wake), this can be accomplished easily by introducing the desired η

dependence into the distortion function —see Fig. 2. Similarly, a higher resolution can be achieved in the boundary region by introducing a more complicated dependence on ξ into $f(\xi,\eta)$. Note that the finite-difference equations of the problem of interest will always be solved on a uniform grid in the unit square, $0 \leq \xi,\eta \leq 1$; it is well known that the uniform grid is preferable for the production of finite-difference schemes of high accuracy.

Let us now consider the boundary conditions for numerical generation of the mapping $x(\xi,\eta),y(\xi,\eta)$. Referring to Fig. 1b, it is easy to see that

$$\left.\frac{\partial x}{\partial \eta}\right|_{\substack{\eta=0\\ \eta=1}} = 0 \quad ; \quad \left. y \right|_{\substack{\eta=0\\ \eta=1}} = 0 \quad . \tag{7}$$

At $\xi = 0$, which is a concentration point for the coordinate system and a singular point for the differential Eqs. (3), the only necessary condition is that x and y be finite (see Morse and Feshbach [19], pp. 713-716), which reflects the fact that no real physical boundary is present. This condition will, of course, be satisfied by any numerical solution of (3), and it is permissible to choose arbitrary values [within some reasonable range of 0(1)] for x and y at $\xi = 0$, with the particular choice influencing the solutions for $x(\xi,\eta)$ and $y(\xi,\eta)$ by no more than the order of accuracy of the numerical scheme. Here, we simply choose

$$\left. x \right|_{\xi=0} = 0 \quad ; \quad \left. y \right|_{\xi=0} = 0 \quad . \tag{8}$$

Finally we turn to conditions at the boundary $\xi = 1$, which corresponds to the bubble surface in the example considered here. In general, both $x(1,\eta)$ and $y(1,\eta)$ cannot be specified simultaneously if the resulting coordinate system is to be orthogonal. In order to demonstrate this fact, we need only examine the orthogonality constraint $g_{12} = 0$. With the definition of scale facors (4), and the distortion function, this yields

$$f\frac{\partial x}{\partial \xi} = \frac{\partial y}{\partial \eta} \; ; \qquad \frac{\partial x}{\partial \eta} = -f\frac{\partial y}{\partial \xi} \tag{9}$$

These are obviously the analogue of the Cauchy-Riemann conditions in conformal mapping.[4] Clearly, if $x|_{\xi=1}$ is given as a function of η, the conditions (9) determine $\partial y/\partial\xi\,|_{\xi=1}$, and vice versa. Thus if both $x(1,\eta)$ and $y(1,\eta)$ are given, the conditions (9) provide also $\left.\frac{\partial x}{\partial \xi}\right|_{\xi=1}$ and $\left.\frac{\partial y}{\partial \xi}\right|_{\xi=1}$, and the problem is overdetermined. Note, however, that a combination of a constant Dirichlet condition for one function and a zero Neumann condition for the other will satisfy (9) automatically [conditions (7) are of this type]. If it is essential that both $x(1,\eta)$ and $y(1,\eta)$ be specified (i.e. the exact boundary correspondence of the mapping be prescribed), it is evident that the method of coordinate transformation must be substantially changed. This question is considered in section 5.

We have noted earlier that the strong constraint method is particularly useful for problems in which the boundary shape must be determined as part of the solution. For the example of a deformed bubble, considered here, the shape of the boundary, $x(1,\eta),y(1,\eta)$ must be attained as part of the problem solution. One approach is to use an iterative procedure starting from an initial shape (e.g. spherical). At each iteration, the position of the curve $\xi = 1$ which represents the bubble boundary (in either x,y or X,Y) must be changed incrementally in the normal direction, with the magnitude and sign of the increment (i.e. whether the boundary moves locally "in" or "out") to be determined by the magnitude and sign of the local normal-stress imbalance across the interface.

What is needed for application of the strong constraint method to problems involving an unknown boundary shape is a method for changing the mapping $x(\xi,\eta),y(\xi,\eta)$ so that the position of the curve $\xi = 1$ is changed in the desired direction by a small increment normal to itself. This must be done without directly specifying both $x(1,\eta)$ and $y(1,\eta)$, as would seem to be necessary if one were to attempt somehow to specify the new position of a boundary point [say, $x^n(1,\eta),y^n(1,\eta)$] directly from its position in the

previous iteration $[x^{n-1}(1,\eta),y^{n-1}(1,\eta)]$. The approach proposed here is to alter the mapping, in a prescribed fashion, by changing its metric tensor (i.e. the scale factors). In particular, it is evident from the geometrical significance of $h_\xi(\xi,\eta)$ that a point of the boundary, say $\xi = 1$, $\eta = \eta_o$, can be moved outward or inward along a ξ-coordinate line ($\eta = \eta_o$) which is locally normal to the boundary (due to the orthogonality of the coordinate lines) by simply increasing or decreasing $h_\xi(\xi,\eta_o)$. There is, of course, no way to modify h_ξ all along the line $\eta = \eta_o$ in an *a priori* fashion and still obtain a mapping which satisfies Eqs. (3). If a point on the boundary is moved, the mapping functions and the scale factors are then completely determined inside the domain by these equations. The approach which we adopt is thus to derive boundary conditions for the functions x and y at $\xi = 1$ which are equivalent to changing h_ξ locally in the limit as $\xi \to 1$. In order that this change in $h_\xi(1,\eta_o)$ actually cause the boundary $\xi = 1$ to move inward or outward in the x,y plane, it is necessary that it propagate inside the domain to produce changes of the same sign for $h_\xi(\xi,\eta_o)$ for $\xi < 1$. We can offer no rigorous proof at this time that this will always be true. For now, we simply accept it as a hypothesis. It should be noted, however, that this hypothesis is supported in the special case $f = 1$ of conformal mapping by the so-called Lindelöf principle [20] and has also turned out to be true for all test cases that we have considered to date.

The iterative procedure which we have adopted in the case of determining the unknown boundary shape for a bubble may be represented as follows. The value of $h_\xi(1,\eta_o)$ at the n^{th} iteration is calculated as its value at the previous iteration plus a small change $\delta^{n-1}(\eta_o)$, dependent on (in the simplest case, "proportional to") the normal stress imbalance at η_o for the $n\text{-}1^{st}$ iteration, i.e.

$$h_\xi^n(1,\eta_o) = h_\xi^{n-1}(1,\eta_o) + \delta^{n-1}(\eta_o) \tag{10}$$

for $0 \le \eta_o \le 1$. The new value of $h_\xi(1,\eta_o)$ is then transformed into boundary values for $\left.\frac{\partial x}{\partial \xi}\right|_{\xi=1}$ and $\left.\frac{\partial y}{\partial \xi}\right|_{\xi=1}$ by means of the definition

$$\left(h_\xi^n\right)^2 = \left(\frac{\partial x^n}{\partial \xi}\right)^2 + \left(\frac{\partial y^n}{\partial \xi}\right)^2 \tag{11}$$

and the constraint of orthogonality, $g_{12} = 0$. The latter is implemented by noting that $g_{12} = 0$ can be expressed in the form

$$\left.\frac{\left(\frac{\partial y}{\partial \xi}\right)}{\left(\frac{\partial x}{\partial \xi}\right)}\right|_{\xi=1} = -\left.\frac{\left(\frac{\partial x}{\partial \eta}\right)}{\left(\frac{\partial y}{\partial \eta}\right)}\right|_{\xi=1} \tag{12}$$

The term on the left-hand side is the slope of a ξ-coordinate line at the boundary, while that on the right is the negative inverse of the slope of the boundary ($\xi = 1$) itself. Thus, in order that the iterative procedure converge to a mapping in which the ξ-coordinate line at the boundary ($\xi = 1$) is orthogonal to the boundary, we interpret (and use) Eq. (12) as defining the slope of the ξ-coordinate line at the n^{th} iteration via the slope of the boundary $\xi = 1$ at the previous iteration, i.e.

$$\left.\frac{\left(\frac{\partial y^n}{\partial \xi}\right)}{\left(\frac{\partial x^n}{\partial \xi}\right)}\right|_{\xi=1} = -\left.\frac{\left(\frac{\partial x^{n-1}}{\partial \eta}\right)}{\left(\frac{\partial y^{n-1}}{\partial \eta}\right)}\right|_{\xi=1} \tag{13}$$

Equations (10), (11) and (13) provide sufficient information to determine boundary conditions for

$$\left.\frac{\partial x^n}{\partial \xi}\right|_{\xi=1} \quad \text{and} \quad \left.\frac{\partial y^n}{\partial \xi}\right|_{\xi=1}$$

at each new iteration. Equation (13) can be applied either in the given form or inverted, the choice being made in such a manner as to avoid division by very small numbers. The signs of $\left.\frac{\partial x^n}{\partial \xi}\right|_{\xi=1}$ and $\left.\frac{\partial y^n}{\partial \xi}\right|_{\xi=1}$ [which are found by a square root operation from (11)] are determined from the signs of $\left.\frac{\partial y^{n-1}}{\partial \eta}\right|_{\xi=1}$ and $\left.\frac{\partial x^{n-1}}{\partial \eta}\right|_{\xi=1}$

via (9).

The procedure outlined above can be implemented easily on a computer and leads to a stable and fast iterative process. It may be noted, however, that the boundary conditions for $x(\xi,\eta)$ are all of the Neumann type, with the exception of the "weak" condition at $\xi = 0$ and the solution is therefore determined only up to an arbitrary constant. Numerically, this "indeterminacy" manifests itself in the fact that the coordinate boundary (and, in fact, the whole coordinate system) may "creep" along the x axis during the iterative process (the point $\xi = 0$ stays at $x = 0$ but, being a singular point, it cannot "hold" the rest of the solution — see the discussion above). A simple way to eliminate this unwanted movement is to add a constant to $x(\xi,\eta)$ after each iteration, with the value chosen in such a way that the points closest to $\xi = 0$ on the x axis [i.e. $x(h,0)$ and $x(h,1)$ where h is the gird size] are required to fit symmetrically about the point $x = 0$.

b. Numerical Examples of the Strong Constraint Method

The proposed strong constraint method for generation of boundary-fitted, orthogonal coordinates has now been reduced to the solution of Eqs. (3), subject to the boundary conditions described above. A variety of finite-difference schemes can be used for this purpose. In our own computations we have adopted the ADI technique of Peaceman and Rachford (see, e.g. Richtmyer and Morton [21]) and used a 41x41 grid, i.e. $h = 0.025$.

First, we test the adequacy of Eqs. (11) and (13) for the generation of boundary conditions for $(\partial x/\partial\xi)_{\xi=1}$ and $(\partial y/\partial\xi)_{\xi=1}$ with $h_\xi(1,\eta)$ known. We consider two cases. In the first, we set

$$h_\xi(1,\eta) = 1$$

and

$$f(\xi,\eta) = \pi\xi(1 - 0.9\cos\pi\eta) \quad .$$

while the second has

$$h_\xi(1,\eta) = \begin{cases} \sin^2\pi\eta & \text{for} \quad 0 \le \eta \le 0.5 \\ 1 & \text{for} \quad 0.5 \le \eta \le 1 \end{cases}$$

and

$$f(\xi,\eta) = \pi\xi \quad .$$

In both cases, an iterative process is necessary even with $h_\xi(1,\eta)$ specified. For the calculations reported here, we start with an initial guess for x,y, use this to calculate $(\partial x/\partial\eta)$ and $(\partial y/\partial\eta)$ at the boundary ($\xi = 1$), use the specified form for h_ξ and Eqs. (11) and (13) to obtain boundary values for $\partial x/\partial\xi\big|_{\xi=1}$ and $\partial y/\partial\xi\big|_{\xi=1}$, and finally calculate a new estimate for the mapping by numerically solving Eqs. (3) with $\partial x/\partial\xi\big|_{\xi=1}$ and $\partial y/\partial\xi\big|_{\xi=1}$ as boundary conditions. With this new estimate for $x(\xi,\eta)$ and $y(\xi,\eta)$ the process can be repeated. Presumably, if Eqs. (11) and (13) did not provide a sufficient means of obtaining boundary conditions for $x(\xi,\eta)$ and $y(\xi,\eta)$ (and this is by no means obvious), we might expect this iterative procedure to diverge. However, in both of the cases listed above, a convergent solution was obtained. In the first example, a very good initial guess can be generated analytically and the test of conditions (11) and (13) is rather weak. However, the resulting coordinate mapping, which is shown in Fig. 2, is of some qualitative interest in itself since it demonstrates how the density of a computational grid can be controlled by $f(\xi,\eta)$; this particular grid might potentially be useful for computation of the flow past a body with a developed wake. The "teardrop" shape shown in Fig. 3 was obtained for the second case and constitutes a much stronger test of convergence with boundary conditions generated from Eqs. (11) and (13). In this case, approximately 60 iterations [with a constant time step 0(h)] were necessary to compute the mapping, starting with polar coordinates (and a circular boundary) as an initial guess (sixty iterations correspond to approximately 30 sec of CPU time on the

VAX-11/780 computer which we used for our work). It should be noted that $h_\xi(1,\eta) = 1$ for all η in this initial guess and the change from this to the specified form for $h_\xi(1,\eta)$ is a very strong "jump", much greater than one might expect at each step in an overall solution scheme for a problem with unknown boundary shape where h_ξ is incremented according to Eq. (10). The maximum nonorthogonality error in the final solution is approximately 0.5%, i.e. $\max|g_{12}| \simeq 0.005$.

Let us now turn to an example of a problem in which an unknown boundary shape is to be calculated as part of the solution. This will constitute a final numerical test of the strong constraint method. Figure 4 gives a final converged solution for the axisymmetric steady shape of a bubble at finite Reynolds number, for a uniform streaming flow which moves from left to right. Of course, the shape is initially unknown and can be determined only in the course of solving the full fluid dynamical problem, described by the Navier-Stokes equations and appropriate boundary conditions. This is precisely the type of problem that the strong constraint method was designed to handle, but it is very important to establish the convergence of the overall solution scheme outlined in section 4a, including iterative incremental changes in $h_\xi(1,\eta)$ as indicated in Eq. (11). In the present example, only an approximate solution of the fluid dynamics problem was obtained on the grid provided by the mapping at each overall iteration. This decreases the necessary computing time to the final steady state, but renders meaningless the transient results for bubble shape and velocity field at intermediate iterations in the solution scheme. The mapping and bubble shape illustrated in Fig. 4 were obtained starting from a sphere as the initial guess for bubble shape. After obtaining the solution of the fluid dynamics problem for a given boundary shape at each iteration in the overall solution scheme, the scale factor $h_\xi(1,\eta)$ was changed according to the sign and magnitude of the normal stress imbalance at the surface of the bubble, as discussed in subsection 4a. The new scale factor was then used to redefine the mapping and the corresponding boundary shape for the bubble, and the whole process was

repeated for this new shape, until overall convergence was achieved. A detailed account of this fluid mechanical problem will appear in a forthcoming publication. A brief description of the solution procedure and results was presented in [13].

c. On the Possibility of Analytical Solution by Separation of Variables

The present approach to the construction of an orthogonal mapping via the strong constraint method is primarily a numerical one. Nevertheless, it is of interest to note that the possibility exists for analytical solution in cases where the distortion function $f(\xi,\eta)$ of the mapping happens to coincide with the distortion function of some classical separable coordinate system. For example, the distortion function in the previous section, $f(\xi,\eta) = \pi\xi$, is just that for polar coordinates and an analytical solution could have been attempted. The reason for this is that the covariant Laplace Eq. (3), which defines the orthogonal mapping, has exactly the same form for the general orthogonal coordinates ξ,η as it does in the classical polar coordinate system with the same $f(\xi,\eta)$ — simply because the form of the equation depends only on $f(\xi,\eta)$. The domain in the ξ,η plane is a unit square and one can solve Eqs. (3), in principle, as a series expansion in the appropriate eigenfunctions of the Laplace equation.

As an example, let us consider the distortion function $f(\xi,\eta) = \pi\xi$ for which the general solution of the Laplace equation, that is finite at $\xi = 0$, is (Morse and Feshbach [19], pp. 713-714),

$$\sum_{l=0}^{\infty} [A_l \cos(l\pi\eta) + B_l \sin(l\pi\eta)]\xi^l \quad .$$

Applying the conditions at $\xi = 0$, $\eta = 0$ and $\eta = 1$ that were discussed in section 4a, one thus obtains

$$x = \sum_{l=1}^{\infty} A_l \cos(l\pi\eta)\xi^l; \qquad y = \sum_{m=1}^{\infty} B_m \sin(m\pi\eta)\xi^m$$

and the conditions for orthogonality (9) require

$$A_l = B_m \quad \text{for} \quad l = m \quad .$$

The mapping is thus

$$x = \sum_{l=1}^{\infty} A_l \cos(l\pi\eta)\xi^l \quad ; \quad y = \sum_{l=1}^{\infty} A_l \sin(l\pi\eta)\xi^l$$

and the coefficients are to be determined from the boundary conditions at $\xi = 1$, where

$$\sum_{l=1}^{\infty} A_l \cos(l\pi\eta) = x|_{\xi=1} \quad ; \quad \sum_{l=1}^{\infty} A_l \sin(l\pi\eta) = y|_{\xi=1} \quad . \tag{14}$$

One can distinguish several possible cases insofar as determination of A_l is concerned. First, in the unlikely circumstance that *one* of the Cartesian coordinates, i.e. x or y, is known at the boundary $\xi = 1$ as a function of the transform variable η, the coefficients can be obtained directly from (14) using the orthogonality of $\cos(l\pi\eta)$ and/or $\sin(l\pi\eta)$. Second, in a more realistic situation, the shape of the boundary $\xi = 1$ is given parametrically, e.g.

$$x|_{\xi=1} = u(s) \quad ; \quad y|_{\xi=1} = v(s) \quad ; \qquad 0 \leq s \leq s_{max}$$

where s is an arclenth, i.e.

$$\left(\frac{du}{ds}\right)^2 + \left(\frac{dv}{ds}\right)^2 = 1 \quad .$$

Since the correspondence between s and η is not ordinarily known, the coefficients A_l in this case cannot be found directly in closed form, but some version of a method of successive approximations should be used.

Finally, there may be cases like that discussed in section 4a in which the boundary shape is not known in advance but must be determined as part of the solution. In this case, an iterative procedure like that adopted in section 4a is appropriate.

Whatever method (numerical or analytical) is used to construct the mapping, the equations of the problem of interest, which are to be solved on the mapped domain, may still be solvable by separation of variables, provided $f(\xi,\eta)$ is of some classical

form. This curious possibility of using classical analytical methods of solution, devised for some very special coordinate systems, in the case of a much more general orthogonal mapping is due to the fact that the form of the governing equations depends mainly (for the Laplace equation entirely) on the distortion function.

These analytical approaches are worth exploring in more detail than is done here. On the other hand, as the next section will show, in many cases it may be advantageous to use a distortion function which is not limited by the requirement of being of some classical form.

5. Orthogonal Mapping with a Prescribed Boundary Correspondence (the Weak Constraint Method)

The strong constraint method, considered so far, could also be used, at least in principle, for problems of type 2 when the shape of the domain (but not the complete boundary correspondence) is prescribed from the beginning. In this case, one might start from some initial approximation to the desired boundary shape and proceed iteratively by using the distance between the desired boundary and the numerical approximation to that boundary (measured along the direction normal to the current boundary) as a driving 'normal force" for moving the boundary in or out. In practice, however, a much more powerful technique can be devised for dealing both with this problem, and the apparently more difficult one in which the complete boundary correspondence (i.e. the boundary shape and the spacing of coordinate nodes along the boundary) is specified. This is the topic of the present section.

Let us then consider the generation of an orthogonal mapping with a prescribed boundary correspondence. It has often been suggested that such a mapping is impossible — see, for example, Thompson *et al.* [1], p. 300. Indeed, in the case of conformal mapping it is not possible to achieve a prescribed boundary correspondence, and this is crucial in limiting the application of conformal mapping to problems of practical

importance.

It would be very beneficial in a number of applications to be able to construct an orthogonal mapping with a prescribed distribution of grid points along a boundary of given shape. Indeed, in the case of a boundary separating two domains of solution (e.g. the surface of a liquid drop), this ability is imperative in order that the normal coordinate lines on the two sides emanate from the same boundary points (otherwise application of matching conditions is greatly complicated).

It may seem, at first, that the present approach could not be any more successful than conformal mapping as far as the determination of a mapping with prescribed boundary correspondence is concerned. Indeed, a complete prescription of boundary shape and mesh spacing along a boundary requires the imposition of Dirichlet boundary conditions for both functions $x(\xi,\eta)$ and $y(\xi,\eta)$ on the boundaries of the ξ,η domain — and this is clearly impossible with $f(\xi,\eta)$ specified (as discussed in section 4a). However, we will see that the present approach does allow orthogonal mappings with prescribed boundary correspondence, provided one imposes what we shall call a "weak constraint" on $f(\xi,\eta)$, rather than specifying $f(\xi,\eta)$ completely throughout the whole ξ,η domain.

We have noted in section 2 that two degrees of freedom exist in defining a mapping in two dimensions. In the method of the preceding section, these were used to impose the orthogonality condition $g_{12} = 0$, and to specify the distortion function, $f(\xi,\eta) \equiv h_\eta/h_\xi$, throughout the domain of ξ and η. It will be convenient to refer to constraints specified throughout ξ and η as utilizing a "domain degree of freedom", and call these "strong constraints". Evidently, in this terminology, a mapping in two dimensions allows imposition of two (and only two) strong constraints, and the imposition of an added "boundary constraint", in the form of a prescribed boundary correspondence, will cause the mapping to be over-determined *unless one of the domain constraints*, for

g_{12} *or* f, *is relaxed.* The basic idea proposed here is to maintain orthogonality, i.e. $g_{12} = 0$, while giving up a part of the freedom to specify $f(\xi,\eta)$ everywhere in return for the ability to specify both $x(\xi,\eta)$ and $y(\xi,\eta)$ on the boundary of the ξ,η domain. In other words, we propose to relinquish a "part" of the "domain degree of freedom" available to specify f, in order to gain a "boundary degree of freedom" for $x(\xi,\eta)$ [or $y(\xi,\eta)$] while still retaining the orthogonality condition $g_{12} = 0$. Instead of prescribing the function $f(\xi,\eta)$ explicitly throughout the domain, we give a rule which determines f in the interior of the ξ,η domain as soon as it is known on the boundary. The *boundary* values of f are found using the definition of $f(\equiv h_\eta/h_\xi)$, and the formulae (4) to obtain h_ξ and h_η from the mapping functions $x(\xi,\eta)$ and $y(\xi,\eta)$. The latter are obtained, in principle, by solving Eqs. (3) subject (for prescribed boundary correspondence) to Dirchlet conditions on the boundaries of the ξ,η domain. It is evident, since the governing Eqs. (3) for x and y involve f, that the *boundary* values for f (which are used to determine f in the interior) and the mapping functions $x(\xi,\eta)$ and $y(\xi,\eta)$ must be determined sequentially in a successive approximation scheme, starting from some initial guess for f. The exact manner in which this scheme is implemented will be discussed shortly. As a preliminary, however, it is useful to consider some additional factors that are intended to clarify the fundamental ideas behind the approach proposed here to obtain orthogonal mappings with a prescribed boundary correspondence.

First, the rule to determine f from its boundary values is essentially arbitrary, subject to the condition that $f > 0$. It may thus take the form of an algebraic ("interpolation") formula, or, for example, an elliptic differential equation which can be solved to determine f from its values on the boundary. For convenience, we denote this type of condition on f as a weak constraint to distinguish it from the strong constraint in which f is given explicitly throughout the domain. It is obvious that a weak constraint together with the values of f on the boundary is exactly equivalent to some strong constraint, and we have seen that a strong constraint on f is enough, together with the

condition $g_{12} = 0$, to determine an orthogonal mapping in two dimensions. The available domain degree of freedom may thus be used either to impose a strong constraint on f (as in the previous section), or to impose a weak constraint together with values of f along the boundary. Heuristically, the second approach divides a domain degree of freedom into two "parts": the "interior degree of freedom" (used by a weak constraint) and the "boundary degree of freedom".

The key idea of the present development is to use a weak distortion constraint instead of a strong one, and to leave the values of f along the boundary unspecified, i.e. to let these values be determined by the mapping itself. The hope is that in this case one will be able to prescribe the boundary correspondence, since the boundary degree of freedom, available for the distortion constraint, is not used.

Let us now discuss how the method is to be applied. As we have noted, the problem of determining $x(\xi,\eta)$ and $y(\xi,\eta)$ is rather unusual in the sense that the coefficients of the governing partial differential Eqs. (3) depend via $f(\xi,\eta)$ on the coupling between the solutions $x(\xi,\eta)$ and $y(\xi,\eta)$. The problem is thus nonlinear and must be solved by some iterative procedure. Although this might seem a disadvantage in comparison with the strong constraint method of the previous section, this is not necessarily true since the latter also requires iteration (on boundary conditions) and it is not obvious which iteration will converge most rapidly. At any rate, this nonlinearity is a small price to pay for the ability to construct an orthogonal mapping with a prescribed boundary correspondence.

The iterative procedure mentioned above may be realized as follows:

1. Choose an initial guess for $x(\xi,\eta)$,$y(\xi,\eta)$, thus obtaining an initial guess for $f(\xi,\eta)$ via its definition and expressions for scale factors (4). It is preferable, but probably not absolutely necessary, that the initial $f(\xi,\eta)$ satisfy the chosen weak constraint, i.e. the chosen rule for determining f from its boundary values.

2. Using this $f(\xi,\eta)$ and the Dirichlet boundary conditions for $x(\xi,\eta),y(\xi,\eta)$ known from the prescribed boundary correspondence, calculate new $x(\xi,\eta),y(\xi,\eta)$ from the basic Eqs. (3); if some iterative scheme is used to solve (3), it will be sufficient to advance the solution by only a few (or even one) iterations.

3. Calculate new scale factors on the boundary from $x(\xi,\eta),y(\xi,\eta)$ using (4).

4. Use the weak constraint and the new boundary values for $f(\xi,\eta)$, calculated from the scale factors of step 3, to find new $f(\xi,\eta)$ in the interior of the domain.

5. Go to step 2 and repeat.

This algorithm appears to work fairly well. It has been tried with two types of weak distortion constraints (rules) — algebraic "interpolation" and an elliptic partial differential equation (EPDE). The weak constraint may apparently be chosen quite arbitrarily, but it should give $f(\xi,\eta)$ which is non-negative and, preferably, smooth. Since the freedom to prescribe the boundary correspondence already gives a considerable degree of control over the spacing of coordinate lines near the boundaries (which is usually the most important area), the weak constraint can often be chosen as a rule which determines the values of $f(\xi,\eta)$ in the interior of a domain as some kind of simple interpolation between its boundary values.

To obtain interpolation by EPDE, $f(\xi,\eta)$ is defined as a solution of some EPDE with Dirichlet boundary conditions. The EPDE may, for example, be the ordinary Laplace equation $\frac{\partial^2 f}{\partial \xi^2} + \frac{\partial^2 f}{\partial \eta^2} = 0$, and the motivation for this approach is the fact that a linear interpolation in 1D can be thought of as defined by the differential equation $\frac{d^2 f}{d\xi^2} = 0$. It is, of course, known that the solution of the ordinary Laplace equation provides a means of (local) averaging throughout the domain.

Although this EPDE approach appears quite sophisticated, experience obtained in the course of the present study indicates that the simpler, algebraic, approach is often

to be preferred, and this will now be described in more detail.

To obtain a convenient formula for an algebraic interpolation, consider first the case when the given boundary values of $f(\xi,\eta)$ are zero in all four corners of the $0 \leq \xi,\eta \leq 1$ domain. Then the formula

$$f^o(\xi,\eta) = (1-\xi)f(0,\eta) + \xi f(1,\eta) + (1-\eta)f(\xi,0) + \eta f(\xi,1)$$

gives a suitable, smooth interpolation. If the corner values are not zero, however, this formula is not suitable, since each corner value appears in it twice, giving a spurious contribution. To obtain a useful interpolation formula in this case, we need to subtract a bilinear "corner function"

$$f^c(\xi,\eta) = (1-\xi)(1-\eta)f(0,0) + (1-\xi)\eta f(0,1) + \xi(1-\eta)f(1,0) + \xi\eta f(1,1) \quad .$$

The final formula for an algebraic interpolation thus reads[5]

$$f^a(\xi,\eta) = f^o(\xi,\eta) - f^c(\xi,\eta) \tag{15}$$

This algebraic interpolation is very easy to apply both as a weak constraint for a distortion function $f(\xi,\eta)$ and as an initial guess for $x(\xi,\eta)$ and $y(\xi,\eta)$ (if a better guess is not available). We note in passing that if orthogonality of the boundary-fitted coordinates is not required [as in the method of Thompson *et al.* (see section 1)], a direct algebraic interpolation for $x(\xi,\eta),y(\xi,\eta)$ provides the simplest possible way to construct a complete coordinate system with prescribed boundary correspondence.

It should be borne in mind that one has almost complete freedom in choosing the weak constraint rule, and the above suggestions are simply examples. In particular, some control over the spacing of the coordinate lines can obviously be achieved by the form chosen for the weak constraint, in addition to the strong control obtained by prescribing the boundary correspondence. The only limitation is that $f(\xi,\eta)$ must be greater than 0 inside the domain. In some cases, this will follow automatically from the fact that $f(\xi,\eta) > 0$ at the boundaries (where it is calculated as a ratio of two posi-

tive quantities - the scale factors). In other cases, the condition $f(\xi,\eta) > 0$ inside the domain may be quite simply satisfied by adding some function of ξ and η to (15), which vanishes at the boundaries; the same function can also be efficiently used for control of the coordinate mesh. Other possibilities are conceived easily, but the details of choosing the weak constraint rule are much better discussed in the context of a particular application and we will not deal with them further here.

Let us finally consider numerical examples of the weak constraint method. These examples were obtained using an ADI technique to solve Eqs. (3) and the algebraic interpolation (15) as an initial guess for $x(\xi,\eta)$, $y(\xi,\eta)$. The number of iterations needed was of the same order (50 - 100) as required by the strong constraint method of section 4. The "peanut" shape, shown in Fig. 5 was obtained by simply specifying arbitrarily chosen values of x and y (i.e. prescribing the boundary correspondence) at $\xi = 1$, $\eta = 0$ and $\eta = 1$; plus the boundary conditions $y(0,\eta) = 0$ and $\left.\frac{\partial x}{\partial \xi}\right|_{\xi=0} = 0$ at the boundary $\xi = 0$ (which in this case corresponds to a segment of the x axis). This last pair satisfies the orthogonality conditions (9) for any $f(0,\eta)$ which means that at this part of the boundary (only) the value of $f(\xi,\eta)$ needs to be given; it was chosen as $f(0,\eta) = 4\sin^2\pi\eta$. The algebraic interpolation (15) served then as a weak constraint on the distortion function $f(\xi,\eta)$. Note that in order to make the picture legible, only every second of the η-coordinate lines were drawn.

The mapping shown in Fig. 6 gives a coordinate system in the interior of the axisymmetric bubble, deformed by the flow. The distribution of the coordinate nodes at the surface of the bubble (i.e. the boundary correspondence $x(1,\eta)$,$y(1,\eta)$ at the boundary $\xi = 1$) was taken from the mapping of the exterior of the bubble (see Fig. 4) which was obtained previously as a part of the solution of the fluid mechanical problem using the strong constraint method. The boundary conditions for $x(\xi,\eta)$ and $y(\xi,\eta)$ at $\xi=0$, $\eta=0$ and $\eta=1$ were assumed to be the same as in section 4a [see (7) and (8)] and hence,

they too satisfy (9) for any distortion $f(\xi,\eta)$. Thus, $f(\xi,\eta)$ must be specified independently at $\xi=0$, $\eta=0$ and $\eta=1$. If $\xi=0$ is to be a concentration point of the coordinate system, then $f(0,\eta)$ should be equal to 0, and if $f(\xi,0)$ and $f(\xi,1)$ are taken to be linear functions of ξ, one obtains the simplest possible variety of the algebraic weak constraint

$$f(\xi,\eta) = \xi f(1,\eta) \quad ,$$

which was, in fact, used to construct the mapping in Fig. 6.

In the last two examples, shown in Figs. 7 and 8, we consider mapping in a concave region whose shape is similar to a domain in which the recent method of Haussling and Coleman [8] failed to produce an orthogonal grid even for shapes with smaller boundary curvature. It is important to note that the boundary correspondence in Figs. 7 and 8 was prescribed on all four boundaries. The mapping in Fig. 7 was computed with the weak constraint given by (15). The mapping in Fig. 8 was obtained using (15) multiplied by $(1 - 0.8 \sin \pi\xi \sin \pi\eta)$ as the weak constraint. Comparing Figs. 7 and 8, it can be seen that the form chosen for the weak constraint does provide a degree of control over the spacing of the coordinate grid inside the domain; however, the main features of the mapping are determined by the prescribed boundary correspondence. Though the numerical examples that we have considered show that an orthogonal mapping can be computed with a prescribed boundary correspondence for reasonably complicated geometries, they do not, of course, prove either the existence or uniqueness of such mappings for arbitrary geometries and/or boundary correspondence. This is a very important and interesting question, but one that is far beyond the scope of the present study and probably requires the attention of theoretical mathematicians.

A final important point about the weak constraint method concerns the prescription of the boundary correspondence. Apart from the difficult question of the existence of a mapping, some care must also be exercised to minimize the possibility of the result-

ing coordinates being ill-suited for numerical solutions. Consider, for example, the problem of generating orthogonal coordinates inside an acute angle with coordinate nodes distributed in equal increment along the sides. Evidently, orthogonal coordinates can be generated quite easily if these nodes are connected by one family of coordinate lines with the other family emanating from the vertex (thus giving, essentially, polar coordinates inside the angle). However, if it were assumed that the side boundary nodes belonged to different families of coordinate lines (as might initially seem to be the obvious choice if one were to think of the acute angle as being obtained from a right angle with Cartesian coordinates inside it, by simply decreasing the included angle), the configuration of the corresponding coordinates is less obvious and the numerically generated coordinates would likely have a larger nonorthogonality error due to discretization.

6. Conclusions

The mapping techniques proposed in this paper provide a method for the construction of an orthogonal, boundary-fitted coordinate system in two dimensions. The strong constraint method of orthogonal mapping is obtained by specifying $f(\xi,\eta)$ throughout the ξ,η domain in advance and is especially suitable for cases when the shape of the boundary in the x,y plane is not known but is to be found as a part of the solution of some physical problem ('free boundary problems'). The weak constraint method of orthogonal mapping is obtained by specifying a rule which determines the values of $f(\xi,\eta)$ in the interior of the ξ,η domain as soon as its boundary values are known. This method is capable of solving the most important and difficult problem, namely the construction of an orthogonal mapping with a prescribed boundary correspondence, or, in other words, the construction of an an orthogonal coordinate system fitted to a boundary of given shape, with a prescribed distribution of coordinate nodes along this boundary.

The governing equations of any physical problem of interest can be written out easily in the resulting orthogonal coordinate system in terms of physical components of vectors and tensors, using the standard expressions for invariant differential operations in orthogonal coordinates. Alternatively, the technique of tensor analysis can be employed directly for this purpose if the connection coefficients in the orthonormal basis and a "physical tensor" notation (given in the Appendices) are used.

The most serious rival of the present method is, of course, conformal mapping. The main advantage of conformal mapping is that a harmonic function of the x,y coordinates remains a harmonic function of the ξ,η coordinates. This reduces the solution of the Laplace equation on some domain in the x,y plane to a problem of finding the conformal mapping for this domain. However, this reduction is not of much help unless a conformal mapping function has already been tabulated; moreover, the solution of the Laplace equation, though significant, is certainly not the only important problem to be solved.

The important drawbacks of conformal mapping include the difficulty of construction by the direct approach, closely connected with the inability to prescribe the boundary correspondence, and the potentially poor quality of the resulting grid for numerical solutions. The method proposed here for orthogonal mapping is free of these problems. In addition, it has the potential of extension to a three-dimensional space.

Footnotes

1. Note that this case can also serve as a basis for three-dimensional orthogonal coordinates in the presence of either translational symmetry in the direction normal to the x,y plane (i.e. no dependence on z) or axial symmetry. For these special cases, the three-dimensional orthogonal coordinates are obtained, respectively, by either translating the ξ,η system in the z direction or rotating it about the axis of symmetry provided that the latter is also a coordinate line in ξ,η.

2. One of the referees has pointed out that Eqs. (3) can be obtained from Thompson et al.'s Eqs. (1) with an appropriate choice for P and Q, thus suggesting that the present mapping techniques (and all related techniques intended to generate orthogonal mappings) should be considered as special cases of Thompson et al.'s technique. While the first part of this statement is, of course, true, the specific choice

$$P = \frac{1}{h_\xi h_\eta}\frac{\partial f}{\partial \xi};\ Q = \frac{1}{h_\xi h_\eta}\frac{\partial}{\partial \eta}\left[\frac{1}{f}\right]$$

which is necessary to obtain (3), was not, apparently, evident to Thompson and coworkers, who suggested that P and Q be chosen as sums of decaying exponentials and stated "An orthogonal system cannot be achieved with arbitrary spacing of the coordinate lines around the boundary"; nor to subsequent workers (cf. Haussling and Coleman [8]) who actually attempted to generate the P and Q so as to ensure an orthogonal mesh. At any rate, this choice is not directly realizable since h_ξ and h_η cannot be specified in advance.

3. It may be noted that the present orthogonal mapping corresponds to a special case of a so-called quasiconformal mapping [17,18] when f and f^{-1} are bounded [the "complex dilatation" μ of the quasiconformal mapping being real and equal to $(1 - f)/(1 + f)$ in this case]. An extensive mathematical theory of quasiconformal map-

ping has been developed, including the mapping theorem [17,18] which establishes the existence of a quasiconformal mapping for a given μ (and thus of an orthogonal mapping for a given f if f and f^{-1} are bounded). It would obviously be of considerable interest to establish theoretically the existence of an orthogonal mapping for any given f, since some of the most useful orthogonal mappings do not satisfy the above boundedness conditions (e.g. the mapping which gives polar coordinates, has $f = \pi\xi$, so that $f = 0$ at $\xi = 0$, see section 4a). In this paper we take the existence of an orthogonal mapping for granted and proceed to the practical task of generating the mapping numerically.

4. Note that the signs in (9) are for a mapping which preserves orientation, otherwise the signs are reversed.

5. We are indebted to one of the referees for pointing out the existence of an elaborate mathematical framework [22] for constructing expressions of this type. In mathematical terminology, the Eq. (15) is a "bivariate interpolation by a Boolean sum of projection operators" $P_\xi \oplus P_\eta \equiv P_\xi + P_\eta - P_\xi P_\eta$, where the projection operator P_ξ has been defined in our case as $P_\xi f(\xi,\eta) \equiv (1-\xi)f(0,\eta) + \xi f(1,\eta)$, i.e. P_ξ and P_η realize linear interpolations in 1D. Obviously, much more sophisticated interpolation formulae can be obtained by using more complicated forms for P_ξ and P_η.

Appendix A.

Connection Coefficients in Orthonormal Basis

In order to use the orthogonal mapping techniques which are presented in the main body of this paper, it is necessary to express the governing differential equations and boundary conditions of a physical problem, which are normally given in terms of the invariant differential operators for vectors and/or tensors, in terms of a general orthogonal coordinate system. In most instances this can be done by simply using the standard expressions for the various invariant differential operations in orthogonal curvilinear coordinates which are given in numerous texts and require only a knowledge of the scale factors h_i. However, expressions for some differential operations are not readily accessible, and it is necessary, in general, to have a method available for their derivation from the invariant (tensorial) form. The most commonly advocated approach is to use the expression for the ∇ operator, together with the expressions for the spatial derivatives of the unit basis vectors. This is a rather cumbersome and outdated procedure in comparison with the powerful technique of tensor analysis; the trouble is, however, that the connection coefficients, which are necessary for covariant differentiation, are usually given only for a coordinate basis (whose vectors $\mathbf{e}_i \equiv \frac{\partial \mathbf{r}}{\partial \xi^i}$ are not generally of unit length). In this case (only) they are called "Christoffel symbols". Correspondingly, covariant differentiation can usually be performed only for covariant and contravariant components of vectors and tensors.

In the case of an orthogonal coordinate system, it is highly preferable to use an orthonormal basis (whose basis vectors $\mathbf{e}_{\hat{i}} \equiv \frac{\mathbf{e}_i}{h_i}$ are of unit length) and physical components of the vectors and/or tensors. In this case, we need only the normal rules for covariant differentiation and the connection coefficients for an orthonormal basis. These connection coefficients are derived easily, following the methods of [14] (see, in

particular, Chapter 8), but we do not intend to spell out the details here. Instead, we simply state the results, first using the standard notation of tensor analysis. In Appendix B, a much simplified notation is introduced for "physical tensors", which is a natural and obvious extension of the Cartesian tensor formalism.

We use the gradient of a second rank tensor, say

$$G \equiv \nabla T$$

as a suitable invariant object (a third rank tensor) for illustration purposes. This entity can be expressed for any particular coordinate system in terms of its components calculated in any basis according to the rules of covariant (absolute) differentiation (denoted by the semicolon ";")

$$G^i{}_{jk} \equiv T^i{}_{j;k} = T^i{}_{j,k} + \Gamma^i{}_{lk}T^l{}_j - \Gamma^l{}_{jk}T^i{}_l$$

where indices run through 1,2,3 and summation over repeated indices is implied. The connection coefficients are denoted $\Gamma^m{}_{np}$, and the comma "," indicates differentiation of the tensor component as if it were a scalar (for example, $f_{,k}$ indicates the k^{th} component of the gradient of a scalar field f). It should be noted that this "scalar differentiation" coincides with partial differentiation $\partial/\partial\xi^k$ only in a coordinate basis; in the orthonormal basis it is given by

$$f_{,\hat{i}} \equiv \mathbf{e}_{\hat{i}} \cdot \nabla\, f = \frac{1}{h_i}\frac{\partial f}{\partial \xi^i} \,. \tag{A1}$$

Scale factors h_i, being a shorthand notation for $(g_{ii})^{1/2}$, are exempt from the summation convention. Carets are employed to indicate the use of an orthonormal basis.

Now, in a general three-dimensional space, there are 27 connection coefficients. However, in an orthonormal basis, only 12 are nonzero, and these can be expressed in the compact form

$$\Gamma^{\hat{m}}_{\hat{n}\hat{m}} = -\Gamma^{\hat{n}}_{\hat{m}\hat{m}} = h_{m,\hat{n}}/h_m \quad (m \neq n, \text{ no summation}) \,. \tag{A2}$$

The general rule for covariant differentiation, together with the formulae (A1) and (A2) are all that is needed to write any differential expression in terms of physical components in a general orthogonal coordinate system.

Appendix B

A Simplified "Physical Tensor" Notation for Covariant Differentiation in Orthogonal Coordinates

An orthonormal basis (with a positive definite metric) is identical with its dual (reciprocal), so that covariant and contravariant components coincide (and are called "physical") and the usual distinction between these quantities, by the use of upper and lower indices, becomes unnecessary. In other words, the metric tensor of an orthonormal basis is always a unit tensor, i.e. $g_{\hat{i}\hat{j}} = \delta_{ij}$. (This tensor should be distinguished, however, from the metric tensor of the coordinate basis g_{ij}, which is used in the main body of this paper and is often called "the metric tensor of the coordinate system" because it defines the line element.) Although an attempt has previously been made to formulate the rules of tensor calculus specifically for physical components (see Ericksen [23]), the resulting rules have not found application, apparently due to notational inconvenience. Here, a much simplified notation is introduced which is a natural generalization of Cartesian tensor formalism. Since the physical components are by definition (see McConnell [24]) the components in the local Cartesian coordinate system, whose basis vectors coincide with the orthonormal basis vectors at a given point, the similarity between physical and Cartesian tensor analysis is not surprising.

The transition to a simplified notation for physical tensors from the general covariant formalism is accomplished by writing all indices of tensor or vector components as subscripts and switching to the convention of summation over repeated subscripts

which is typical of Cartesian tensors. The carets, which indicated an orthonormal basis before, will be dropped since we deal with orthonormal bases only. All tensor algebra for physical tensors is formally identical to Cartesian tensor calculus, but the rules of differentiation are different. Specifically, the gradient of a tensor field $G \equiv \nabla T$ is calculated according to the following rule of covariant (meaning here 'invariant') differentiation for physical tensors

$$G_{ij\cdots nk} \equiv T_{ij\cdots n;k} = T_{ij\cdots n,k} + \Gamma_{il k}T_{lj\cdots n} + \Gamma_{jl k}T_{il\cdots n} + \cdots + \Gamma_{nl k}T_{ij\cdots l} \tag{B1}$$

where the comma "," denotes scalar differentiation defined by

$$f_{,k} = \frac{1}{h_k}\frac{\partial f}{\partial \xi_k} \tag{B2}$$

(as always, scale factors h_i are exempt from the summation convention).

For a Cartesian coordinate system where

$$\text{all } h_i = 1 \ , \quad \text{all } \Gamma = 0$$

the rule (B1) reduces to the familiar partial differentiation of Cartesian tensor calculus. Otherwise one has to correct for the change of scale [thus (B2)] and for the variation of basis vectors in space [the "ΓT" terms in (B1), one for each index of T]. To remember the pattern of these latter terms, the following mnemonic rule is useful: (1) The last index of Γ is always the differentiation index; (2) The index being corrected shifts to the first subscript on Γ and is replaced on T by a dummy summation index, identical to the middle index on Γ. The 12 nonzero connection coefficients can be taken directly from (A2),

$$\Gamma_{iji} = -\Gamma_{jii} = h_{i,j}/h_j \equiv \frac{1}{h_i h_j}\frac{\partial h_i}{\partial \xi_j} \quad (i \neq j, \textit{ no summation}) \tag{B3}$$

The basic rule of tensor analysis is that a tensorially correct equation (formula), which is true in a particular coordinate system (say, Cartesian), is true in any other coordinate system. It is thus evident that a physical law expressed in terms of the physical components for some arbitrary orthogonal system is formally identical to its component form for Cartesian tensors, provided only that ordinary partial derivatives with respect to coordinates are replaced by covariant derivatives, i.e. one simply has to substitute semicolons for the symbol used to indicate partial differentiation in the Cartesian expression and then use (B1). This makes relatively complicated differential expressions very easy to calculate assuming a familiarity with the corresponding Cartesian tensor quantities. By way of illustration, we may consider the derivation of formulae for the physical components of the rate-of-strain tensor in a general orthogonal coordinate system. A diagonal component, such as e_{11}, is simply

$$e_{11} \equiv u_{1;1} = u_{1,1} + \Gamma_{1i1}u_i = \frac{1}{h_1}\frac{\partial u_1}{\partial \xi_1} + \frac{u_2}{h_1 h_2}\frac{\partial h_1}{\partial \xi_2} + \frac{u_3}{h_1 h_3}\frac{\partial h_1}{\partial \xi_3}$$

while the off-diagonal (2,3) component is

$$e_{23} \equiv \frac{1}{2}(u_{2;3} + u_{3;2}) = \frac{1}{2}(u_{2,3} + \Gamma_{2i3}u_i + u_{3,2} + \Gamma_{3i2}u_i)$$

$$= \frac{1}{2}\left[\frac{1}{h_3}\frac{\partial u_2}{\partial \xi_3} - \frac{u_3}{h_2 h_3}\frac{\partial h_3}{\partial \xi_2} + \frac{1}{h_2}\frac{\partial u_3}{\partial \xi_2} - \frac{u_2}{h_2 h_3}\frac{\partial h_2}{\partial \xi_3}\right]$$

Although these formulae are identical to those derived by direct differentiation of the basis vectors (see, e.g. [25], p. 600), they are obviously much easier to obtain using the physical tensor notation.

So far we have been dealing with general orthogonal coordinates in 3D. However, the orthogonal coordinate system used in practice is most likely to be axisymmetric or two-dimensional, in which cases even fewer connection coefficients remain nonzero. Consider first the axisymmetric case, with $\xi_3 \equiv \varphi$ being the azimuthal angle. In this case, $h_3 = \sigma$ where σ is the distance between the point of interest and the symmetry

axis, and only eight connection coefficients remain nonzero

$$\Gamma_{121} = -\Gamma_{211} = h_{1,2}/h_1 \equiv \frac{1}{h_1 h_2}\frac{\partial h_1}{\partial \xi_2};\quad \Gamma_{212} = -\Gamma_{122} = h_{2,1}/h_2 \equiv \frac{1}{h_2 h_1}\frac{\partial h_2}{\partial \xi_1};$$

$$\Gamma_{313} = -\Gamma_{133} = \sigma_{,1}/\sigma \equiv \frac{1}{\sigma h_1}\frac{\partial \sigma}{\partial \xi_1};\quad \Gamma_{323} = -\Gamma_{233} = \sigma_{,2}/\sigma \equiv \frac{1}{\sigma\ h_2}\frac{\partial\ \sigma}{\partial \xi_2}; \tag{B4}$$

In the two-dimensional case with $\xi_3 = z$ and $h_3 = 1$, only Γ_{121}, Γ_{211}, Γ_{212} and Γ_{122} remain nonzero.

The formalism presented above provides an easy method for writing any differential expression in terms of physical components for the boundary-fitted orthogonal coordinates (ξ,η,φ) whose construction we have discussed in the main body of the paper. A final quantity of interest, relevant to the boundary conditions in some problems, is the boundary curvature. The geometric definition of the connection coefficients for the orthonormal basis (see [14], Chapter 8) is

$\Gamma_{ijk} \equiv$ (i component of the rate of change in $\mathbf{e}_j$, along $\mathbf{e}_k$).

Thus, it is evident that

$$\Gamma_{iij} = \kappa^{(ij)}_{(n)}\ ;\quad \Gamma_{kjj} = \kappa^{(ij)}_{(g)}$$

where $\kappa^{(ij)}_{(n)}$ is the normal curvature in the direction $\mathbf{e}_j$ of the coordinate surface with normal $\mathbf{e}_i$ and $\kappa^{(ij)}_{(g)}$ is the geodesic curvature of the ξ_j coordinate line on the same surface (note, there is a slight difference here from the classical definition of geodesic curvature which usually takes it to be always positive - see [15,24]).

If one considers the ξ_j coordinate line as a curve on the coordinate surface $\xi_k =$ const, the geometrical meaning of Γ_{iij} and Γ_{kjj} is reversed, i.e.

$$\Gamma_{iij} = -\kappa^{(kj)}_{(g)}\ ;\quad \Gamma_{kjj} = \kappa^{(kj)}_{(n)}$$

The half-sum of the normal curvatures in two perpendicular directions [say, $\kappa^{(ij)}_{(n)}$ and

$\kappa_{(n)}^{(ik)}$] gives the mean curvature of the surface; and since the coordinate lines of an orthogonal coordinate system are also the lines of curvature of a coordinate surface ([15], p. 195), these normal curvatures are also the principal curvatures and hence their product gives the Gaussian (intrinsic) curvature of the surface.

This work was supported by a grant from the National Science Foundation. The authors wish to thank J. R. A. Pearson and P. R. Eiseman for valuable comments on an earlier draft of this paper.

References

1. J. F. Thompson, F. C. Thames and C. W. Mastin, Automatic numerical generation of body-fitted curvilinear coordinate system for field containing any number of arbitrary two-dimensional bodies, J. Comp. Phys. **15** (1974), 299-319.

2. F. C. Thames, J. F. Thompson, C. W. Mastin and R. L. Walker, Numerical solutions for viscous and potential flow about arbitrary two-dimensional bodies using body-fitted coordinate systems, J. Comp. Phys. **24** (1977), 245-273.

3. B. Fornberg, A numerical method for conformal mapping, SIAM J. Sci. Stat. Comput. 1 (1980), 386-400.

4. D. I. Meiron, S. A. Orszag and M. Israeli, Applications of numerical conformal mapping, J. Comp. Phys. **40** (1981), 345-360.

5. T.-K. Hung and T. D. Brown, An implicit finite-difference method for solving the Navier-Stokes equation using orthogonal curvilinear coordinates, J. Comp. Phys. **23** (1977), 343-363.

6. S. B. Pope, The calculation of turbulent recirculating flows in general orthogonal coordinates, J. Comp. Phys. **26** (1978), 197-217.

7. C. D. Mobley and R. J. Stewart, On the numerical generation of boundary-fitted orthogonal curvilinear coordinate systems, J. Comp. Phys. **34** (1980), 124-135.

8. H. J. Haussling and R. M. Coleman, A method for generation of orthogonal and nearly orthogonal boundary-fitted coordinate systems, J. Comp. Phys. **43** (1981), 373-381.

9. G. Starius, Constructing orthogonal curvilinear meshes by solving initial value problems, Numer. Math. **28** (1977), 25-48.

10. D. E. Potter and G. H. Tuttle, The construction of discrete orthogonal coordinates, J. Comp. Phys. **13** (1973), 483-501.

11. C. W. Davies, An initial value approach to the production of discrete orthogonal coordinates, J. Comp. Phys. **39** (1981), 164-178.

12. G. Ryskin, Development of a numerical procedure for the problem of fluid motion past a deformable body (bubble or drop), Internal Report, Department of Chemical Engineering, California Institute of Technology, (March 15, 1979) (unpublished).

13. G. Ryskin and L. G. Leal, Bubble shapes in steady axisymmetric flows at intermediate Reynolds numbers, in: Proc. 2nd Int. Colloq. on Drops and Bubbles, Monterey, California, November 1981 (D. H. LeCroissette, ed.), pp. 151-156, NASA JPL Publication 82-7, Pasadena, California, 1982.

14. C. W. Misner, K. S. Thorne and J. A. Wheeler, "Gravitation", Freeman, San Francisco, 1973.

15. I. S. Sokolnikoff, "Tensor Analysis", 2nd edition, Wiley, New York, 1964.

16. L. P. Eisenhart, "Riemannian Geometry", Princeton University Press, Princeton, N.J., 1950 (corrected printing of 1926 edition).

17. L. V. Ahlfors, "Lectures on quasiconformal mappings", Van Nostrand, Princeton, N.J., 1966.

18. O. Lehto and K. I. Virtanen, "Quasiconformal Mappings in the Plane", Springer, New York, 1978.

19. P. M. Morse and H. Feshbach, "Methods of Theoretical Physics", McGraw-Hill, New York, 1953.

20. M. A. Lavrentiev and B. V. Shabat, "Methods of the theory of functions of complex variable " ("Metody teorii funktsii kompleksnogo peremennogo"), Nauka, Moscow, 1973 (in Russian).

21. R. D. Richtmyer and K. W. Morton, "Difference Methods for Initial-Value Problems", Interscience, New York, 1967.

22. W. J. Gordon, Blending-function methods of bivariate and multivariate interpolation and approximation, SIAM J. Numer. Anal. **8** (1971), 158-177.

23. J. L. Ericksen, Tensor fields, in: "Handbuch der Physik" (S. Flugge, ed.), Vol. 3/1, pp. 794-858, Springer, Berlin, 1960.

24. A. J. McConnell, "Applications of Tensor Analysis", Dover, New York, 1957.

25. G. K. Batchelor, "Introduction to Fluid Dynamics", Cambridge University Press, Cambridge, 1967.

Figure Captions

Figure 1. Sketch of the coordinate system for the exterior of an axisymmetric bubble. (a) The final coordinate system in the infinite domain, and (b) the auxiliary mapping for the finite domain.

Figure 2. Control over the density of coordinate lines by distortion function. Here, $f(\xi,\eta) = \pi\xi(1 - 0.9\cos\pi\eta)$; $h_\xi(1,\eta) = 1$.

Figure 3. "Teardrop" shape; obtained with $f(\xi,\eta) = \pi\xi$ and $h_\xi(1,\eta) = \begin{cases} \sin^2\pi\eta & \text{if } \eta \le 0.5 \\ 1 & \text{if } \eta > 0.5 \end{cases}$

Figure 4. Deformed bubble; obtained as a part of solution of the fluid mechanical problem described by the Navier-Stokes equations; $f(\xi,\eta) = \pi\xi$.

Figure 5. "Peanut" shape; obtained by the weak constraint method (only every second of the η-coordinate lines are drawn).

Figure 6. Interior of the deformed bubble; obtained by the weak constraint method with the distribution of the points at the surface taken from the exterior mapping (Fig. 4).

Figure 7. Orthogonal mapping by the weak constraint method with prescribed boundary correspondence on all four boundaries and algebraic interpolation (15) used as the weak constraint.

Figure 8. Same as Fig. 7 but the weak constraint is now (15) multiplied by $(1-0.8\sin\pi\xi\sin\pi\eta)$.

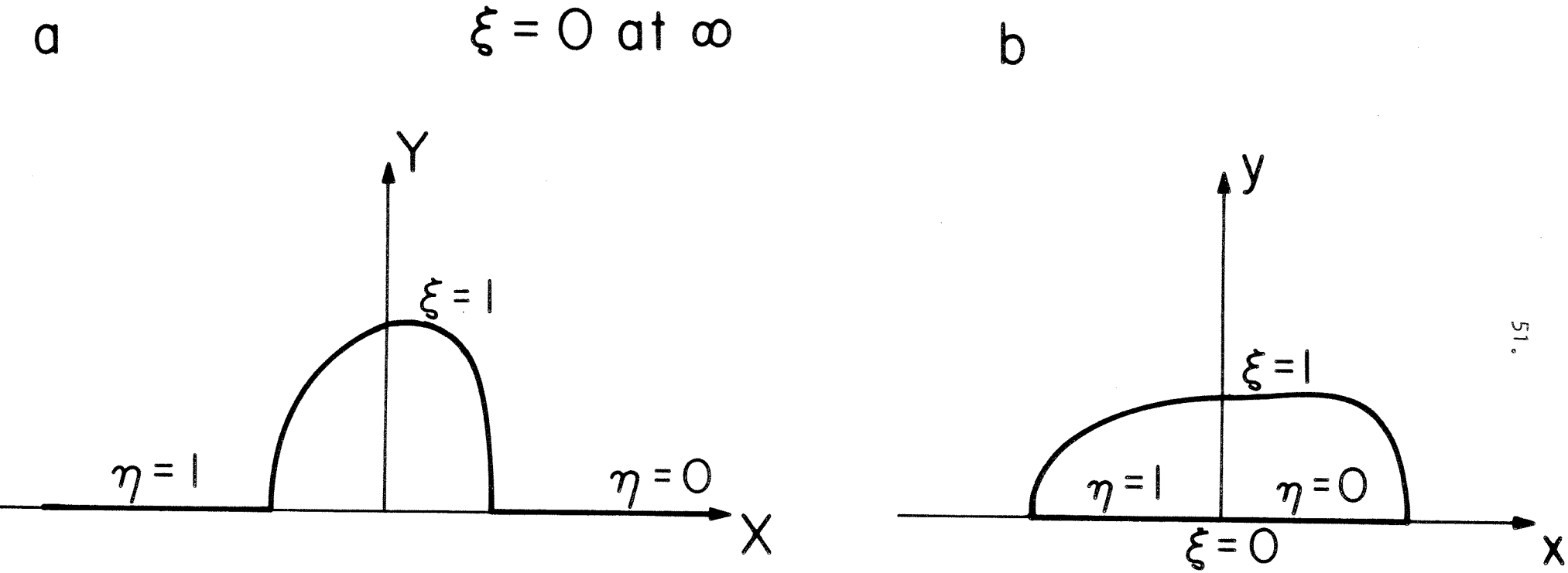

Figure 1

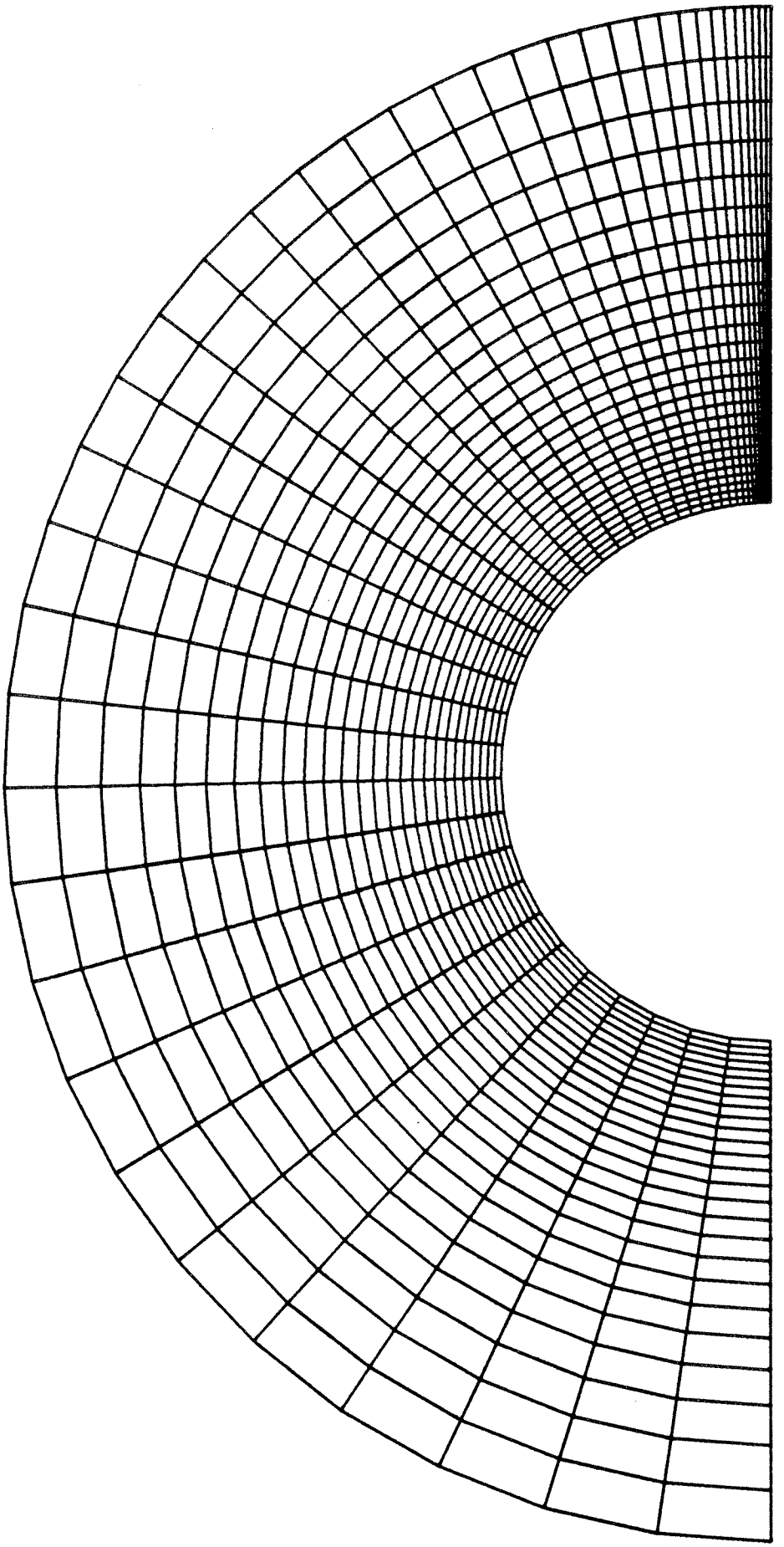

Figure 2

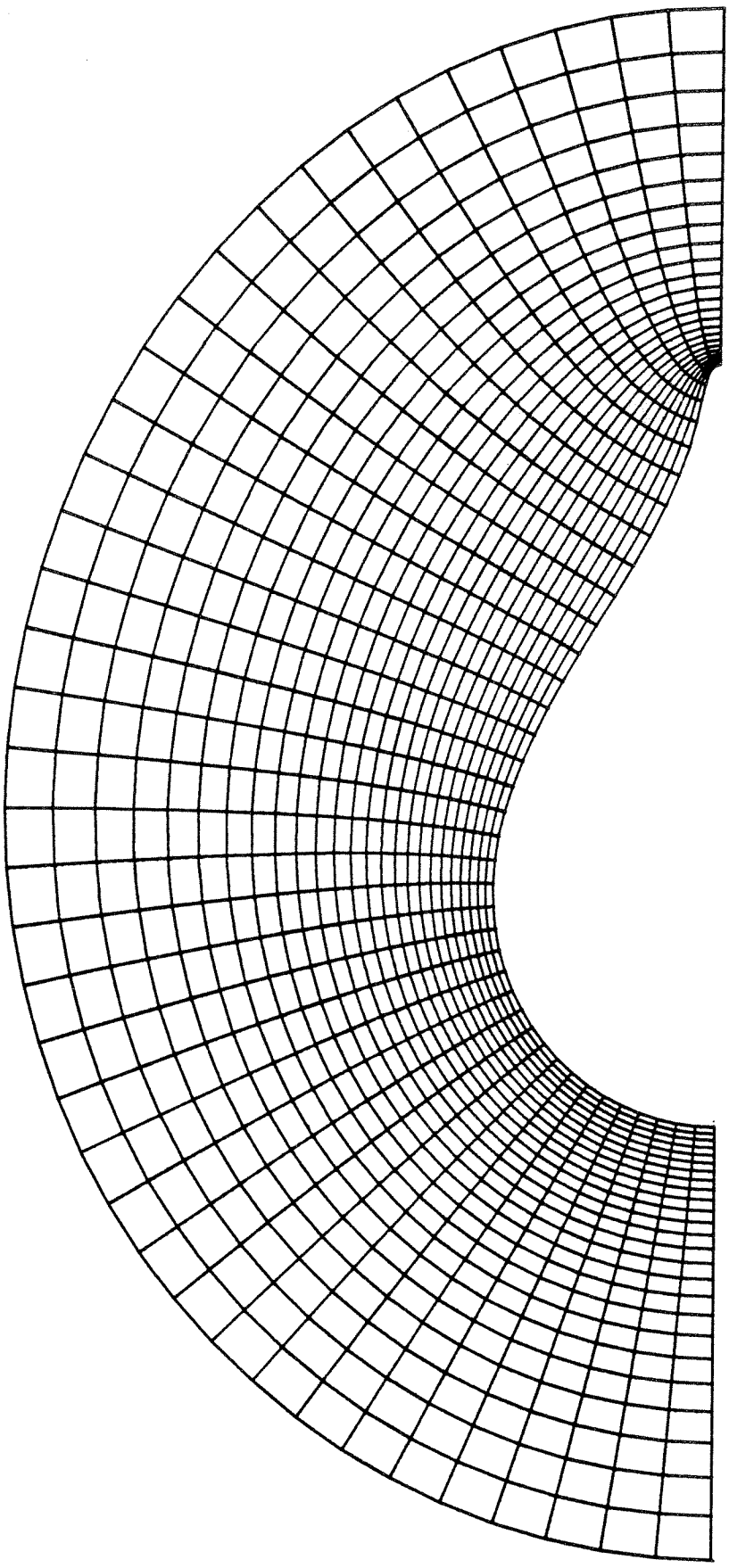

Figure 3

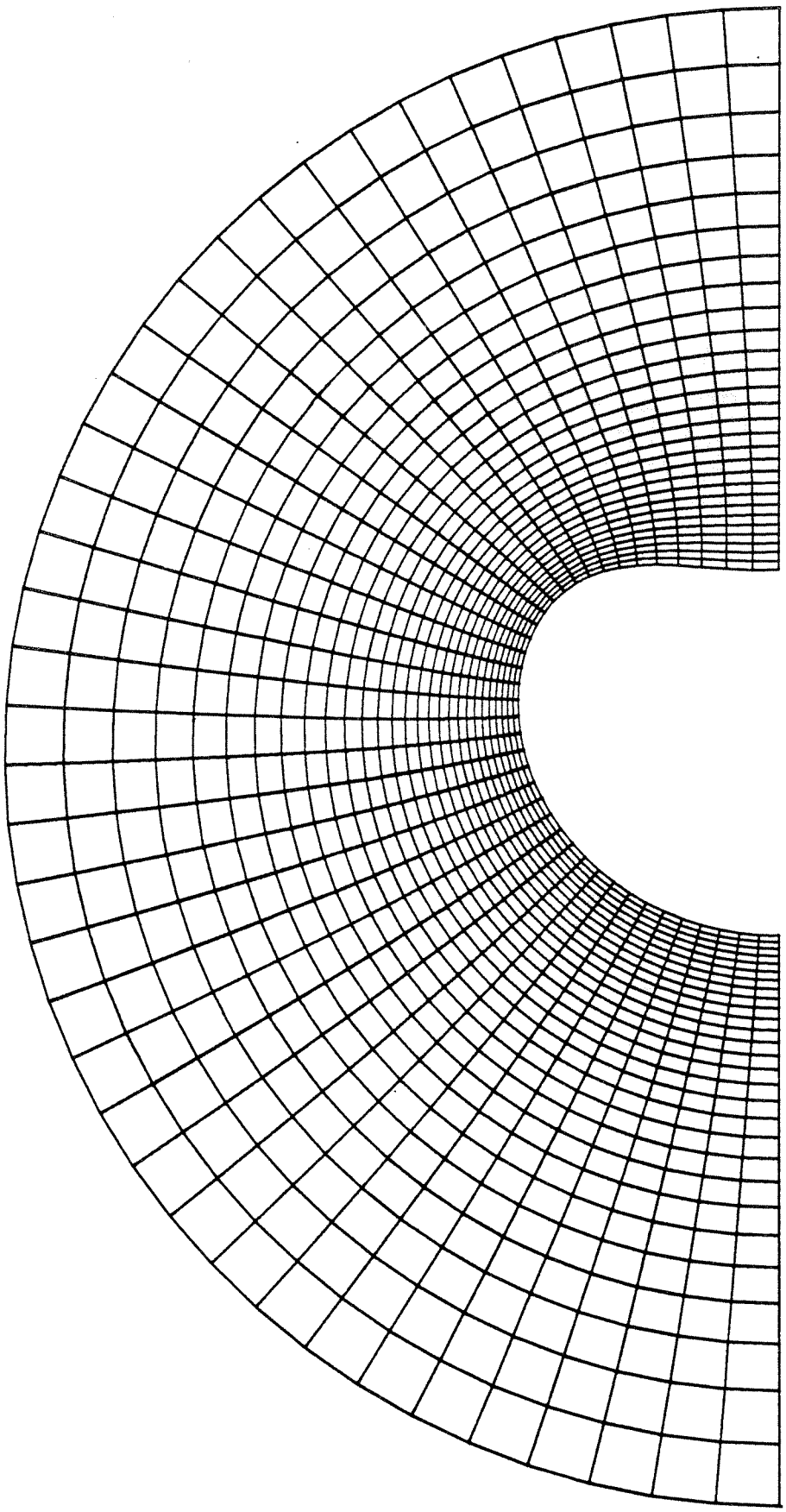

Figure 4

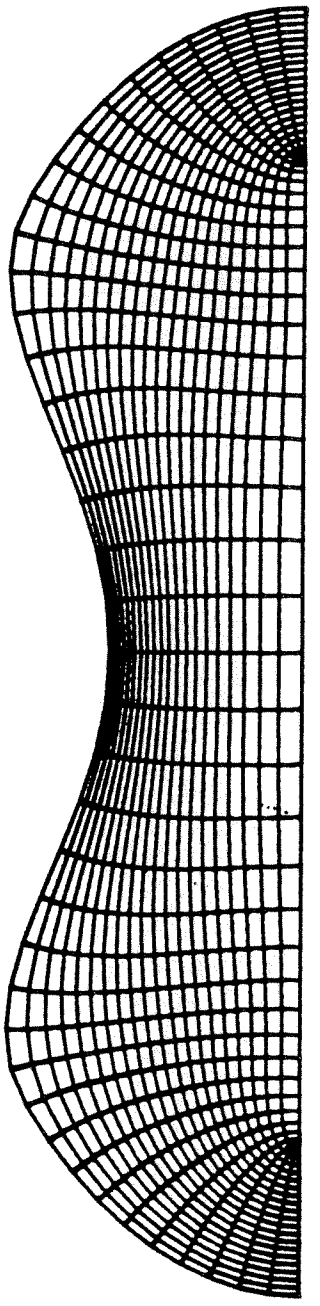

Figure 5

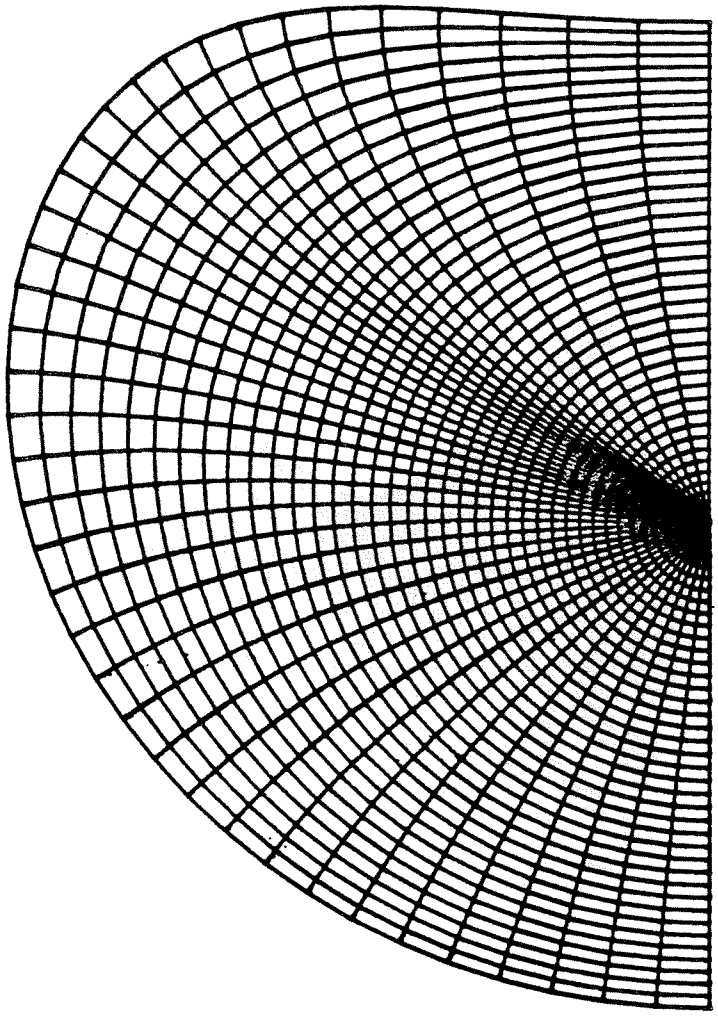

Figure 6

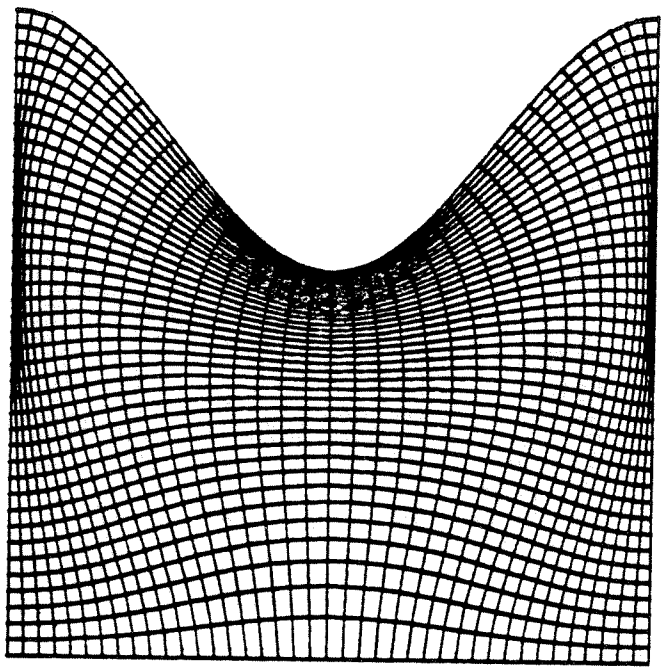

Figure 7

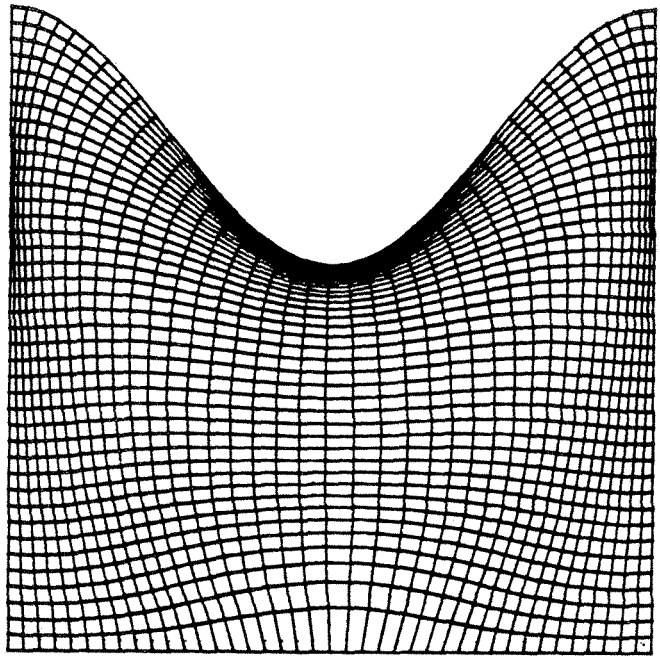

Figure 8

CHAPTER II

Large Deformations of a Bubble in Axisymmetric Steady Flows. Part 1. Numerical Technique

by

G. Ryskin and L. G. Leal

Department of Chemical Engineering
California Institute of Technology
Pasadena, California 91125

Abstract

We present here a brief description of a numerical technique suitable for solving axisymmetric (or two-dimensional) free-boundary problems of fluid mechanics. The technique is based on a finite-difference solution of the equations of motion on an orthogonal curvilinear coordinate system, which is also constructed numerically and always adjusted so as to fit the current boundary shape. The overall solution is achieved via a global iterative process, with the condition of balance between total normal stress and the capillary pressure at the free boundary being used to drive the boundary shape to its ultimate equilibrium position.

J. Fluid Mech. (submitted)

I. Introduction

We are concerned in this paper, and the two papers which follow, with some specific examples of the class of so-called "free-boundary" problems of fluid mechanics. This class of problems is characterized by the existence of one boundary (or more) of the flow domain whose shape is dependent upon the viscous and pressure forces generated by the fluid motion. In this case, the shape of the boundary and the form of the velocity and pressure fields in the fluid are intimately connected, and one must solve for the boundary shape as a part of the overall solution of a particular problem. The most common problems of this type in fluid mechanics occur in the motions of two immiscible fluids which are contiguous at a common interface. In parts II and III of this series, we consider two specific problems involving the motion of a bubble in a viscous, incompressible Newtonian fluid; namely, buoyancy-driven motion through an unbounded, quiescent fluid, and motion in an axisymmetric straining flow. In the present paper, we discuss those general features of the numerical solution scheme, used in parts II and III, which would be expected to carry over to the solution of other free-boundary problems that involve a gas/liquid interface.

The existing published literature on free-boundary problems in fluid mechanics is quite extensive in number, but limited in scope. Three distinct solution methods can be identified. By far the majority of papers is concerned with asymptotic or limiting cases in which the interface shape, while unknown, deviates only slightly from some predefined configuration. In the case of bubble motions, for example, a number of authors have used the so-called "domain perturbation" method to solve for the first (infinitesimal) deviations from a spherical bubble in a variety of flows (cf. Taylor, 1934; Taylor & Acrivos, 1964). In addition, a similar approach has been used to consider the first deviations from the limiting form of a slender body with an arbitrarily small radius-to-length ratio, which is relevant, for example, to uniaxial extensional flows with a sufficiently high strain rate (Taylor, 1964; Acrivos & Lo, 1978). A second method of solution for free boundary problems is restricted to the limiting cases of either zero

Reynolds number, where the governing differential equations are the linear Stokes' equations, or inviscid, irrotational flow where the governing differential equations reduce to Laplace's equation. This is the so-called boundary-integral technique in which fundamental solutions of the governing (linear) equations are used to reduce the general n-dimensional problem to the solution of a set of (n-1)-dimensional integral equations. The boundary-integral method is not restricted to small deformations. Indeed, solutions have been obtained which exhibit large departures from a predefined shape (Youngren & Acrivos, 1976; Miksis, Vanden-Broeck & Keller, 1981; Lee & Leal, 1982). However, this method is applicable only in the creeping or potential flow limits, and this reduces its usefulness. The third and most important class of free boundary problems is that in which neither of the restrictions of small deformation or linear governing differential equations is present. This is, quite simply, the general problem at finite Reynolds number which clearly requires a fully numerical method of solution. This case has received relatively little attention to date. Most of the solutions which have been obtained were developed using a finite-element formulation of the numerical problem. Here we consider an alternative approach based upon a finite-difference approximation of the governing equations.

The finite-difference method which we have developed incorporates a numerically generated orthogonal coordinate system, which is "boundary-fitted" in the sense that all boundary surfaces of the solution domain (including the free-boundary whose shape is determined as part of the solution) coincide with a coordinate line (or surface) of the coordinate system. Thus, the problem of interpolation between nodal points of the finite-difference grid when the latter is not coincident with physical boundaries is avoided altogether. Indeed, the existence of the interpolation problem in the first place is seen to be a consequence of the use of the common, analytically generated coordinate systems, such as cylindrical, spherical, etc. when the latter do not correspond to the natural boundaries of the solution domain.

A full description of the procedure for generation of an orthogonal, boundary-fitted coordinate system has already been given in Ryskin and Leal (1983) hereafter called I. The present paper will focus on implementation of this procedure in a full numerical algorithm for fluid mechanics problems in which the free-boundary is a gas-liquid interface. The mapping procedure is presently restricted to two-dimensional and axisymmetric flow domains. For the problems currently under investigation, we additionally restrict ourselves to steady motions. The shape of the free boundary is determined via an iterative procedure, with the coordinate system changed at each step to match the current approximation to the free boundary shape.

II. Problem Formulation

In this section, we outline the mathematical formulation of a typical free-boundary problem in which the free boundary is a gas-liquid interface that is assumed to be completely characterized by a constant (i.e. spatially uniform) surface tension. In effect, we are assuming that the interface is free of surfactant and the system is isothermal. We assume that the boundary geometry and flow fields are both axisymmetric and steady. The steady-state assumption can be relaxed, in principle, by suitable modification of the methods and equations of this paper. The assumption of axisymmetry is required by the mapping algorithm in its present form. We assume that the liquid in our system is incompressible and Newtonian, and that its density and viscosity is sufficiently large compared with that of the gas so that the dynamic pressure and stress fields in the gas at the interface can be neglected compared to those on the liquid side.

We denote the "boundary-fitted" coordinate system as (ξ,η,φ), with φ being the azimuthal angle measured about the axis of symmetry. In view of the assumed axisymmetry, these boundary-fitted coordinates can be connected with the common cylindrical coordinates (x,σ,φ) (with the axis of symmetry being the x-axis) via a pair of mapping functions, $x(\xi,\eta)$ and $\sigma(\xi,\eta)$, which satisfy the covariant Laplace equations (see I)

$$\frac{\partial}{\partial\xi}\left[f\frac{\partial x}{\partial\xi}\right]+\frac{\partial}{\partial\eta}\left[\frac{1}{f}\frac{\partial x}{\partial\eta}\right]=0$$

$$\frac{\partial}{\partial\xi}\left[f\frac{\partial\sigma}{\partial\xi}\right]+\frac{\partial}{\partial\eta}\left[\frac{1}{f}\frac{\partial\sigma}{\partial\eta}\right]=0 \qquad (1)$$

Here, the function $f(\xi,\eta)$ is the so-called "distortion function" representing the ratio, h_η/h_ξ, of scale factors ($h_\eta \equiv \sqrt{g_{\eta\eta}}$, $h_\xi \equiv \sqrt{g_{\xi\xi}}$) for the boundary-fitted coordinate system. In the "strong constraint" method developed in I for free-boundary problems, the distortion function can be freely specified to provide control over the density of coordinate lines in the boundary-fitted system. With respect to the (ξ,η,φ) system, the mapping is always defined in such a way that the solution domain (for any arbitrary fixed φ) is the unit square

$$0 \le \xi,\eta \le 1 \ .$$

Boundary conditions for the mapping functions $x(\xi,\eta)$ and $\sigma(\xi,\eta)$ were described in detail in I. In section IV we focus on boundary conditions at the free surface, and the corresponding numerical method of adjusting the interface shape at each step in an iterative solution scheme, with the shape change based upon the imbalance of normal stress and surface tension forces calculated from a previous guess of the interface shape.

The fluid mechanics part of the problem, then, is to obtain solutions of the Navier-Stokes equations using a finite-difference approximation in the boundary-fitted (ξ,η) coordinates. With axisymmetry assumed, the Navier-Stokes equations are most conveniently expressed in terms of the stream function ψ and vorticity ω in the form

$$L^2(\omega\sigma) = R\frac{1}{h_\eta h_\xi}\left[\frac{\partial\psi}{\partial\xi}\frac{\partial}{\partial\eta}\left[\frac{\omega}{\sigma}\right]-\frac{\partial\psi}{\partial\eta}\frac{\partial}{\partial\xi}\left[\frac{\omega}{\sigma}\right]\right] \qquad (2)$$

$$L^2\psi + \omega = 0 \qquad (3)$$

where

$$L^2 \equiv \frac{1}{h_\xi h_\eta}\left\{ \frac{\partial}{\partial \xi}\left[\frac{f}{\sigma}\frac{\partial}{\partial \xi}\right] + \frac{\partial}{\partial \eta}\left[\frac{1}{f\sigma}\frac{\partial}{\partial \eta}\right]\right\} \tag{4}$$

and R is the Reynolds number. In terms of the mapping functions, $x(\xi,\eta)$ and $\sigma(\xi,\eta)$, the scale factors which appear in these equations are

$$h_\xi = \left\{\left[\frac{\partial x}{\partial \xi}\right]^2 + \left[\frac{\partial \sigma}{\partial \xi}\right]^2\right\}^{1/2}$$

$$h_\eta = \left\{\left[\frac{\partial x}{\partial \eta}\right]^2 + \left[\frac{\partial \sigma}{\partial \eta}\right]^2\right\}^{1/2} \tag{5}$$

We assume, for convenience, that the coordinate mapping is defined with $\xi = 1$ corresponding to the interface, and $\eta = 0$ and 1 to the symmetry axes. Then, boundary conditions at the symmetry axes are

$$\psi = 0, \omega = 0 \quad \text{at} \quad \eta = 0 \text{ and } 1 \ . \tag{6}$$

At the gas-liquid interface ($\xi = 1$), we require:

$$\psi = 0 \tag{7}$$

corresponding to zero normal velocity in the assumed steady state solution,

$$\omega - 2\kappa_{(\eta)} u_\eta = 0 \tag{8}$$

corresponding to the condition of zero tangential stress (*note*: $\kappa_{(\eta)}$ is the normal curvature of the interface and u_η is the tangential velocity in the η direction); and

$$\tau_{\xi\xi} - \frac{1}{W}\left(\kappa_{(\eta)} + \kappa_{(\varphi)}\right) = 0 \tag{9}$$

representing the balance between the normal stress contributions due to pressure and viscous forces on the one hand and the capillary force on the other (here, $\kappa_{(\varphi)}$ is the normal curvature in the φ direction and W the dimensionless Weber number measuring the ratio of characteristic pressures due to inertial and capillary forces at the interface). The conditions at $\xi = 0$ (the far-field boundary in many cases) depend on the particular problem. If the flow domain is two-dimensional rather than axisymmetric, suitable modifications of the equations (2)-(9) are made easily, but will not be pursued

here.

It may be noted that the complete streamfunction and vorticity fields can be determined for an axisymmetric interface *of specified shape* using only conditions (7) and (8). The normal stress balance (9) then provides a consistency condition on the interface shape, as well as a basis for determining an improved estimate of that shape when the condition is not satisfied. As is well known, the only source of vorticity at the gas-liquid (zero tangential stress) interface is the boundary curvature.

III. Solution Algorithm

The problem, from a numerical point of view, is to solve simultaneously the differential equations (1), (2) and (3) for the mapping functions and the streamfunction/vorticity fields subject to conditions (6)-(9) at the interface, $\xi = 1$, plus appropriate additional boundary conditions at the other boundaries, $\xi = 0$ and $\eta = 0,1$ as indicated above.

A simple approach which we have found to be efficient and stable for solution of this coupled fluid dynamics-mapping problem involves an iterative procedure that can be summarized broadly as follows:

1. Choose some initial shape of the gas-liquid interface together with the corresponding orthogonal coordinate system (usually taken from a known solution or obtained analytically, as for a spherical bubble).

2. Obtain an approximation to the streamfunction and vorticity fields by carrying out some small number of iterations on Eqs. (2) and (3), subject to the boundary conditions (6)-(8), plus the appropriate conditions at $\xi = 0$. In practice, we have found that the most rapid convergence of the overall solution algorithm is usually attained by a single iteration at this step.

3. Check the normal stress condition, Eq. (9), and if it is not satisfied, modify the interface shape so as to reduce the imbalance between the total stress, $\tau_{\xi\xi}$, and the

surface tension term $(\kappa_{(\eta)} + \kappa_{(\varphi)})/W$, and compute a new (approximate) boundary-fitted coordinate system by carrying out some number of iterations (usually one) on Eqs. (1), plus boundary conditions.

4. Return to step 2 and repeat until all equations and boundary conditions are satisfied.

In the subsequent sections of this paper, we shall consider in detail several aspects of the numerical algorithm which we believe may not be obvious. In particular, we discuss implementation of the tangential stress condition (8), the ADI technique used to solve the differential Eqs. (1), plus (2) and (3), and, finally, the method of modifying the interface shape in accord with Eq. (9).

IV. Details of the Solution Algorithm

A. Discretization and Solution by ADI

Equations (1), (2) and (3) were all solved using the ADI procedure of Peaceman and Rachford (see e.g., Richtmyer and Morton, 1967). In order to illustrate the procedure in our present context, it is convenient to express Eqs. (1), (2) and (3) in a standard form

$$0 = f^2 \frac{\partial^2 w}{\partial \xi^2} + \frac{\partial^2 w}{\partial \eta^2} + q_1 \frac{\partial w}{\partial \xi} + q_2 \frac{\partial w}{\partial \eta} + q_3 w + q_4 \tag{10}$$

in which the q's are coefficients that do not depend explicitly on w. The ADI procedure is then implemented by imbedding (10) in a fictitious time-dependent problem of parabolic type, and discretizing in such a way that derivatives in the spatial directions are alternately treated implicitly at one half-step in "time" and explicitly at the next half-step. Denoting the value of an independent variable at each full iteration n by a superscript, and the intermediate (half-step) value by ~ , we have

$$\frac{\tilde{w} - w^n}{(\Delta t/2)} = f^2 \frac{\delta^2 \tilde{w}}{\delta \xi^2} + \frac{\delta^2 w^n}{\delta \eta^2} + q_1^n \frac{\delta \tilde{w}}{\delta \xi} + q_2^n \frac{\delta w^n}{\delta \eta} + \left(\frac{q_3^n - |q_3^n|}{2} \right) \frac{\tilde{w} + w^n}{2}$$

(11a)

$$+\left[\frac{q_3^n + |q_3^n|}{2}\right] w^n + q_4^n$$

$$\frac{w^{n+1} - \tilde{w}}{(\Delta t/2)} = f^2 \frac{\delta^2 \tilde{w}}{\delta \xi^2} + \frac{\delta^2 w^{n+1}}{\delta \eta^2} + q_1^n \frac{\delta \tilde{w}}{\delta \xi} + q_2^n \frac{\delta w^{n+1}}{\delta \eta} + \left[\frac{q_3^n - |q_3^n|}{2}\right] \frac{\tilde{w} + w^{n+1}}{2}$$

(11b)

$$+\left[\frac{q_3^n + |q_3^n|}{2}\right] w^n + q_4^n$$

We utilize a uniform finite difference grid in the ξ,η coordinates, with control over mesh density affected by the form chosen for the distortion function $f(\xi,\eta)$. The symbols $\delta/\delta\xi$ or $\delta/\delta\eta$ are used in (11a) and (11b) to denote centered difference approximations of the indicated partial derivatives. The resulting systems of linear algebraic equations along each coordinate line are tridiagonal and can be solved very efficiently.

The only unusual feature of the discretization in (11a) and (11b) is that involving the term $q_3 w$ in (10). The "obvious" form, $q_3^n \frac{\tilde{w} + w^n}{2}$ for the first half-step and $q_3^n \frac{\tilde{w} + w^{n+1}}{2}$ for the second was found to lead to instability in the solution of the vorticity equation (2) for Re > 0(50), even with frozen ψ and boundary conditions. This instability was, at first, thought to be due to the use of centered difference approximations in the q_1 and q_2 terms. However, putting q_1 and q_2 identically to zero (for testing purposes) did not prevent instability, while $q_3 = 0$ did. It is evident that a differential equation of the form

$$\frac{\partial w}{\partial t} = q_3 w$$

will exhibit exponential growth of w if q_3 is positive. Such growth is, of course, restricted by other terms in the case of the differential Eq. (2) (at least for moderate R), but a precise cancellation may not occur at some intermediate step in the numerical solution of the same equation. In order to avoid this potential problem, the term $q_3 w$

was frozen at its level from the previous (nth) iteration if $q_3 > 0$, thus yielding Eqs. (11a) and (11b). The numeral scheme represented by Eqs (11) proved stable [R up to 0(200) was achieved in the application reported in part II, for example] and accurate (when compared with exact solutions such as the Hill's spherical vortex).

In practice, it was found that dividing the form (10) of the vorticity equation (9) by f^2 and then applying ADI [with large time steps $\Delta t = 0(10)$] improved the stability of the numerical computation at high R and W. We do not at present have a viable explanation for this observation.

B. Application of the Tangential Stress Condition

The condition (8) of zero tangential stress at the fluid interface is used to obtain the boundary vorticity values. In most cases, this can be done in the simple explicit manner

$$\omega^{n+1} = \omega^n - \beta_\omega(\omega^n - 2\kappa_{(\eta)}u_\eta^n) \tag{12}$$

pioneered by Dorodnitsyn and Meller (1968) and Israeli (1970) for a solid wall, and extended later for the case of a fluid-fluid interface by Rivkind and Ryskin (1976) (see Ryskin, 1980, for details). Here, β_ω is a positive relaxation parameter whose optimal value must be found by numerical experiment; typical values are $0(10^{-2} - 10^{-1})$.

The corresponding condition $\omega^{n+1} = \omega^n + \beta_\omega u_\eta^n$ for a solid boundary can be used effectively for any smooth boundary shape. However, in the case of a fluid-fluid boundary, the condition (12) leads to a stable computation of vorticity only for interfaces of convex shape (where $\kappa_{(\eta)} > 0$) or slightly concave shapes. For strongly concave interface shapes, condition (12) leads to instability.

In this latter case of a concave interface, an alternative implicit method was successfully implemented for calculation of the boundary vorticity. This method, first suggested by Ghia and Davis (1974), is much more complicated than the explicit method based on (12). The basic idea for any implicit scheme would be to determine

the relationship between the boundary values for u_η and the boundary values of vorticity, i.e. $u_\eta(\omega)$, thus giving from Eq. (8) (with $\kappa_{(\eta)}$ known) an equation for the vorticity, i.e.

$$\omega - 2\kappa_{(\eta)} u_\eta(\omega) = 0$$

The difficulty with this approach is to estimate $u_\eta(\omega)$ since u_η is obtained from the streamfunction [illegible] which, in turn, depends on the entire vorticity field, i.e. the dependence of u_η on the boundary values of ω is extremely complicated and nonlocal (u_η at some given boundary point depends on ω at all boundary points). Even if one were to assume heuristically that the dependence on local values of ω is most important, and seek to find this dependence, one would have to solve for new vorticity and streamfunction fields with ω varied at the point of interest and "frozen" at all other boundary points, and this would need to be done separately for every boundary point in turn. Such an approach is clearly out of the question due to the extreme expenditure of computer time that would be required.

However, Ghia and Davis (1974) suggested an idea to circumvent this difficulty. Instead of doing a full iteration on ω and ψ, one does a half-step in ω which is implicit along the lines normal to the boundary (i.e. along the ξ lines) and then immediately a half-step in ψ along the same ξ lines, using the new values of ω. Thus the interdependence on the direction parallel to the boundary is disconnected, and a single half-iteration on the whole field provides the necessary dependence of u_η on ω at the same boundary point for all boundary points at once. Of course, an error is introduced by using half-step values of ω and ψ instead of the full-step, but this error goes to zero with convergence, since the half-step and full-step fields are equal on the converged solution in ADI.

It may also be noted that the function $u_\eta(\omega)$ can be expressed ("locally") as a linear function of ω if the solution of the discrete equations for ω along the ξ lines (which are linear) is obtained as a sum of a "particular" solution, ω_p, with ω_p set equal to zero on

the boundary, and a "homogeneous" solution ω_H of the same equations with the right-hand side (i.e. the terms not including ω) set equal to zero but with a nonzero boundary value for ω_H (say, $\omega_H = 1$). The two resulting solutions for ω are then used separately to obtain two solutions of the discrete equations for ψ along the same ξ line (which are also linear) and the velocity at the boundary is then obtained as a sum of two parts — one "particular" part due to ω_p and one "homogeneous" part due to ω_H. Thus, if the actual vorticity is ω at the boundary, the velocity will be $u_\eta = u_{\eta p} + \omega u_{\eta H}$, and solution of (8) for ω, with u_η expressed as a linear function of ω, is a trivial task.

The rate of convergence of our numerical scheme is about the same with either the explicit or implicit prescription of boundary vorticity. Therefore, we used the implicit method, which takes more computer time, only for strongly concave interface shapes where the explicit scheme failed.

C. Use of the Normal Stress Balance to Determine Interface Shape

We have already indicated in section III that the steady shape of the free interface is determined in our solution scheme via an iterative process in which the imbalance between the total normal stress and capillary forces for a given estimated shape of the interface is used to obtain an "improved" shape for the next iteration — i.e. a shape for which the imbalance is decreased [or condition (9) more nearly satisfied]. Although a number of methods may be suggested for obtaining this improved estimate of boundary shape, the applications of the solution technique considered to date suggest a heuristic approach as providing the greatest degree of stability and most rapid approach to the final steady state. In effect, this approach is equivalent to considering any local excess of total normal stress to capillary forces, i.e.

$$\pi(\eta) \equiv \tau_{\xi\xi} - \frac{1}{W}\left(\kappa_{(\eta)} + \kappa_{(\varphi)}\right)$$

as a kind of normal "force" causing a local displacement of the interface in the direction of the "force"; the magnitude of the local displacement being proportional to $\pi(\eta)$.

Before going on to describe the detailed implementation of this simple heuristic method, it is, perhaps, worth dicussing briefly two alternatives which were not chosen. The most obvious would be to treat the normal stress boundary condition (9) as a nonhomogeneous differential equation for the boundary shape functions $x(1,\eta),\sigma(1,\eta)$ with the total stress $\tau_{\xi\xi}$ calculated from the streamfunction and vorticity fields corresponding to the interface shape at the previous iteration. However,this technique, utilized in an explicit scheme as described above, is not suitable for large values of W. This is because it assumes implicitly that the shape is determined by a balance between the total stress, $\tau_{\xi\xi}$ (including hydrostatic and dynamic pressure plus viscous stress contributions), and capillary forces, whereas for large W the capillary forces are negligible (except possibly in regions of very high curvature) and the interface shape is actually determined by the condition that the viscous stress, and the hydrostatic and dynamic pressure distributions balance in such a way that $\tau_{\xi\xi}|_{\xi=1} \approx 0$. Another possible method of calculating the steady interface shape is to treat the whole problem in a genuine transient mode, thus applying the two stress relationships (8) and (9) as boundary conditions to determine the instantaneous streamfunction and vorticity fields, and the kinematic condition [i.e. the transient generalization of (7)] to increment the interface position based on the magnitude and sign of the normal velocity at each point. Although this approach appears viable to us, and would, in fact, be necessary to obtain solutions in a transient problem, the means of using (9) as a boundary condition for determination of the streamfunction and vorticity fields is not obvious, and is likely, in any case, to yield a quite unstable solution algorithm since it involves derivatives of ψ and ω rather than the values themselves. It must be admitted, however, that we have not so far devoted much effort to this approach, and it may ultimately prove satisfactory for both transient and steady state calculations.

The prior efforts to compute free-boundary solutions utilized finite element techniques, cf. Silliman and Scriven (1980), Saito and Scriven (1981). Silliman and Scriven used either the normal stress or kinematic condition in the ways just described. As

expected, they found that the normal stress iteration diverged for low surface tension i.e. when a parameter, characterizing the relative magnitude of capillary pressure and stress, was below 0(1); while the kinematic iteration diverged when the same parameter was above 0(1). Eventually they had to abandon both of these approaches and switched to a global Newton's method (Saito & Scriven, 1981), with the free-boundary shape included in the system of equations and solved simultaneously with the dynamics. The Newton process has great advantages (quadratic convergence, generality, availability of the Jacobian matrix which can be used to trace nonunique solutions, etc.). But it also has some severe drawbacks, including the necessity to invert a huge Jacobian matrix (extremely time-consuming). The other problem with Newton's method is the need for a very good initial guess (e.g. Fornberg, 1980, in order to compute flow past a circular cylinder at R = 300, needed the solution at R = 297.5 as an initial guess). Fornberg (1980) also required 1-2 min. of computer time for a single case on the CDC STAR-100 computer which is $0(10^3)$ faster than our VAX-11/780, on which our algorithm takes from 15-60 min. for a single case (for comparable grids).

Let us now consider the details of our current technique, which is heuristic in concept, but is extremely simple and exhibits sufficiently rapid and stable convergence to the final steady state interface shapes.

As noted before, we modify the interface shape at each step in the overall iteration scheme by slightly moving points of the surface in the normal direction by an amount proportional to $\Pi(\eta)$ at the point. As explained in I, this cannot be done by prescribing new positions for the interface nodal points directly (and still maintain coordinate orthogonality), but must rather be done indirectly by changing the mapping itself via increments in the scale factor, h_ξ, at the boundary $\xi = 1$. We have shown in I that the increment in h_ξ can be expressed in terms of equivalent Neumann boundary conditions for the mapping functions, $x(\xi,\eta)$ and $\sigma(\xi,\eta)$. Thus

$$h_\xi^{n+1} = h_\xi^n + \beta_h \pi^n \tag{13}$$

where the new values of h_ξ are then used to calculate updated values of $\partial x/\partial\xi$ and $\partial\sigma/\partial\xi$ at $\xi = 1$, which provide the necessary boundary conditions for $x(\xi,\eta)$ and $\sigma(\xi,\eta)$. The coefficient, β_h, has to be determined by numerical experiment, its typical values being $0(10^{-3} - 10^{-2})$.

In many applications, including the two problems discussed in parts II and III, the interface completely encloses one of the two fluids —i.e. we then have a drop or bubble in a viscous fluid. In such circumstances, the local incrementation in the location of boundary points must be done in such a way as to preserve the bubble drop volume. Now, to first order, the change in volume between the nth and (n + 1)st iterations is

$$\int_0^1 \left(h_\xi^{n+1} - h_\xi^n\right)\sigma h_\eta \partial\eta \tag{14}$$

where the integral is taken along the boundary $\xi = 1$. Since,

$$h_\xi^{n+1} - h_\xi^n \sim \pi^n \tag{15}$$

it follows that

$$\int_0^1 \pi\sigma h_\eta \partial\eta = 0 \tag{16}$$

This provides a constraint on $\tau_{\xi\xi}$, which contains a free integration constant that can be chosen at each n so the constraint (16) is satisfied.

Even after this constraint has been satisfied, however, the bubble or drop may still change volume slightly at each iteration due to higher order effects [neglected terms in (14) and (15)] and numerical error. If left unchecked, these small changes may accumulate and eventually result in a gross error. To prevent this, a simple scaling of the whole mapping can be incorporated directly into the formula for h_ξ, i.e.

$$h_\xi^{n+1} = \left(\frac{4/3\pi}{V^n}\right)^{1/3} h_\xi^n + \beta_h \pi^n$$

where V^n is the volume of the bubble at the nth iteration, i.e.

$$V = \left| \pi \int_0^1 \left[\sigma^2 \frac{\partial x}{\partial \eta} \right]_{\xi=1} \partial \eta \right| .$$

The application of the algorithm described in this paper to the motion of deformable bubbles in a viscous fluid will be taken up in parts II and III of our present communication.

This work was supported by a grant from the Fluid Mechanics Program of the National Science Foundation.

References

Acrivos, A. & Lo, T. S. 1978 Deformation and breakup of a single slender drop in an extensional flow. J. Fluid Mech. **86**, 641-672.

Dorodnitsyn, A. A. & Meller, N. A. 1968 Approaches to the solution of stationary Navier-Stokes equations. U.S.S.R. Comput. Math. & Math. Phys. **8**(2), 205-217.

Fornberg, B. 1980 A numerical study of steady viscous flow past a circular cylinder. J. Fluid Mech. **98**, 819-855.

Ghia, K. N. & Davis, R. T. 1974 Corner layer flow: optimization of numerical method of solution. Comput. & Fluids **2**, 17-34.

Israeli, M. 1970 A fast implicit numerical method for time-dependent viscous flows. Stud. Appl. Math. **49**, 327-349.

Lee, S. H. & Leal, L. G. 1982 The motion of a sphere in the presence of a deformable interface. II. A numerical study of the translation of a sphere normal to an interface. J. Colloid & Interface Sci. **87**, 81-106.

Miksis, M., Vanden-Broeck, J.-M. & Keller, J. 1981 Axisymmetic bubble or drop in a uniform flow. J. Fluid Mech. **108**, 89-100.

Morse, P. M. & Feshbach, H. 1953 Methods of Theoretical Physics. McGraw-Hill.

Richtmyer, R. D. & Morton, K. W. 1967 Difference Methods for Initial-Value Problems. Interscience.

Rivkind, V. Y. & Ryskin, G. 1976 Flow structure in motion of a spherical drop in a fluid medium at intermediate Reynolds numbers. Fluid Dynamics 11, 5-12.

Ryskin G. 1980 The extensional viscosity of a dilute suspension of spherical particles at intermediate microscale Reynolds numbers. J. Fluid Mech. **99**, 513-529.

Ryskin,G. & Leal, L. G. 1983 Orthogonal mapping. J. Comput. Phys., to appear.

Saito, H. & Scriven, L. E. 1981 Study of coating flow by the finite element method. J. Comput. Phys. **42**, 53-76.

Silliman, W. J. & Scriven, L. E. 1980 Separating flow near a static contact line: slip at a wall and shape of a free surface. J. Comput. Phys. **34**, 287-313.

Taylor, G. I. 1934 The formation of emulsions in definable fields of flow. Proc. Roy. Soc. A **146**, 501-523.

Taylor, G. I. 1964 Conical free surfaces and fluid interfaces. Proc. 11th Int. Cong. Appl. Mech., Munich (H. Gortler, ed.), 790-796.

Taylor, T. D. & Acrivos, A. 1964 On the deformation and drag of a falling viscous drop at low Reynolds number. J. Fluid Mech. **18**, 466-476.

Youngren, G. K. & Acrivos, A. 1976 On the shape of a gas bubble in a viscous extensional flow. J. Fluid Mech. **76**, 433-442.

CHAPTER III

Large Deformations of a Bubble in Axisymmetric Steady Flows. Part 2. The Rising Bubble

by

G. Ryskin and L. G. Leal

Department of Chemical Engineering
California Institute of Technology
Pasadena, California 91125

Abstract

In this paper, numerical results are presented for the buoyancy-driven rise of a deformable bubble through an unbounded, quiescent fluid. Complete solutions, including the bubble shape, are obtained for Reynolds numbers in the range $1 \leq R \leq 200$ and for Weber numbers up to 20. For Reynolds numbers $R \leq 20$, the shape of the bubble changes from nearly spherical to oblate ellipsoidal to spherical-cap depending on Weber number; at higher Reynolds numbers "disk-like" and "saucer-like" shapes appear at $W = O(10)$. The present results show clearly that flow separation may occur at a *smooth* free surface at intermediate Reynolds numbers; this fact suggests a qualitative explanation of the often observed irregular (zigzag or helical) paths of rising bubbles.

J. Fluid Mech. (submitted)

1. Introduction

The buoyancy-driven motion of a deformed bubble through a quiescent fluid has been extensively studied by experimentalists (see references in section 4), but no theory exists except for the cases of very small deformation at either high (Moore, 1959) or low (Taylor and Acrivos, 1964) Reynolds number. The well-known analysis of the "spherical cap" bubble due to Davies and Taylor (1950) relates the speed of rise to bubble size, but the bubble shape is *assumed* on the basis of experimental observation rather than calculated as part of a full solution.

In addition to being an inherently interesting physical problem, the motion of a deformable bubble also represents a good example of the important class of free-boundary problems of fluid mechanics, from which one may anticipate obtaining a better understanding of both solution methods and the factors which control the boundary shape. The problem also affords the opportunity of investigating the rather poorly understood phenomenon of flow separation at a free boundary. The practical importance of bubble motions, ubiquitous as they are in nature and technology, is self-evident.

This paper represents the second in a three-part series on the solution of free-boundary problems at finite Reynolds number by a numerical, finite-difference scheme that is based upon the use of boundary-fitted, orthogonal coordinates that are generated as a part of the overall solution. The general features of the technique were described in part 1 of this series (Ryskin and Leal, 1983, hereafter referred to as I). Here, we consider the solution of the problem of a deformed bubble rising under the action of gravity for Reynolds numbers in the range $1 \leq R \leq 200$, and Weber numbers up to 20.

2. Problem Statement

The gas bubble is assumed to be of constant volume $4/3\ \pi a^3$, rising under gravity with velocity U in a quiescent, incompressible Newtonian fluid of viscosity μ, and

density ρ. The density and the viscosity of the gas inside the bubble are assumed to be negligible in comparison with those of the liquid, and the interface of the bubble is assumed to be characterized by a constant surface tension, γ (thus excluding surfactant effects from consideration). We restrict our attention to steady, axisymmetric bubble shapes — which are physically realizable in experimental studies up to R ~ 0(100-200) or even higher, depending upon the surface tension.

The problem is attacked numerically using a finite-difference approximation of the Navier-Stokes equations and boundary conditions on a curvilinear orthogonal coordinate system (ξ,η,φ) (see Fig. 1), which is connected with the conventional cylindrical coordinates (x,σ,φ), with x directed along the axis of symmetry, through the mapping functions

$$x(\xi,\eta),\ \sigma(\xi,\eta)$$

which can be obtained numerically given an approximation of the bubble shape, using the technique of orthogonal mapping given by Ryskin and Leal (1983) and I.

Utilizing the streamfunction, ψ, the governing differential equations and boundary conditions can be expressed in terms of the (ξ,η,φ) system as

$$L^2(\omega\sigma) - \frac{R}{2}\frac{1}{h_\xi h_\eta}\left\{\frac{\partial\psi}{\partial\xi}\frac{\partial}{\partial\eta}\left[\frac{\omega}{\sigma}\right] - \frac{\partial\psi}{\partial\eta}\frac{\partial}{\partial\xi}\left[\frac{\omega}{\sigma}\right]\right\} = 0 \tag{1}$$

and

$$L^2\psi + \omega = 0 \tag{2}$$

where

$$L^2 \equiv \frac{1}{h_\xi h_\eta}\left\{\frac{\partial}{\partial\xi}\left[\frac{f}{\sigma}\frac{\partial}{\partial\xi}\right] + \frac{\partial}{\partial\eta}\left[\frac{1}{f\sigma}\frac{\partial}{\partial\eta}\right]\right\},$$

h_ξ, h_η are the scale factors for the ξ,η,φ coordinate system, $R \equiv 2\rho Ua/\mu$ is the Reynolds number and ω is the azimuthal vorticity component. The corresponding boundary conditions are

$$\psi = \omega = 0 \text{ at } \eta = 0 \text{ and } \eta = 1 \text{ (symmetry)} \tag{3}$$

$$\psi \sim \frac{1}{2}\sigma^2, \quad \omega \to 0 \text{ for } \xi \to 0 \text{ (infinity relative the bubble)} \tag{4}$$

with

$$\psi = 0 \text{ (zero normal velocity)} \tag{5}$$

$$\tau_{\xi\eta} = 0 \text{ (zero tangential stress)} \tag{6}$$

and

$$\tau_{\xi\xi} - \frac{4}{W}\left[\kappa_{(\eta)} + \kappa_{(\varphi)}\right] = 0 \text{ (normal stress balance)}$$

at $\xi = 1$, the bubble surface. Here $\kappa_{(\eta)}$ and $\kappa_{(\varphi)}$ are the normal curvatures of the bubble surface in the directions of the η and φ coordinate lines, W is the Weber number, $W \equiv \frac{2\rho U^2 a}{\gamma}$ and $\tau_{\xi\xi}$ contains the difference between pressures inside and outside the bubble, as well as dynamic contributions. The curvatures are defined as positive for a convex shape, like a sphere, since the unit vector of the ξ-coordinate serves as the unit normal to the interface and is directed inward. As explained in a general way in I, the tangential stress condition is used to obtain values for the vorticity at the bubble surface, and the normal stress condition is used to determine the bubble shape.

Expressions for the normal curvatures $\kappa_{(\eta)}$ and $\kappa_{(\varphi)}$ are obtained easily in terms of the so-called connection coefficients of the ξ,η,φ coordinates, as shown in Ryskin and Leal (1983). In particular,

$$\kappa_{(\eta)} = -\frac{1}{h_\eta h_\xi}\frac{\partial h_\eta}{\partial \xi} \tag{7}$$

$$\kappa_{(\varphi)} = -\frac{1}{\sigma h_\xi}\frac{\partial \sigma}{\partial \xi}.$$

However, from a computational point of view, it is more convenient to differentiate parallel to the interface rather than normal to it and to avoid differentiation of a scale

factor. Thus, using the general properties of an orthogonal mapping (Ryskin and Leal, 1983),

$$\kappa_{(\eta)} = \frac{1}{h_\eta^3}\left[\frac{\partial x}{\partial \eta}\frac{\partial^2 \sigma}{\partial \eta^2} - \frac{\partial^2 x}{\partial \eta^2}\frac{\partial \sigma}{\partial \eta}\right]$$

$$\kappa_{(\phi)} = -\frac{1}{\sigma h_\eta}\frac{\partial x}{\partial \eta} \tag{8}$$

The tangential stress condition, $\tau_{\xi\eta} = 0$, can be shown to be equivalent to the condition

$$\omega - 2\kappa_{(\eta)} u_\eta = 0\,; \quad \xi = 1 \tag{9}$$

relating the surface vorticity and surface curvature. Finally, for use in the normal stress condition, we have

$$\tau_{\xi\xi} = -p + \frac{8}{R} e_{\xi\xi} = -p - \frac{8}{R}\frac{1}{\sigma h_\eta}\frac{\partial}{\partial \eta}(\sigma u_\eta)\,. \tag{10}$$

To obtain the pressure on the interface, we use the equation of motion in the form

$$\nabla(p + \underline{u}^2) = \frac{2ag}{U^2}\underline{i}_x + 2(\underline{u} \wedge \underline{\omega}) - \frac{4}{R}\mathrm{curl}\,\underline{\omega} \tag{11}$$

At steady state

$$\frac{2ag}{U^2} = \frac{3}{4}C_D$$

where

$$C_D \equiv \frac{\text{drag force}}{\frac{1}{2}\rho U^2 \pi a^2}$$

Thus, the η-component of (11) at the bubble surface gives

$$\frac{1}{h_\eta}\frac{\partial}{\partial \eta}\left[p + u_\eta^2 - \frac{3}{4}C_D x\right] = -\frac{4}{R}\frac{1}{\sigma h_\xi}\frac{\partial}{\partial \xi}(\sigma\omega)$$

or, upon integration

$$p = \frac{3}{4}C_D x - u_\eta^2 - \frac{4}{R}\int \frac{f}{\sigma}\frac{\partial}{\partial\xi}(\sigma\omega)\partial\eta + \text{const} \tag{12}$$

in which $\frac{3}{4}C_D x$ is the hydrostatic pressure contribution, p_{hs}, and the remainder is the dynamic pressure terms, p_{dyn}.

It may be noted that the expression (12) for the pressure contains a free constant of integration, which is a consequence of the incompressibility assumption. This constant is determined in the numerical computation from the constraint (of incompressibility) that the bubble volume be constant using the method described in I.

The drag coefficient, required in (12), is calculated from the equation

$$C_D = 2\int_0^1 \left[-p_{dyn} + \frac{8}{R}e_{\xi\xi}\right]\sigma\,\frac{\partial\sigma}{\partial\eta}\partial\eta\ . \tag{13}$$

3. Numerical Method

The general features of a numerical algorithm for free-boundary problems of the type exemplified by the present problem were presented in part I of the present series. Here, we concentrate only on those aspects of the numerical methods which are unique to the present problem.

First, the orthogonal mapping methods outlined in Ryskin and Leal (1983) for an infinite domain were adopted here. In particular, the mapping process is carried out in two steps: first, a conformal mapping of the form $x + i\sigma = (x^* - i\sigma^*)^{-1}$ is used to invert the infinite physical domain into a finite auxiliary domain; and then, an orthogonal mapping transforms from the finite auxiliary domain to the ξ,η plane. Second, a distortion function of the form $f = \pi\xi(1 - \frac{1}{2}\cos\pi\eta)$ was adopted because it leads to a denser grid downstream of the bubble, where it is desirable in order to give better resolution of the wake structure. Third, a minor change is required in condition (13) of I due to the fact that the final mapping is obtained from the auxiliary mapping $x^*(\xi,\eta)$, $\sigma^*(\xi,\eta)$ by the above inversion. This means that a point on the boundary $\xi = 1$

of the auxiliary mapping should be moved inward if the corresponding point of the final mapping is to move outward corresponding to positive $\mathcal{R}(\eta) \equiv \tau_{\xi\xi} - \frac{4}{w}(\kappa_{(\eta)} + \kappa_{(\varphi)})$. Thus, condition (13) of I must be modified to the form

$$h_\xi^{*(n+1)} = h_\xi^{*(n)} - \beta_h(\tau^*)^2\mathcal{R}^{(n)} \quad at \quad \xi = 1 \tag{14}$$

where the factor $(\tau^*)^2$ is inserted because the scale factors for the auxiliary and orthogonal mappings are related according to $h_\xi = h_\xi^*/(\tau^*)^2$. Fourth, and finally, the singularity which occurs in ψ at $\xi = 0$ (in the transform domain) as a consequence of the condition (4) at infinity (in the physical domain) is removed by subtracting a function which has the same form for $\sigma >> 1$ but preserves the homogeneous boundary conditions on ψ at the other three boundaries

$$\psi^* \equiv \psi - \frac{1}{2}\sigma^2(1 - \xi^3) \tag{15}$$

The subtracted term is the irrotational flow solution for a spherical bubble, but has no simple interpretation when the bubble shape is nonspherical. The modification (15) leads to an equation for ψ^*, derived from equation (2), of the form

$$L^2\psi^* + \omega - \frac{1}{2}L^2(\sigma^2\xi^3) = 0$$

From the Oseen solution, we know that ψ^* is bounded at infinity, $\xi = 0$. This point is a singular point of the differential equation, and boundedness is therefore a sufficient condition for solution (see e.g. Morse and Feshbach, 1953, pp. 713-716). Numerically, any 0(1) number (say, 0) can be used as a boundary condition for ψ^* at $\xi = 0$, with the particular choice influencing the solution by no more than the order of accuracy of the numerical scheme.

The overall scheme for solution of the four elliptic equations, [(1,2) and the two equations for the mapping functions $x^*(\xi,\eta)$ and $\sigma^*(\xi,\eta)$], subject to the boundary conditions indicated earlier for ψ^*, ω and in I for the mapping functions, has already been described in I. In the present case, all of the basic computations were performed on a

40x40 grid in the ξ,η domain, $0 \leq \xi,\eta \leq 1$. A number of checks were made to assess the accuracy of the resulting solutions. One was to insure that the final bubble shapes were consistent with the geometric constraint that is known as the Gauss-Bonnet theorem (cf. Sokolnikoff, 1964). This theorem states that the integral of the total (Gaussian) curvature K over a smooth surface, topologically equivalent to a sphere, should equal 4π. Since the normal curvatures $\kappa_{(\eta)}$ and $\kappa_{(\varphi)}$ are also the principal curvatures (Dupin's theorem, see Sokolnikoff, 1964, p. 195), we have $K = \kappa_{(\eta)}\kappa_{(\varphi)}$, and the integral is computed easily. The final bubble shapes always satisfied the Gauss-Bonnet theorem to within 1%.

A second check was more physical, and involved comparisons between the drag coefficients computed, respectively, on the basis of the total rate of energy dissipation via the Bobyleff-Forsythe formula (see Ryskin, 1980) and by integration of the pressure and viscous stresses over the bubble surface. It may be anticipated that the latter values, dependent only on surface quantities, should be the more accurate of the two, and the surface force integration was adopted as our basic method. The drag coefficients calculated by the two methods were found to be in good agreement in most cases (see Table 1). The level of agreement was actually quite surprising since the dissipation calculation involves integrating the squared vorticity over the whole solution domain — an operation which magnifies the effects of errors in the vorticity at large distances away from the bubble. However, at the largest values of R and W the differences were much larger. We believe that these differences in the calculated drag coefficients provide a conservative view of the accuracy of our numerical solutions. As we have already noted, the dissipation calculation weighs heavily the vorticity values at a large distance from the bubble surface, and this is just the point where one might expect the largest errors to appear. Indeed, for the highest R and W considered, some evidence of "numerical noise" was present in the vorticity fields far from the bubble and recirculating wake, indicating that we are approaching the limits of usefulness of the 40x40 mesh. It should be noted, however, that relatively small errors in the

vorticity at large distances from the bubble ($\leq$ 2% of ω_{max}), especially downstream and outside the wake, would not be expected to influence the solution much in the vicinity of the bubble surface. Support for this point of view may be found in the recent work of Fornberg (1980) who showed that the major effect of downstream boundary conditions on the accuracy of numerical solutions for streaming flow past a cylinder was in the streamfunction, with the precise form of the vorticity boundary conditions playing a relatively minor role. The calculated drag coefficients for all cases considered are given in Table 1.

Finally, as indicated above, a comparison was made for one case, R = 20 and W = 12 (a highly deformed bubble), with solution obtained on a finer 80x80 grid. The computations on the 40x40 grid took approximately 15-60 minutes of CPU time on a VAX 11/780 for each case, starting with the solution at the same R and the next lower value of W as an initial condition. The solution on an 80x80 grid required more than order of magnitude increase in computer time and therefore was computed only for a single case. As can be seen from Fig. 2, the only noticeable difference in the 40x40 and 80x80 solutions in this particular case is in the intensity of motion inside the recirculating wake (whose shape is virtually identical). Since the velocities in this region are extremely small anyway (the magnitude of ψ at the innermost streamline is only 0.01), we judge the absolute error to be acceptably small. The value of the drag coefficient is about 3% lower on the finer grid, and this probably should be used to suggest that all of the drag coefficients from the 40x40 mesh system are going to be a little above the true values.

4. Summary of Experimental Observations

The experiments of Haberman and Morton (1953), Saffman (1956), Hartunian and Sears (1957), Hnat and Buckmaster (1976), Bhaga and Weber (1981) and others provide a fairly detailed picture of the motion of gas bubbles through a quiescent, viscous liquid. It is convenient to describe their results in terms of the dimensionless parame-

ter, $M \equiv g\mu^4/\rho\gamma^3$, which is related to our parameters according to

$$M = \frac{3}{4} C_D \frac{W^3}{R^4}$$

The variation of M in pure liquids is mainly due to variations in viscosity; M varies from $O(10^{-13})$ in liquid metals to $O(10^5)$ in viscous oils. Water has $M = O(10^{-10})$.

In high-M liquids ($M \geq 4 \times 10^{-3}$ according to Bhaga and Weber, 1981), the flow past a bubble is steady if $R \leq 110$ (for $R > 110$, the wake becomes unsteady) and the shape depends mainly on R, changing from spherical for $R \leq 0.1$, to oblate ellipsoidal, to ellipsoidal cap and finally to spherical cap (Hnat and Buckmaster, 1976; Bhaga and Weber, 1981).

In low-M liquids the bubbles likewise change from spherical to oblate ellipsoidal at low R and have a spherical-cap shape at large R. However, the transition between these regimes does not pass through a sequence of steady shapes as in the high-M case. First, when the bubbles are still only slightly deformed at $W = O(3)$ and $R \geq 200$, their path becomes zigzag or helical (Hartunian and Sears, 1957). At higher R and W, the path becomes rectilinear again, but the bubble becomes very flattened in shape, and fluctuates violently (Saffman, 1956). Finally, at $W \geq O(30)$, the bubble assumes a stable spherical cap shape but with a very sharp (often ragged) rim and unsteady or turbulent wake (Wegener and Parlange, 1973).

Our numerical solution technique is restricted to steady and axisymmetic laminar flows. In effect, we attempt to obtain steady, axisymmetric solutions without questioning their stability (and, hence, realizability) in the real, physical situation. Although a failure of the numerical procedure to converge may sometimes be indicative of a physical instability, this is by no means obvious and should not be automatically construed in that light. A common feature of many problems is the existence of a steady solution for a given set of parameters where the steady solution would not be realizable due to the presence of an instability or bifurcation. Such steady solutions may still be of con-

siderable interest in understanding the asymptotic nature of the governing equations and boundary conditions. In the present work, we attempt to achieve steady, axisymmetric solutions for both low- and high-M conditions.

5. Results of the Numerical Computations

We have computed solutions for R in the range $1 \leq R \leq 200$ and W from 2 up to 20 for $R \leq 20$ and up to 10 for $R \geq 50$. All these cases are listed in Table 1. In addition, several solutions were obtained for $R = 0.5$ for comparison with the low Reynolds number, small deformation theory of Taylor and Acrivos (1964). The limits on W are a consequence of the very large values of curvature which occur at the rim of the bubble, in combination with the use of a 40x40 mesh for the calculations.

(a) Drag Coefficients

Our results for the drag coefficient are presented in Fig. 3 for the cases with $R \geq 1$. Several solutions were also obtained for $R = 0.5$, as indicated above, and the comparison between these solutions and the small R, small deformation theory of Taylor and Acrivos (1964) is shown in Table 2. These latter results suggest that the Taylor-Acrivos theory is quantitatively accurate only for $R \leq 0.5$, $W \leq 0.5$, where the deformation is very small (see section (b) below).

Bhaga and Weber (1981) found that the drag coefficient (and the shape) depended only on R for high-M liquids (i.e. for $M \geq 4 \times 10^{-3}$). In the context of our solutions, this should imply that the drag coefficient and shape become independent of W for any fixed R at sufficiently large W. Bhaga and Weber (1981) gave an empirical formula for the drag coefficient for high-M liquids (i.e. for large W in our framework), namely

$$C_D = \left[(2.67)^{0.9} + \left(\frac{16}{R} \right)^{0.9} \right]^{1/0.9} ,$$

and the values of C_D calculated from this formula are shown in Fig. 3 together with our numerical results. For $R \leq 20$, and sufficiently large W, there is obviously good

agreement between our results and the empirical, large-M formula of Bhaga and Weber (1981) for the drag coefficient. However, it should be noted that the value of W required for each R does not correlate well with a fixed critical value of M, and, in any case, the corresponding values of M are considerably larger than 4×10^{-3}. Thus, though our results for $R \leq 20$ show asymptotic behavior in full agreement with the empirical formula, the latter must apparently be viewed as an asymptotic result for sufficiently large W, rather than a universally valid result for high-M liquids. It is evident that the value of W required for good comparison with Bhaga and Weber's experimental asymptote does increase with increasing Reynolds number. The values of W which we could achieve for $R \geq 50$ were apparently not large enough, though this should not be considered as suggesting that the asymptotic behavior would not appear for higher W.

A byproduct of beginning our calculations from a spherical shape at each value of R is the results for the drag coefficient for a spherical bubble at each R (in effect, the solution for $W = 0$ shown in Fig. 3). These results are in essential agreement with the results of numerical computations for spherical bubbles by Brabston and Keller (1975) and Rivkind and Ryskin (1976). The latter authors also demonstrated good agreement with experimental data for cases where the actual bubble shapes are nearly spherical.

Experimental data corresponding to $R \geq 50$ and $W \leq 10$ do not apparently exist. Such cases would correspond roughly to liquids with $0(10^{-7}) < M < 0(10^{-3})$. However, the experiments would be more difficult than those with high-M liquids because the small bubbles required to achieve modest R in the range 50-200 would be highly susceptible to the influence of surface active impurities. In addition, even if such experiments did exist, it is quite possible that the bubbles at these R and W would rise in a zigzag or spiral path, thus rendering any comparison with the present solutions meaningless.

(b) Bubble Shape

The computed bubble shapes for all cases considered, except R = 0.5, are shown in Fig. 4. Results for R = 0.5 and W = 0.5 and 1 are given in Fig. 5, along with the shapes calculated for these cases from the asymptotic formula of Taylor and Acrivos (1964). As was also true for the drag coefficients, quantitative agreement with this small R, small W asymptotic theory is evidently possible only for W and R ≤ 0.5 where the deformation is very small indeed. Let us now turn to the more general results represented by Fig. 4, beginning with cases for R ≤ 20.

We may first note that, for Re ≤ 20, the progression of bubble shapes is in accord with qualitative "expectations" based on the most commonly reported experimental observations, namely spherical to oblate ellipsoid to more complicated "oblate" shapes with indentation and/or flattening at the rear.† Furthermore, as W reaches 0(15), for R ≤ 0(20), the shape of the bubble becomes visually independent of W, in agreement with the experimental observations of Bhaga and Weber (1981). It may be noted that direct comparison with the photographs of Bhaga and Weber (1981) is possible in some cases, e.g. our result for R = 2, W = 16 with their photo for R = 2.47 and W = 16.5 (their Fig. 3a), but the majority of their experimental results are for very high Weber numbers compared to those attained in the present work.

Although the bubble shapes for W ≥ 0(15) appear visually similar at any fixed R ≤ 20, as noted above, our computations show that the influence of W does still persist in this range in the vicinity of the bubble rim where the local curvature continues to increase with W. Evidently, two bubbles may have quite different local curvatures at the rim and still have almost identical overall shapes. The local differences in curvature with increase of W are, however, quite important for the flow fields, which continue to change with W even after the overall bubble shape is visually constant —it may be seen

† It should be kept in mind, however, that typical experiments do not hold either R or W constant, but rather the parameter M with the independent dimensional parameter being the bubble volume. An increase in bubble volume with M held constant yields an increase in W proportional to u^2a and an increase in R proportional to ua.

from the condition (9) of zero tangential stress that the amount of vorticity generated at any point on the bubble surface is proportional to the local curvature. The resultant changes in the vorticity and velocity fields with W (see Fig. 7 for R = 20) do not, however, seem to feed back to have strong influence on the bubble shape.

In its present form, our numerical technique is not well suited for handling very high surface curvature. We did not, therefore, compute any solutions for $W > 20$, and cannot do more than speculate as to the asymptotic nature of the flow for large W and $R \leq 20$. In the low R number range, it appears likely that the final asymptotic shape will not differ much, in an overall sense, from the highest W results of Fig. 4. However, the curvature at the rim and consequently the amount of vorticity in the wake may well grow indefinitely with W. The existence of "skirts" at the rim (cf. Hnat and Buckmaster, 1976) may suggest that a value of W exists for any R beyond which surface tension can no longer balance the local "pulling" action of dynamic forces at the rim, but this is pure speculation at the present time.

In spite of the fact that shapes in which the deformation is strongest at the rear (eventually leading to spherical caps) have become accepted as the "natural" mode of deformation, it is not easy to explain why this should occur. At steady state, all deformation is a consequence of local imbalances between hydrostatic and dynamic (normal) stresses which must, on the other hand, balance exactly in a certain global (i.e. integral) sense in order that the resultant force on the bubble be zero. In the case R = 0, both static and dynamic forces are linear functions of vertical position (i.e. of x in our notation) and thus must also balance locally leading to a spherically shaped bubble for any surface tension. For nonzero Reynolds number, on the other hand, deformation will occur in a form that depends wholly on the details of any local imbalance between the static and dynamic normal stress contributions and these details are nearly impossible to anticipate in any "a priori" sense. Examination of the surface distributions of hydrostatic pressure, dynamic pressure and the normal component of viscous stress, given in Fig. 6 for R = 2, W = 16, shows that the hydrostatic pressure

contribution is locally dominant at the rear of the bubble thus leading to an indentation in that part of the bubble. While this fact may be associated, after the fact, with a leveling of the dynamic normal stress contributions from their initially linear dependence on x (caused by the sweeping of vorticity to the rear of the bubble?) no satisfactory "a priori" explanation seems possible. Indeed, a striking feature of the bubble shapes for high W and $R \leq 20$ is that they can be closely approximated by intersecting segments of two spheres of different radii. This means that two strongly varying functions (the hydrostatic pressure and the dynamic normal stress) add up to one of two constant values everywhere on the bubble surface except in the local vicinity of the rim (see Fig. 6 for R = 2, W = 16). Apparently, as $W \to \infty$, the sum of hydrostatic and dynamic forces will approach a δ-function located at the rim, though we can offer no real insight as to why this should be the case for a shape consisting of two spherical segments (including a plane as a limiting case of a sphere).

Let us now consider the results for the higher Reynolds numbers, $R \geq 50$. As can be seen from Fig. 4, at these Reynolds numbers the (front) stagnation pressure becomes dominant and the bubble initially flattens more at the front than at the back. Eventually, for R = 100 and 200, the bubble actually develops an indentation in this area. Miksis, Vanden-Broeck and Keller (1981) have also found bubble shapes in *potential* flow with an indentation at the front, but in that case the bubble shape must remain fore-aft symmetric so that the overall shape resembles a donut without the hole. In the real viscous flow, the rear stagnation pressure does not reach the same value as the front stagnation pressure (see Fig. 6 for R = 100, W = 10), and the deformation is greater in the front as shown in Fig. 4. The case of R = 50 lies approximately on the border between two types of deformation: one characteristic for lower R with stronger deformation in the rear, and another characteristic for higher R, with stronger deformation in the front. Consequently, at R = 50 the bubbles almost preserve fore-aft symmetry, leading at higher Weber numbers to the shapes which Bhaga and Weber (1981) termed "disk-like" (see the photograph in their Fig. 2c for R = 55.3 and W = 15.4). They

note that these bubbles wobbled as they rose. Observations of saucer-like shapes such as those illustrated in Fig. 4 for $R \geq 100$ and $W = O(10)$ have also been reported in the literature (see e.g., Lane and Green, 1956), but we were unable to find any photographs for comparison. It is quite likely that this is a consequence of the fact that the real bubbles do not rise steadily at the highest Reynolds and Weber numbers which we attained in our computations, but rather wobble or rise along a zig-zag or helical path (see section 6 below). Since these latter phenomena cannot be predicted in our present studies which assume the flow and bubble shapes to be steady and axisymmetric, a natural question is the purpose of obtaining solutions for the higher values R and W that are represented in Fig. 4. We would assert that such solutions are of considerable importance, even if they are unstable in reality, because they can demonstrate important trends toward asymptotic behavior (see e.g., Saffman, 1981). In classical fluid mechanics, an equivalent problem is the quest to develop steady, asymptotic solutions for separated flows at high Reynolds number even though experimental observation shows such solutions to be unstable if they exist at all.

A case in point in the present study is the evolution with increasing Weber number, and $Re \geq 100$, of flatter and flatter shapes with an indentation in front, and the concomitant lack of any apparent tendency toward spherical cap shapes which are known experimentally to occur for $W \geq O(30)$ at these Reynolds numbers (see Bhaga and Weber, 1981), following a regime of unsteady motions and shapes at lower W. Indeed, the trend of the present solutions with increasing W would appear to support the proposition that no steady solutions of this branch (i.e. increasingly flattened bubbles with increasing W) can exist above some critical W which will depend upon the Reynolds number R. In particular, the occurrence of increasingly flattened bubbles for higher W is likely to lead eventually to a situation in which a further increase in Weber number, and thus deformation, will not lead to an equilibrium shape because the dynamic forces associated with the local increase in curvature will increase faster than surface tension forces. Results of precisely this type were reported for *potential* flow past an

axisymmetric bubble by Miksis et al. (1981) who found a critical Weber number of 3.2. Restrictions in the present solution technique prevent us from extending the solutions at R = 100 and 200 beyond W = 10 and we can thus neither *prove* that solutions of the branch attained here do not exist for $W > W_c$, nor provide a numerical estimate of the critical Weber number, W_c, for the finite Reynolds numbers considered here. In particular, the rate of convergence using our particular iterative algorithm for bubble shape slows considerably at these higher values of R and W. In addition, the 40x40 grid is not sufficiently fine to merit extension of the present solutions to larger R or W, while the use of a finer grid is currently too costly. The fact that we cannot yet obtain results at larger W does not, however, diminish the potential value of extending the range of steady, axisymmetric solutions beyond the point of experimentally observed instability. The use of such solutions in the present problem to establish the nonexistence of the branch of flattened shapes beyond some critical $W = W_c(R)$ would presumably signal the onset of "shape instabilities" which may account for the violent fluctuations and irregularities of shape that are observed experimentally before the bubble attains a spherical cap shape (Saffman, 1956). In spite of the current restrictions on maximum W, we believe that the solutions shown in Fig. 4 for R = 100 and 200 are indicative of just such a result (though, as already noted, we cannot yet pinpoint a critical value for W at these Reynolds numbers). Note that "shape instability" associated with the nonexistence of steady, axisymmetric solutions for bubble shape should be distinguished from non-axisymmetric shapes caused by non-rectilinear trajectories that result from intrinsically unsteady wake flows (termed "path instability"). The "instability" of the "path" occurs when the bubble is still only slightly deformed (cf. Hartunian and Sears, 1957), and is of a completely different nature than the instability of shape associated with a large, super-critical deformation. We will discuss this point in more detail in section 6 below. However, the fact noted by Miksis et al. (1981) that the instability of the trajectory (or path) often occurs at Weber numbers very near the critical value (3.2) for shape instability in *potential* flow is purely coincidental. The "path instability" *can-*

not be predicted if the flow is assumed axisymmetric and steady from the outset, as is done in both potential solutions (cf. Miksis et al., 1981) and in our computations, while the "shape instability" implies nonexistence of steady axisymmetric solutions above some Weber number and thus will manifest itself quite clearly under the above assumptions.

It is relevant to note that the branch of solutions exhibiting increased flattening with W was generated here by holding R constant and gradually increasing W starting with a sphere for W = 0. It is quite possible that the spherical-cap branch of solutions for $R \geq 0(100)$ could be reached numerically by first computing spherical cap bubbles for R = 0(20) and W = 0(30) —where they must presumably exist as an extension of our present solution for R = 20, W = 20 —and then increasing R while holding W constant. However, we have not yet attempted to attain spherical caps by this route, pending changes in the numerical scheme to better accommodate local regions of high surface curvature.

Finally, it may be noticed from Fig. 4 that the dependence of the shape on Reynolds number becomes rather weak for $R \geq 0(100)$. It is not clear, however, if this means that the solution is near its asymptotic form for $R \to \infty$ or that the values of R = 0(100) correspond to a "plateau" region in the dependence of the shape and flow structure on the Reynolds number. Nor can one discard the possibility that this behavior is (at least partly) an artifact of the numerical scheme working at its limits of accuracy.

(c) Flow Structure-Separation at a Free Surface

In different branches of fluid mechanics flows with free surfaces at high Reynolds numbers are treated as irrotational. This is a good approximation if the flow does not separate since then the velocity at the free surface will differ from its irrotational value by a small amount proportional to $R^{-1/2}$ (see Batchelor, 1967, section 5.14). If the flow separates, however, the entire structure of the flow field will be changed and the assumption of irrotational flow is not useful. It is therefore quite important to

understand if such separation may indeed occur at a free surface and under what conditions. We are not aware of any theoretical or numerical work in this area. There appears to exist a belief that a flow does not separate from a smooth free surface but may separate if a free surface has a sharp edge (see e.g., Batchelor, 1967, sections 5.14 and 6.11).

At intermediate Reynolds numbers, flow separation can be studied numerically, and the present problem provides an excellent opportunity for such study. Our results (see Figs. 7) show that separation not only occurs at a smooth free surface, but that the size of the separated flow region may be very substantial. The onset of separation depends on both Reynolds and Weber numbers. Very roughly, it occurs at $W \approx 9$ for $R = 10$, at $W \approx 7$ for $R = 20$, at $W \approx 5$ for $R = 50$, at $W \approx 4$ for $R = 100$ and at W between 3 and 4 for $R = 200$. The size of the separated region grows with both R and W, though at $R = 0(100)$ the dependence of this size on R is rather weak, similar to the situation for the shape of the bubble, discussed at the end of section 5(b). The present solutions also show that the dividing zero streamline leaves the surface of the bubble at a large angle, though the fine structure of solution near the point of detachment cannot be studied on our relatively coarse grid.

An obvious question is whether the streamline patterns and shapes shown in Figs. 4 and 7 are realistic, especially since the existence of separation from a smooth, zero shear stress surface is not, perhaps, easily accepted by all workers in the field. To answer this question, the most effective course is comparison of our calculated solutions with actual photographs. We could only find one example of a photograph which clearly showed a standing eddy structure downstream and also had values of R and W matching closely one of our numerical cases. A comparison of the computed and experimental bubble shape and wake structure is shown in Fig. 8. As noted, the photograph was taken from the study of Hnat and Buckmaster (1976). The experimental and numerical results for both shape and streamline pattern compare extremely well. It should be noted that the indentation at the rear of the bubble is visible in the

original published photo though somewhat obscured by the fact that we look through the edge of the bubble. It is, however, more difficult to discern in our reproduction of the Hnat-Buckmaster photo.

How can one explain the appearance of separation in this flow with a free surface? We believe that the best explanation is the evolution-type argument due to Batchelor (1967, section 4.12), according to which the separation per se is a secondary occurrence while the primary phenomenon is the development of standing eddies behind the body due to the accumulation of vorticity brought to this area by convection. The crucial evidence in support of this view is the fact that while separation in laminar flow is always accompanied by standing eddies, the standing eddies behind a body may exist without separation, as observed experimentally for a bluff body with base bleed by Leal and Acrivos (1969), and found numerically for a spherical viscous drop by Rivkind and Ryskin (1976). Clearly, the eddies are primary and the separation secondary. However, unless something prevents the standing eddy from attachment (base bleed, internal motion in the drop), the eddy will attach and thus cause separation.

According to the viewpoint expressed above, the key condition for existence of standing eddies (and hence separation) is the generation of vorticity at a sufficient rate from the bubble surface. As is evident from condition (9), this implies the existence of sufficiently large curvature, i.e. bubble deformation. Since the shape of a bubble depends on both the Reynolds number and Weber number, it is difficult to separate the effects of these parameters on the existence of standing eddies (and separation), especially in view of the fact that the Reynolds number is also indicative of the relative efficiencies of convection and diffusion in the transport of vorticity. It can be seen, however, that no separation occurs at any of the Reynolds numbers considered here when the bubble is spherical in shape (i.e. $W = 0$) —a result also confirmed by earlier numerical studies due to Brabston and Keller (1975) and Rivkind and Ryskin (1976) for spherical bubbles. This is presumably due to the fact that the surface

curvature and hence boundary vorticity is not sufficiently large for a sphere. As W increases, however, bubble deformation increases, as do the maximum surface curvature and vorticity and it is not surprising to find separation occurring for a particular Reynolds number at some critical value of W (dependent on R). Our numerical results show that the deformation need not be all that great to yield sufficient vorticity to give standing eddies; the maximum boundary vorticity at the onset of separation is of the order 4-10, being smaller for lower Reynolds numbers (i.e. for more bluff shapes).

Although experimental photographs have been published by a number of authors, including the Hnat-Buckmaster (1976) study cited earlier, which show clear evidence of separation, there has been a reluctance to accept this result as unequivocal evidence for separation from a free interface. In particular, in the experiments, it is never clear that the interface is completely free of surfactants, temperature gradients or other impurities which could change the boundary conditions and thus conceivably account for the existence of separation. The present numerical results, on the other hand, do satisfy the zero shear stress condition to within a small numerical error and thus provide a clear demonstration of flow separation from a smooth free surface, at least for intermediate Reynolds numbers. *Consequently, the usual assumption that flow near a smooth free surface will correspond closely to potential flow at high Reynolds numbers cannot be taken for granted, but requires additional investigation in each case!*

6. Discussion

Finally, in this section, we consider some further implications of our numerical results for the conditions for existence of the unsteady and/or non-axisymmetric motions observed by Saffman (1956), Hartunian and Sears (1957), and many other investigators. As noted in the description of experimental results, these motions consist of zigzag or helical trajectories for sufficiently large Reynolds numbers and relatively small Weber numbers where the shape deformation is only moderate, and violent, chaotic fluctuations of shape with a nearly rectilinear path for more highly deformed,

saucer-like bubbles at higher Weber number. The latter phenomenon has been tentatively associated with the nonexistence of steady, axisymmetric flattened shapes beyond a certain critical Weber number (see section 5(b) above). It was, in fact, suggested many years ago by Haberman and Morton (1953) that the origin of the zigzag or helical path was a consequence of vortex shedding from the bubble. However, this explanation was not readily accepted because it presumed the existence of a standing vortex structure, and because lateral motions of similar magnitude had not been observed for rigid spheres even though rigid spheres and spherical bubbles should exhibit similar hydrodynamic resistance to lateral translational accelerations due to the added mass effect (Saffman, 1956). Later experiments with extremely light solid spheres by Preukschat (1962) and MacCready and Jex (1964) did, however, show large scale oscillations of path similar character to those observed for bubbles, thus lending support for Haberman and Morton's (1953) hypothesis. Nevertheless, the fundamental question remains as to why heavy and light bodies in a given fluid should exhibit large differences in the amplitude of path oscillations when the effective mass (i.e. actual + added mass) differs by only an O(1) numerical factor. We believe that the reason lies in the large differences in *moment* of inertia which, for spheres, is directly proportional to the particle density (the added moment of inertia for a sphere is zero). The lateral force associated with vortex shedding is a consequence of the periodic Magnus force arising from interaction of the main flow past the sphere and the circulation around it (the latter being induced each time an amount of vorticity is shed and being of opposite sign to this vorticity). The moment of inertia is important because the induced circulation around the sphere will be strongly damped by viscous effects unless the sphere participates readily in the rotation. This will be true of a bubble or a "hollow" sphere, but not for a solid sphere, since the moment of inertia for a sphere is proportional to its density.

Now, for vortex shedding to occur, two obvious conditions should be met: the standing eddy should exist behind the body, and the Reynolds number should exceed the

critical value R_c at which the motion in the wake becomes unstable. In the case of a rigid bluff body, the standing eddy structure always appears at Reynolds numbers below R_c, which is of 0(200) (see e.g., Nakamura, 1976, for spheres; and Willmarth, Hawk and Harvey, 1964, for disks). For bubbles, on the other hand, our solutions show that separation is not found for any Reynolds number ($\leq$ 200) when the shape is spherical or near-spherical. Thus, in spite of the fact that a Reynolds number may be reached at which vortex shedding would occur if a vortex structure existed, our solutions suggest that there will be little or no departure from a rectilinear path until a sufficiently large W is reached to obtain the necessary downstream eddy structure.

These implications of the present solutions appear to provide a basis for understanding the experimental results of Hartunian and Sears (1957) who found two distinct criteria for the change from a rectilinear to zigzag or helical path:

a. A critical Reynolds number, R $\approx$ 200, for impure liquids.

b. A critical Weber number, W $\approx$ 3.2, for pure liquids.

Apparently, in the impure liquids, the conditions on the surface of the bubble are sufficiently close to no-slip that the vortex ring forms even for bubble shapes close to spherical when the Reynolds number is below R_c, and the usual criterion for onset of vortex shedding from a solid is obtained. In pure liquids, on the other hand, the free surface conditions are relevant and the condition for onset of zigzag for any sufficiently large Reynolds number is the existence of a sufficiently large Weber number to allow formation of the downstream eddy structure. Our numerical solutions show that the Weber number required for existence of separation is somewhat dependent upon the Reynolds number, but decreases to a value of 0(3-4) for R = 200. This is close to the value reported for onset of zigzag in clean fluids by Hartunian and Sears (1957). At lower Reynolds numbers, it is unlikely that the wake structure becomes unstable (based on the necessary critical R for spheres and disks cited earlier), though instability of shape may be expected for R $\sim$ 0(50-100) where the flattened branch of steady

solution suggests a critical Weber number for nonexistence of steady, axisymmetric shapes. We may also note that the existence of a perfectly pure interface is difficult to achieve (especially for water) in an experiment, and any small departure to a slightly contaminated surface will tend to lead to separation at lower W than predicted here for the perfectly clean, zero shear-stress interface. This may account for the fact that the Hartunian and Sears (1957) critical Weber number was only 3.2, while the present numerical results at R = 200 would suggest the need for W = 0(5-6) in order to have not only onset of separation but some development of the standing vortex structure behind the bubble. It may be noted, in support of this contention, that Tsuge and Hibino (1977) report higher critical Weber numbers for onset of zigzag motions, up to 0(5), for bubbles in highly purified organic liquids.

This work was supported by a grant from the Fluid Mechanics Program of the National Science Foundation.

Table 1. Drag coefficients computed by integration of the forces at the surface (above) and the relative deviation from these values of the drag coefficients computed via energy dissipation (below).

R\W	0	2	3	4	5	6	8	10	12	14	15	16	18	20
1	17.5	18.9		19.1		19.1	19.2							
	0%	3%		0.5%		0,5%	1%							
2	9.32	10.6		11.0		11.0	11.1	11.1	11.2	11.2		11.3	11.3	
	0.1%	2%		2%		2%	3%	3%	4%	5%		6%	6%	
5	4.26	5.00		5.48		5.75	5.90	5.99	6.06					
	0%	0.2%		0.5%		2%	3%	4%	5%					
10	2.43	2.92		3.41		3.67	4.00	4.16	4.25	4.33				
	0%	0%		0.5%		2%	3%	6%	8%	10%				
20	1.41	1.74		2.16		2.56	2.94	3.22	3.33		3.55			3.60
	0%	0.5%		1%		2%	5%	10%	10%		5%			4%
50	0.67	0.88		1.23		1.64	2.18	2.77						
	1%	0.5%		0%		5%	12%	18%						
100	0.38	0.54	0.62	0.81	1.02	1.23	1.86	2.26						
	2%	0.5%	6%	1%	4%	7%	27%	26%						
200	0.22	0.33	0.43	0.59	0.79	0.95	1.26	1.64						
	5%	9%	6%	1%	2%	3%	40%	44%						

Table 2. Comparison of the present results for the drag coefficient at low R and W.with the asymptotic theory of Taylor and Acrivos (1964).

	Present Results	Taylor & Acrivos (1964)
R = 0.5, W = 0	33.6	33.7
R = 0.5, W = 0.5	34.7	33.8
R = 0.5, W = 1	35.3	33.9

References

Batchelor, G. K. 1967 An Introduction to Fluid Dynamics. Cambridge University Press.

Bhaga, D. and Weber, M. E. 1981 Bubbles in Viscous Liquids: Shapes, Wakes and Velocities. J. Fluid Mech. **105**, 61-85.

Brabston, D. C. and Keller, H. B. 1975 Viscous Flows Past Spherical Gas Bubbles. J. Fluid Mech. **69**, 179-189.

Davies, R. M. and Taylor, G. I. 1950 The Mechanics of Large Bubbles Rising Through Extended Liquids and Through Liquids in Tubes. Proc. Roy. Soc. A **200**, 375-590.

Fornberg, B. 1980 A Numerical Study of Steady Viscous Flow Past a Circular Cylinder. J. Fluid Mech. **98**, 819-855.

Haberman, W. L. and Morton, R. K. 1953 An Experimental Investigation of the Drag and Shape of Air Bubbles Rising in Various Liquids. David Taylor Model Basin Report 802.

Hartunian, R. A. and Sears, W. R. 1957 On the Instability of Small Gas Bubbles Moving Uniformly in Various Liquids. J. Fluid Mech. **3**, 27-47.

Hnat, J. G. and Buckmaster, J. D. 1976 Spherical Cap Bubbles and Skirt Formation. Phys. Fluids **19**, 182-194.

Lane, W. R. and Green, H. L. 1956 The Mechanics of Drops and Bubbles. In: Surveys in Mechanics (Batchelor, G. K. and Davies, R. M., eds.), pp. 162-215, Cambridge University Press.

Leal, L. G. and Acrivos, A. 1969 The Effect of Base Bleed on the Steady Separated Flow Past Bluff Objects. J. Fluid Mech. **39**, 735-752.

MacCready, P. B. and Jex, H.R. 1964 Study of Sphere Motion and Balloon Wind Sensors. NASA TM X-53089.

Miksis, M., Vanden-Broeck, J.-M. and Keller, J. B. 1981 Axisymmetric Bubble or Drop in a Uniform Flow. J. Fluid Mech. **108**, 89-100.

Moore, D. W. 1959 The Rise of a Gas Bubble in a Viscous Liquid. J. Fluid Mech. **6**, 113-130.

Nakamura, I. 1976 Steady Wake Behind a Sphere. Phys. Fluids **19**, 5-8.

Preukschat, A. W. 1962 Measurements of drag coefficients for falling and rising spheres in free motion. M.S. Thesis, Department of Aeronautical Engineering, California Institute of Technology.

Rivkind, V. Y. and Ryskin, G. 1976 Flow Structure in Motion of a Spherical Drop in a Fluid Medium at Intermediate Reynolds Numbers. Fluid Dyn. **11**, 5-12.

Ryskin, G. 1980 The Extensional Viscosity of a Dilute Suspension of Spherical Particles at Intermediate Microscale Reynolds Numbers. J. Fluid Mech. **99**, 513-529.

Ryskin, G. and Leal, L. G. 1983 Orthogonal Mapping. J. Comput. Phys. (in press).

Ryskin, G. and Leal, L. G. 1983 Large Deformations of a Bubble in Axisymmetric Steady Flows. Part 1. Numerical Technique. J. Fluid Mech. (submitted).

Saffman, P. G. 1956 On the Rise of Small Air Bubbles in Water. J. Fluid Mech. **1**, 249-275.

Saffman, P. G. 1981 Dynamics of Vorticity. J. Fluid Mech. **106**, 49-58.

Sokolnikoff, I. S. 1964 Tensor Analysis. Wiley.

Taylor, T. D. and Acrivos, A. 1964 On the Deformation and Drag of a Falling Viscous Drop at Low Reynolds Number. J. Fluid Mech. **18**, 466-476.

Tsuge, H. and Hibino, S. I. 1977 Onset conditions of oscillatory motion of single gas-bubbles rising in various liquids. J. Chem. Eng. Japan **10**, 66-68.

Wegener, P. P. and Parlange, J.-Y. 1973 Spherical-Cap Bubbles. Ann. Rev. Fluid Mech. **5**, 79-100.

Willmarth, W. W., Hawk, N. E. and Harvey, R. L. 1964 Steady and Unsteady Motions and Wakes of Freely Falling Disks. Phys. Fluids **7**, 197-208.

Figure Captions

Figure 1. The boundary-fitted coordinate system.

Figure 2. Comparison of the solution for R = 20, W = 12 with the 40x40 grid (left) and the finer 80x80 grid (right). Here and elsewhere in this paper, the contour values for the stream-function are 0, ± 0.001, ± 0.002, ± 0.005, ± 0.01, etc.; for vorticity 0, ± 0.01, ± 0.02, ± 0.05, ± 0.1, etc.

Figure 3. Drag coefficients for a steadily rising bubble as a function of the Weber number for various values of the Reynolds number. The arrows indicate the empirical correlation of Bhaga and Weber (1981) for very large W; W = 0 corresponds to spherical bubbles.

Figure 4. Computed steady, axisymmetric shapes of rising bubbles as a function of R and W.

Figure 5. Comparison of the present results for bubble shape (solid line) with the asymptotic solution of Taylor and Acrivos (1964) (broken line).

Figure 6. Surface distributions of pressure and viscous normal stress as functions of the (relative) distance from the front stagnation point. (1) the hydrostatic pressure $-p_{hs}$; (2) the dynamic pressure $-p_{dyn}$; (3) viscous normal stress $\frac{8}{R}e_{\xi\xi}$; (4) total normal stress $\tau_{\xi\xi}$, i.e. the sum of (1), (2) and (3) according to Eq. (10).

Figure 7. Flow separation at a free surface: the standing eddy structure behind the bubble.

Figure 8. Comparison of the experimental photograph by Hnat and Buckmaster (1976) for R = 19.4, W = 15.3 (C_D = 3.44) with present results for R = 20, W = 15 (C_D = 3.55).

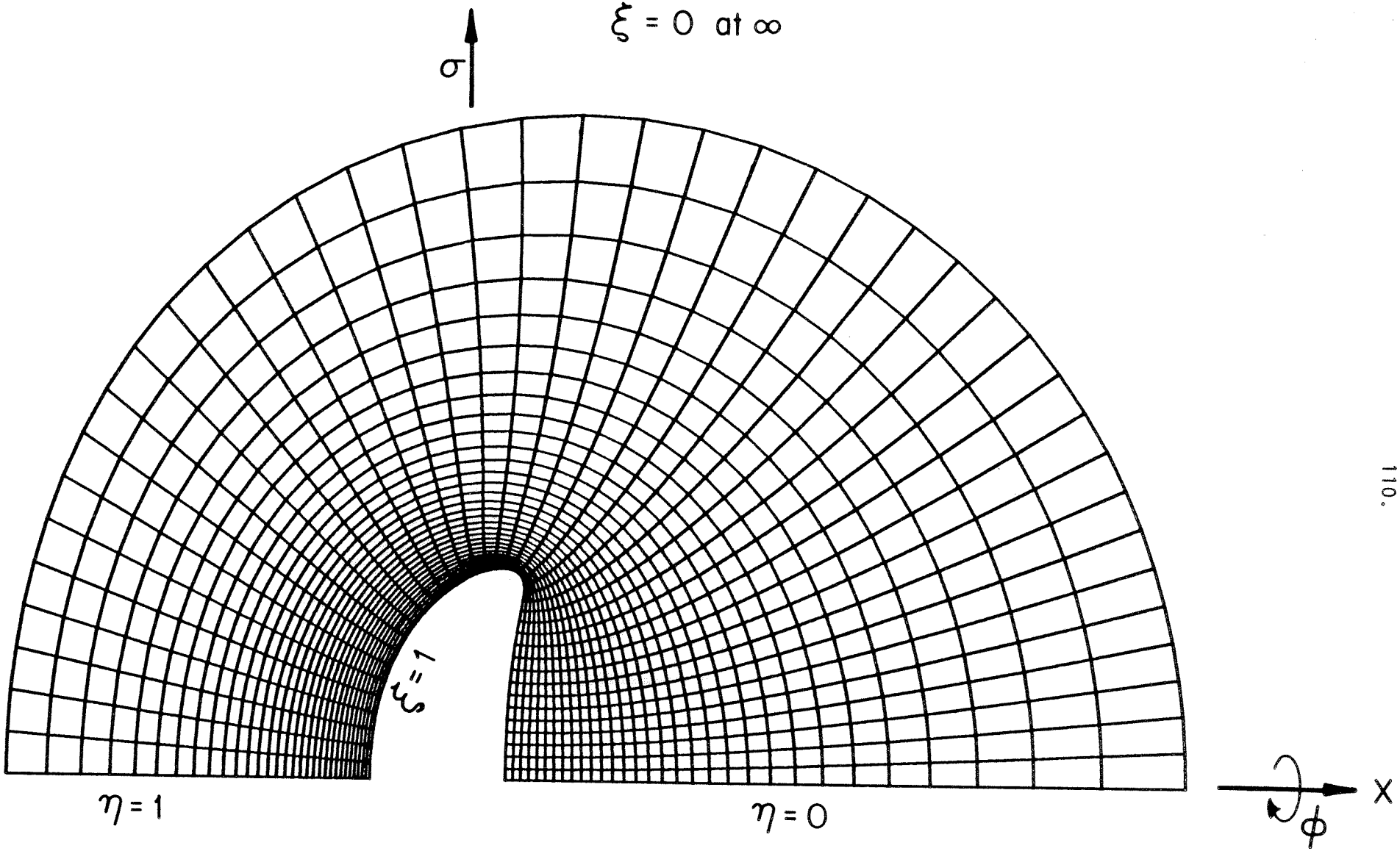

Figure 1

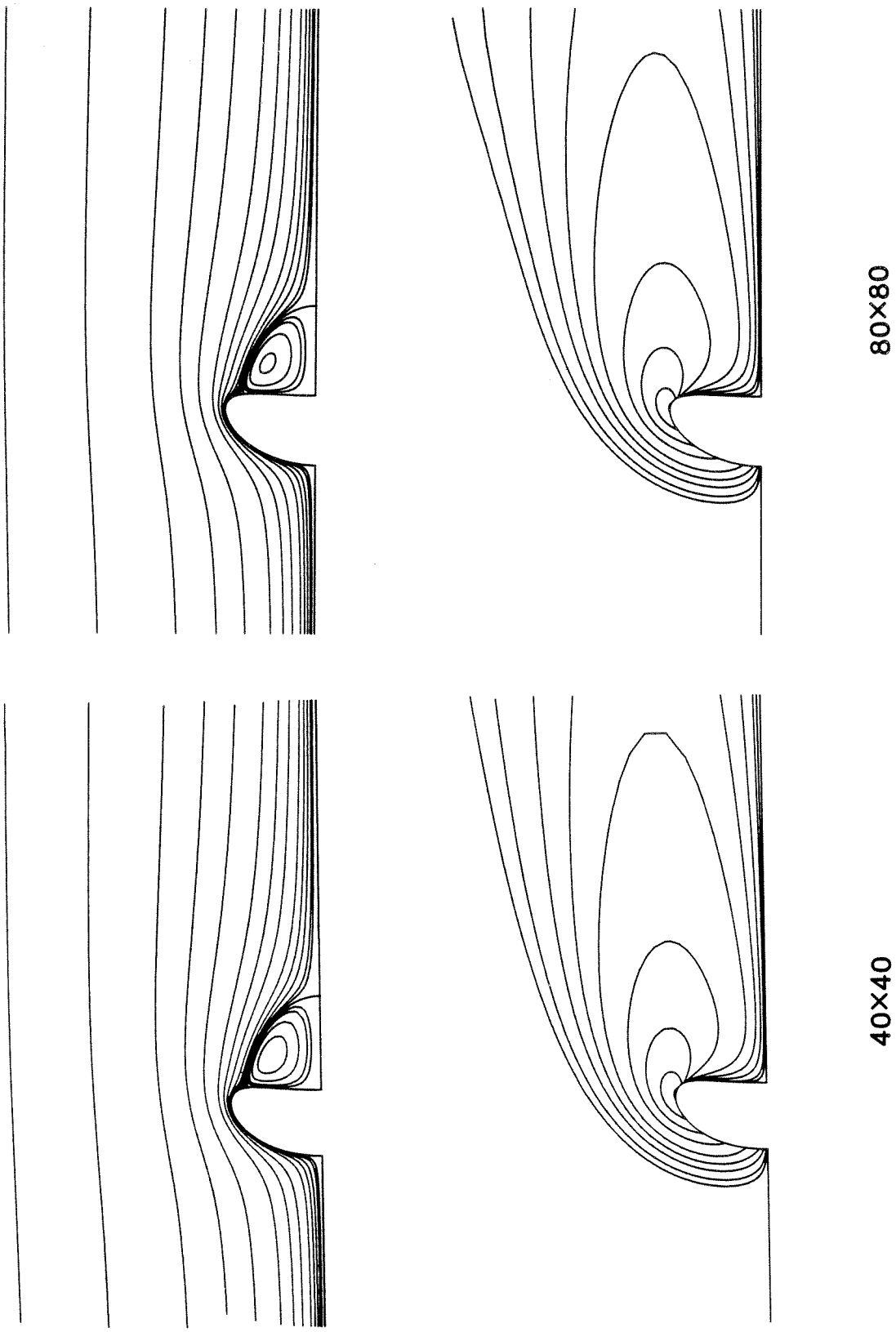

Figure 2

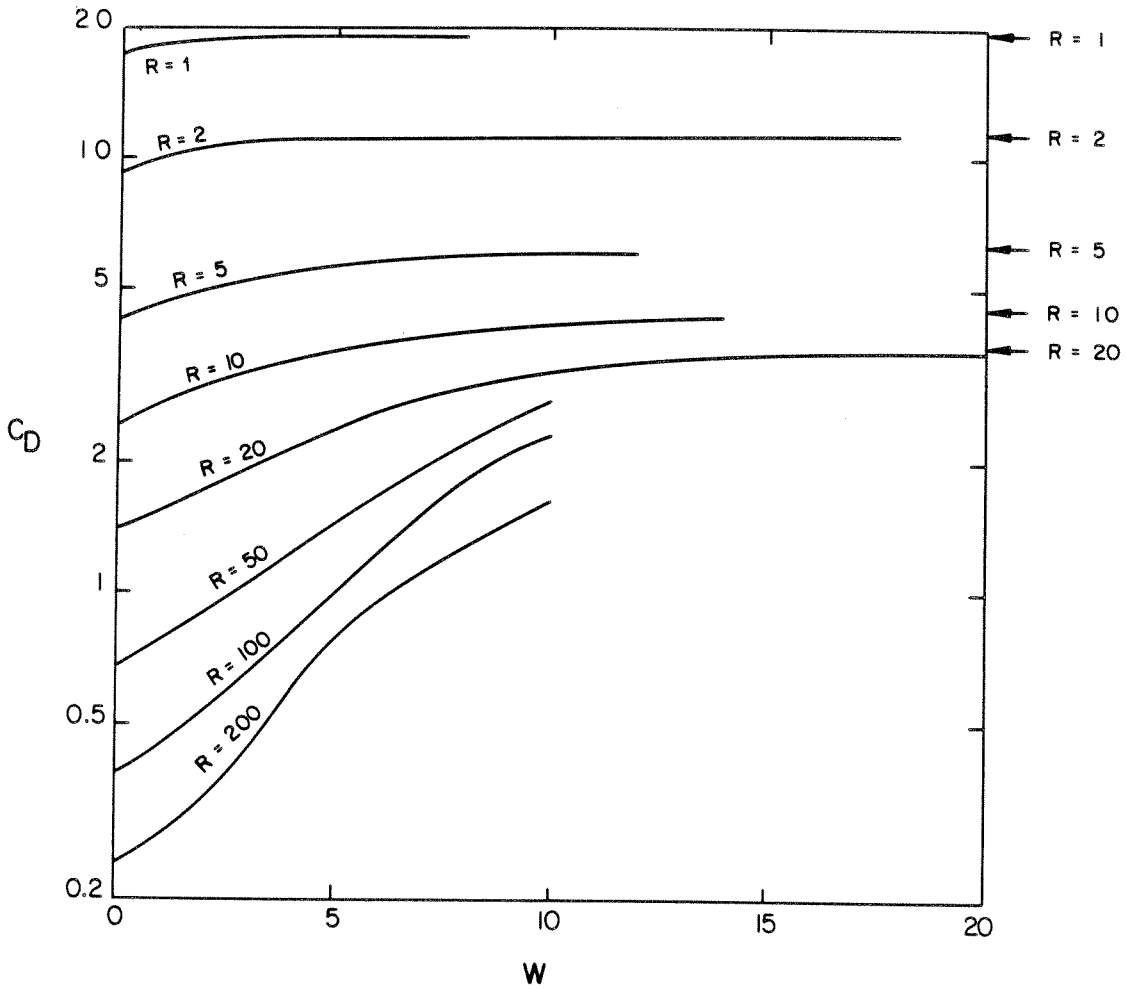
20
10
5
2
1
0.5
0.2
C_D
R = 1
R = 2
R = 5
R = 10
R = 20
R = 50
R = 100
R = 200
R = 1
R = 2
R = 5
R = 10
R = 20
0
5
10
15
20
W

Figure 3

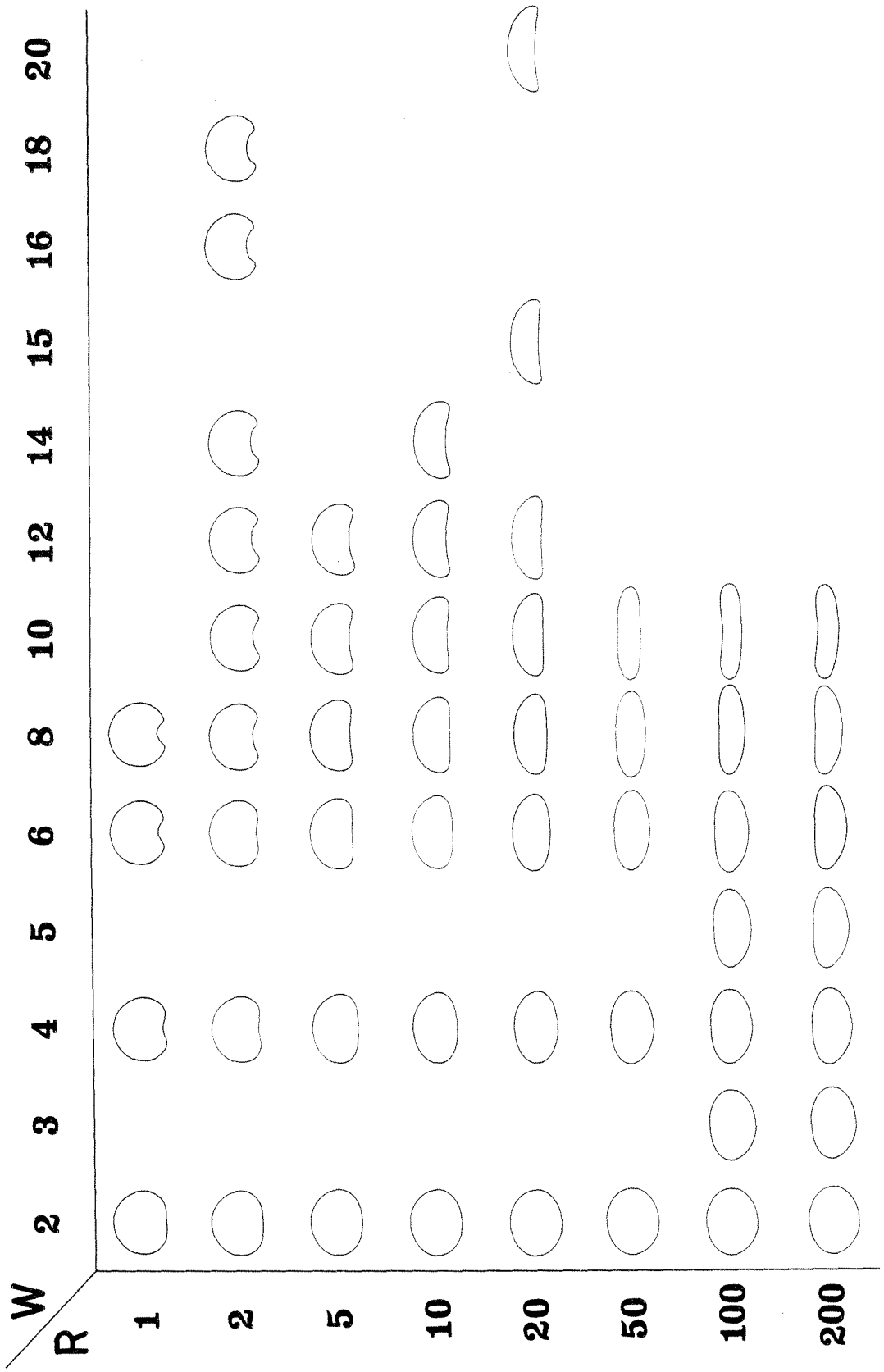

Figure 4

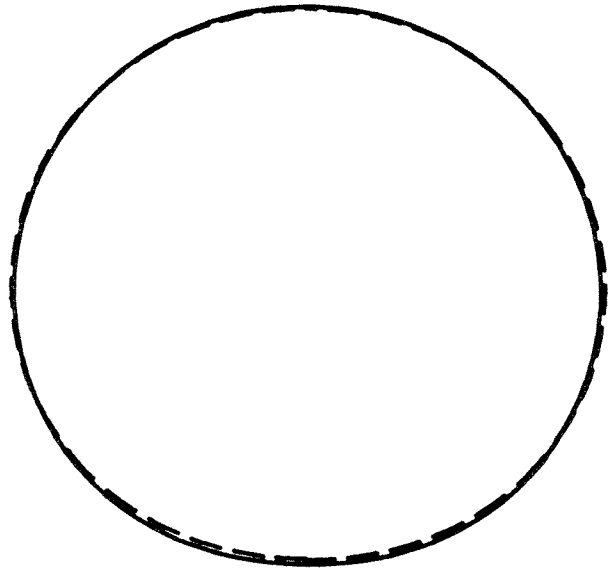

R = 0.5, W = 0.5

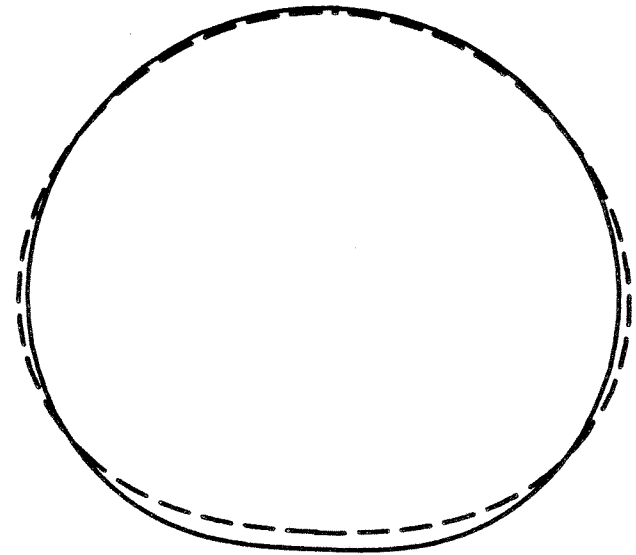

R = 0.5, W =1

Figure 5

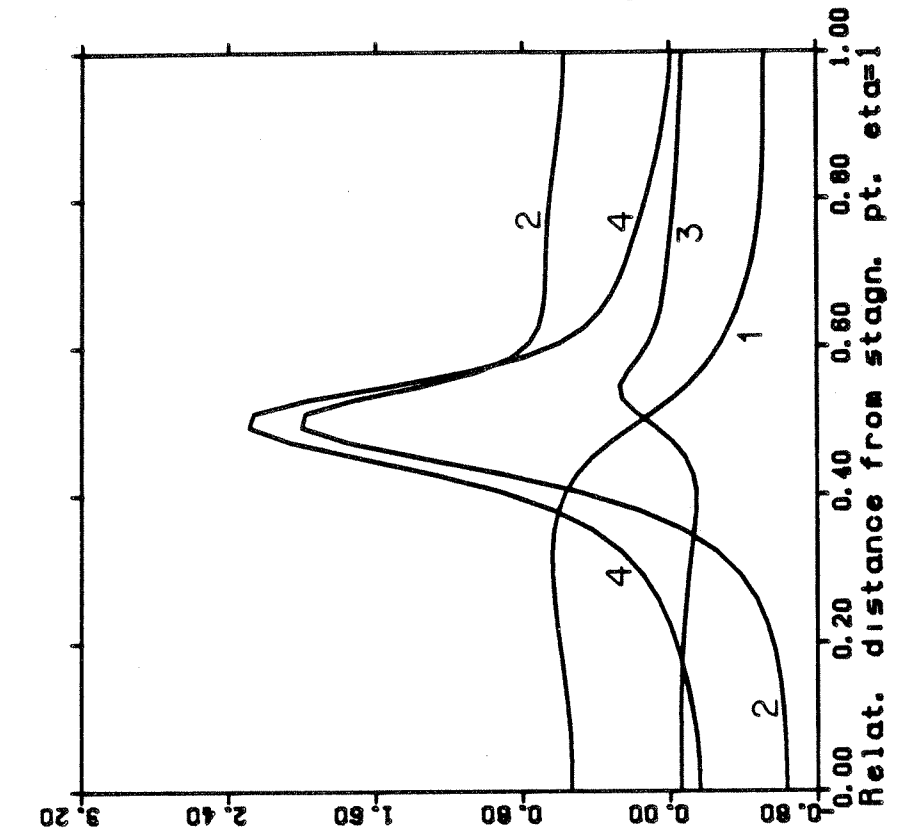

R=100, W=10

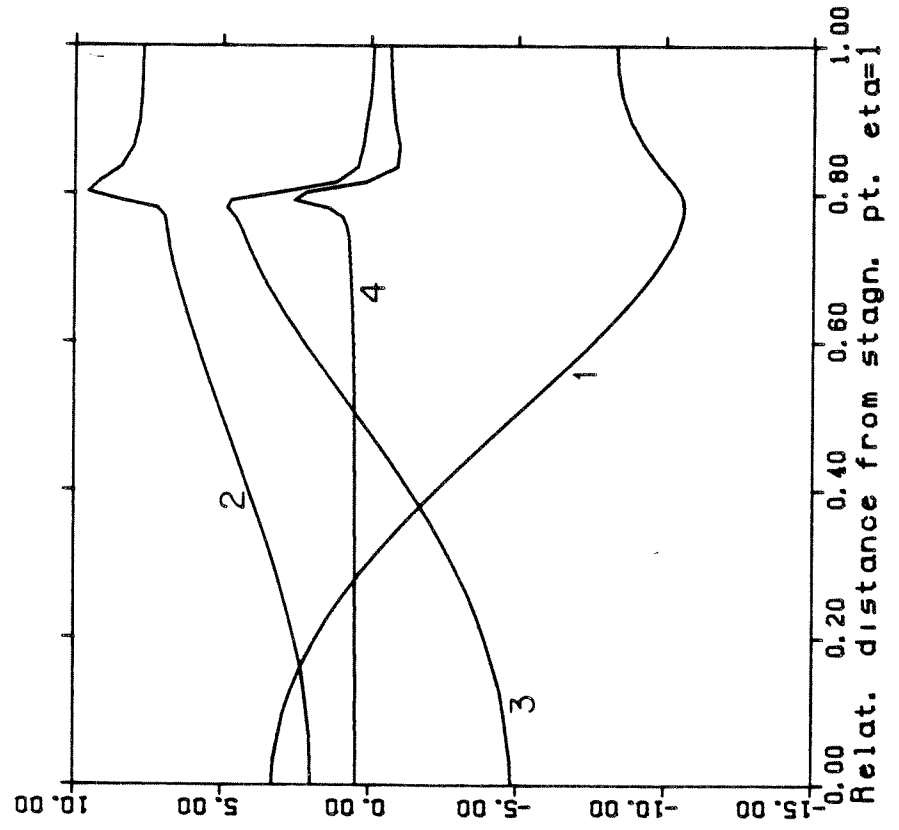

R=2, W=16

Figure 6

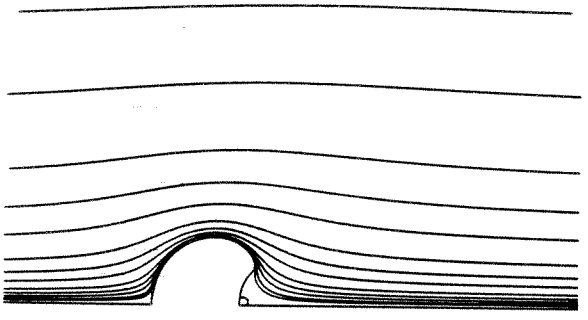

R=2, W=12

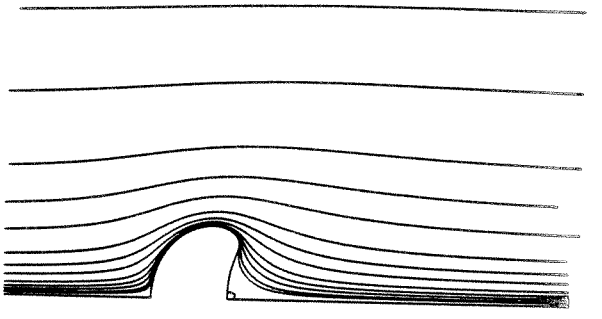

R=5, W=12

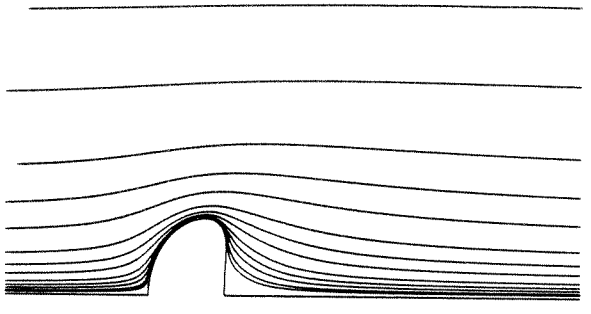

R=10, W=8

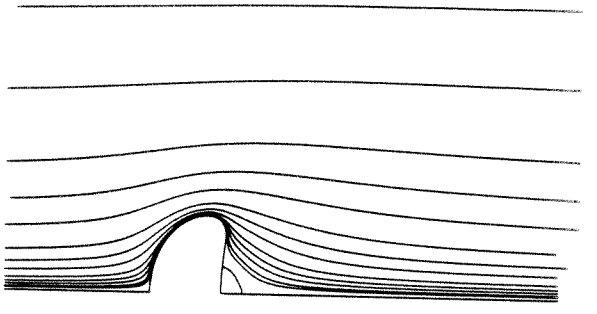

R=10, W=10

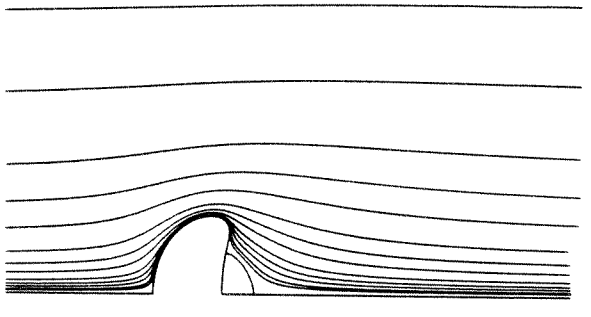

R=10, W=12

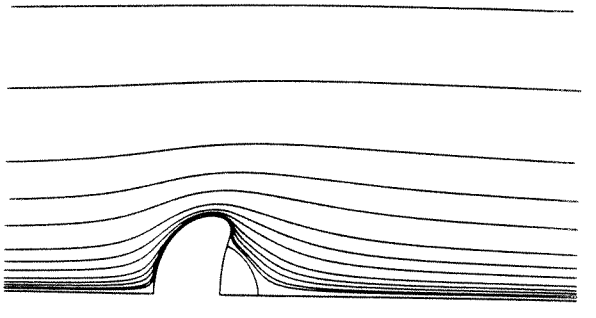

R=10, W=14

Figure 7

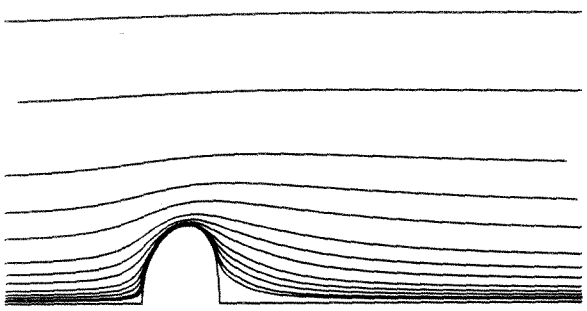

R-20, W-6

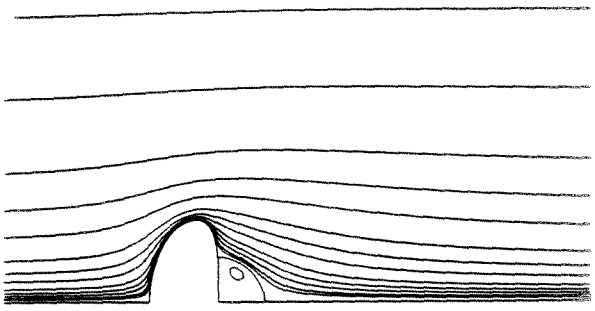

R-20, W-8

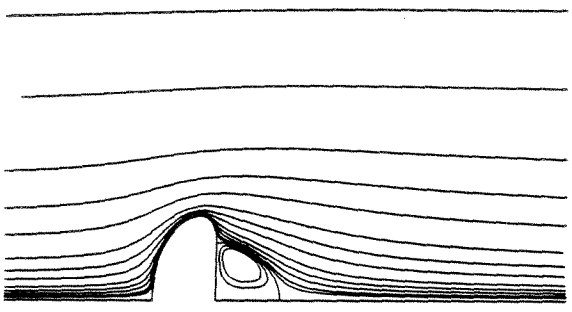

R-20, W-10

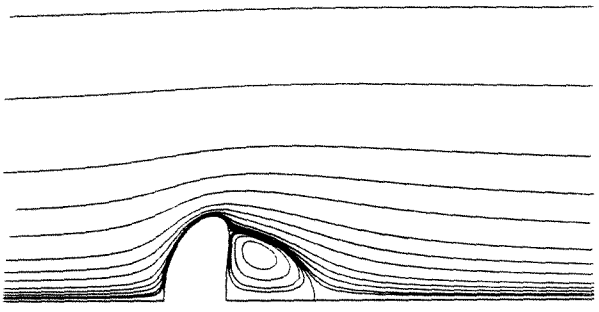

R-20, W-12

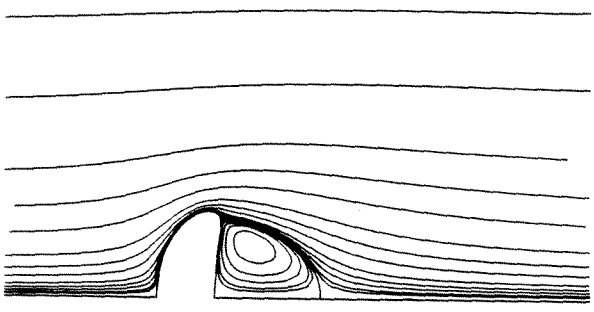

R-20, W-15

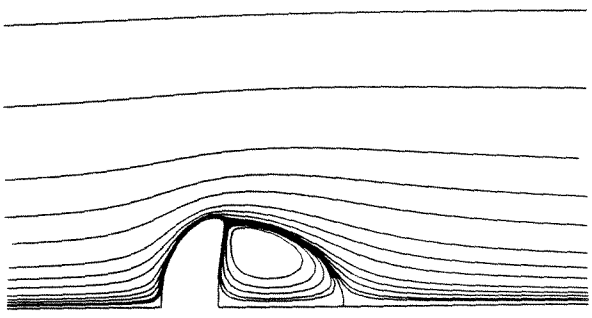

R-20, W-20

Fig. 7 cont'd

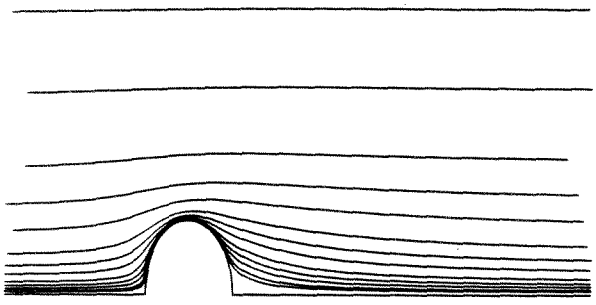

R-50, W-4

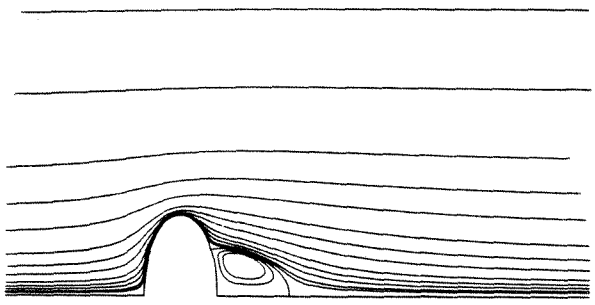

R-50, W-6

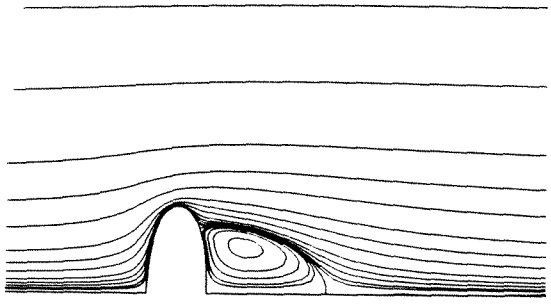

R-50, W-8

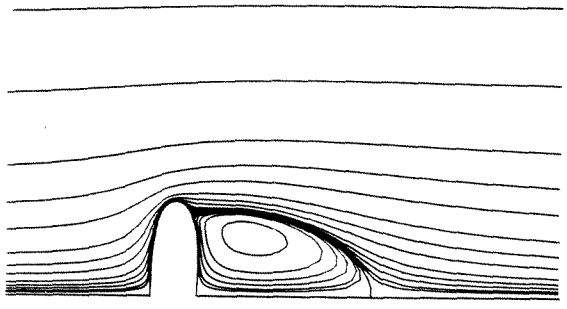

R-50, W-10

Fig. 7 cont'd

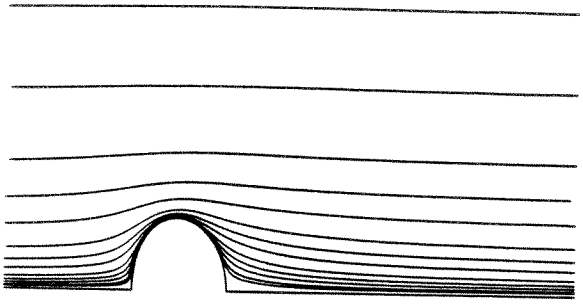

R=100, W=3

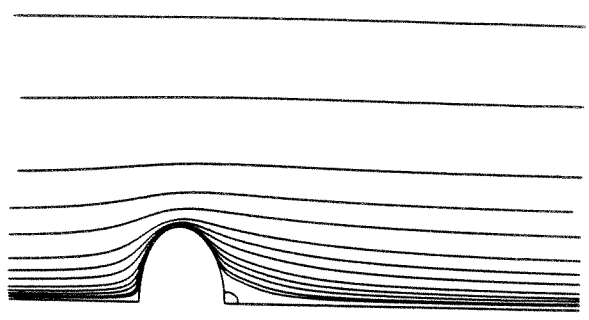

R=100, W=4

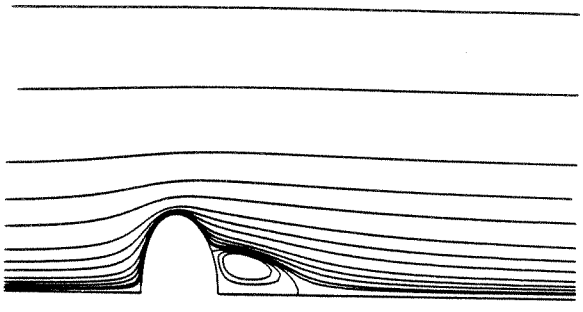

R=100, W=5

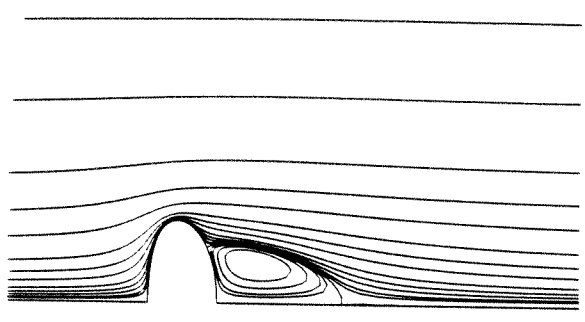

R=100, W=6

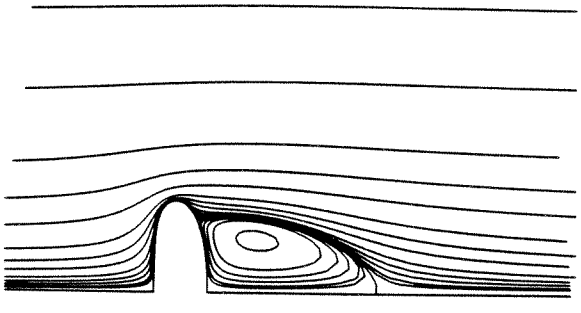

R=100, W=8

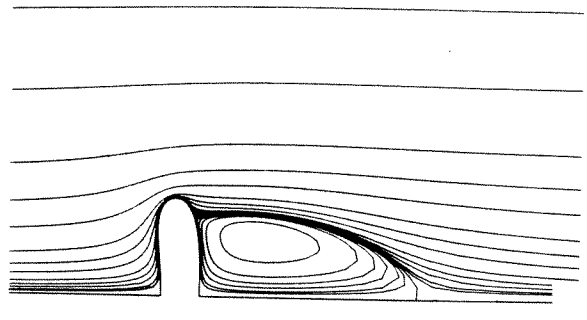

R=100, W=10

Fig. 7 cont'd

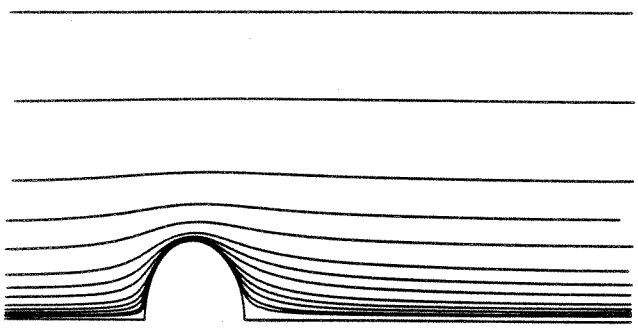

R=200, W=3

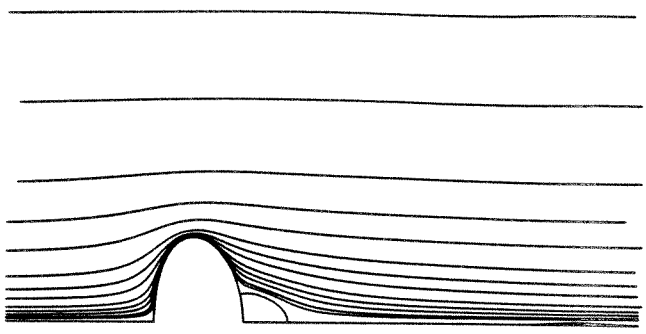

R=200, W=4

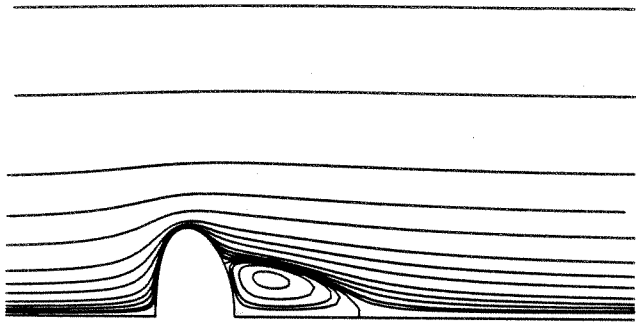

R=200, W=5

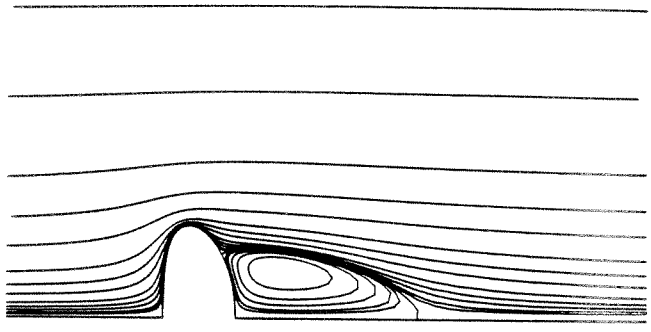

R=200, W=6

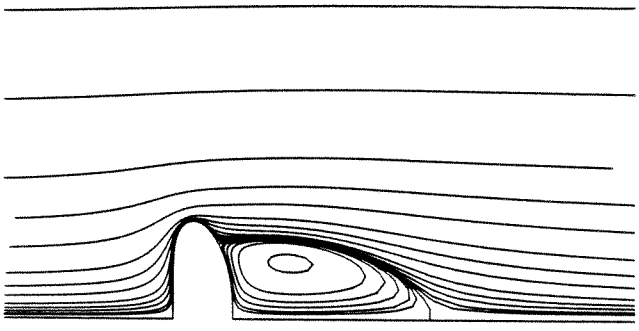

R=200, W=8

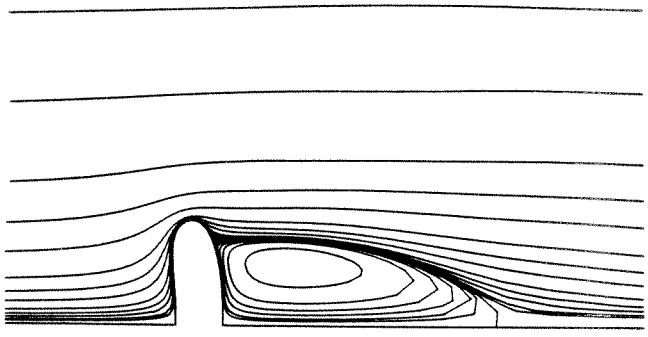

R=200, W=10

Fig. 7 cont'd

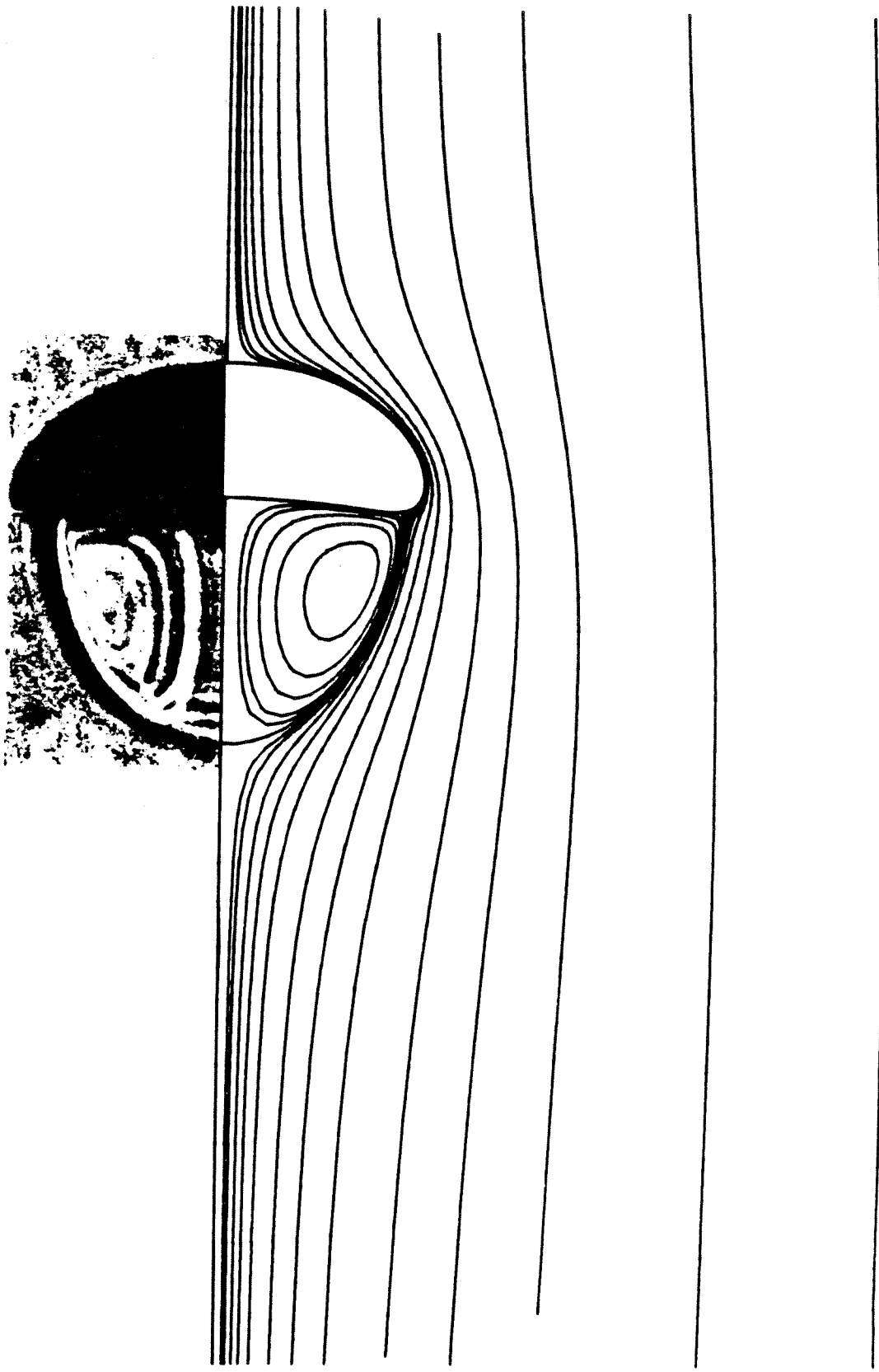

Figure 8

CHAPTER IV

Large Deformations of a Bubble in Axisymmetric Steady Flows. Part 3. Uniaxial Extensional Flow

by

G. Ryskin and L. G. Leal
Department of Chemical Engineering
California Institute of Technology
Pasadena, CA 91125

Abstract

We consider the deformation of a bubble in a uniaxial extensional flow for Reynolds numbers in the range $0.1 \leq R \leq 100$. The computations show that the bubble bursts at a relatively early stage of deformation for $R \geq 0(10)$, never reaching the highly elongated shapes observed and predicted at low Reynolds numbers. We also compute the deformation of the bubble under the assumption of potential flow and conclude that the potential flow solution provides a good approximation to the real flow in this case for $R \geq 0(100)$.

J. Fluid Mech. (submitted)

1. Introduction

The present paper is the third in a series (see Ryskin and Leal, 1983b,c) in which we use numerical methods to study the deformation of a bubble in axisymmetric flow fields at finite Reynolds number. Here we consider uniaxial extensional flow. Previous theoretical studies of this problem have been restricted to zero Reynolds number flows (Taylor, 1934, 1964; Buckmaster, 1972; Barthes-Biesel and Acrivos, 1973; Youngren and Acrivos, 1976), with the exception of the nonzero Reynolds number, slender-body analysis of Acrivos and Lo (1978) which extends to Reynolds number of O(0.1). Although laboratory studies have generally been restricted to highly viscous fluids (and to two-dimensional, rather than uniaxial, extension), many practical flows involve low viscosity fluids such as water and the Reynolds numbers in these systems easily attain values $O(10^2-10^3)$. For example, to achieve R = 100 in water with a bubble of 1 cm diameter requires a strain rate of only $O(1\ sec^{-1})$. The present study covers R ranging from 0.1 to 100, as well as potential flow results, in all of which the deformation may become quite large.

At low Reynolds number, both experiments and theory (Taylor, 1964) show that a bubble may become extremely elongated and develop pointed ends where the curvature tends locally to extremely large values. Such cases are not accessible with our present numerical technique, and the slender-body analysis of Taylor (1964), Buckmaster (1972) and Acrivos and Lo (1978) cannot be checked now. However, we can compare our results in the low Reynolds number range, R = 0.1 and 1, with the predictions of Youngren and Acrivos (1976) who used the boundary-integral technique for creeping flow to consider large deformations of a bubble in extensional flow at zero Reynolds number.

Our results for intermediate Reynolds numbers, R = 10 and 100 appear to us to be of greater interest. Assuming that the absence of numerical convergence can be taken to signify the nonexistence of a stable, axisymmetric solution (which is certainly not

always true, but appears likely in this case), our results indicate that the presence of inertia leads to breakup of a bubble at a quite early stage of deformation.

2. Statement of the Problem

We consider an incompressible gas bubble of volume $4/3\ \pi a^3$ subjected to a steady uniaxial extensional flow of a fluid with constant density ρ and constant viscosity μ. The density and viscosity of the gas inside the bubble are assumed negligible in comparison with those of the liquid. Furthermore, the surface of the bubble is assumed to be characterized completely by a uniform surface tension γ. Finally, we neglect all effects of gravity including the hydrostatic pressure variation in the fluid. The latter condition has been adopted in all previous studies of the problem, and is necessary in order that the shape be axisymmetric and exhibit fore-aft symmetry. If the x-axis of cylindrical coordinates x,σ,φ is directed along the axis of symmetry, the (dimensional) velocity field far from the bubble is given by

$$\underline{u} = \underline{\underline{E}}\cdot\underline{r}; \quad \underline{\underline{E}} = E\begin{bmatrix} 1 & 0 & 0 \\ 0 & -1/2 & 0 \\ 0 & 0 & -1/2 \end{bmatrix}; \quad E>0$$

where E is the principal strain rate. We use the equivalent radius of the bubble a as a characteristic length scale and the product Ea as a characteristic velocity scale. The numerical solution is computed on a boundary-fitted, curvilinear orthogonal coordinate system ξ,η,φ obtained by the technique of orthogonal mapping (Ryskin and Leal, 1983a), in such a way that the surface of the bubble is always represented by the coordinate surface $\xi = 1$. The derivation of the appropriate form of the Navier-Stokes equations proceeds exactly as in Part 2. Thus, as before, we obtain

$$L^2(\omega\sigma) - \frac{R}{2}\frac{1}{h_\xi h_\eta}\left\{\frac{\partial\psi}{\partial\xi}\frac{\partial}{\partial\eta}\left[\frac{\omega}{\sigma}\right] - \frac{\partial\psi}{\partial\eta}\frac{\partial}{\partial\xi}\left[\frac{\omega}{\sigma}\right]\right\} = 0 \tag{1}$$

$$L^2\psi + \omega = 0 \tag{2}$$

where

$$L^2 \equiv \frac{1}{h_\xi h_\eta}\left\{\frac{\partial}{\partial\xi}\left[\frac{f}{\sigma}\frac{\partial}{\partial\xi}\right]+\frac{\partial}{\partial\eta}\left[\frac{1}{f\sigma}\frac{\partial}{\partial\eta}\right]\right\}$$

Here ψ is the Stokes stream function, ω is the vorticity and $R \equiv 2\rho(Ea)a/\mu$ the Reynolds number based on the equivalent diameter of the bubble 2a.

The scale factors h_ξ, h_η are obtained from the mapping functions $x(\xi,\eta), \sigma(\xi,\eta)$ — see Part 1. The distortion function $f \equiv h_\eta / h_\xi$ is specified in advance as $f = \frac{\pi}{2}\xi$.

Due to the obvious symmetry with respect to the equatorial plane, we need to consider only half of the φ = const plane, i.e. $x \geq 0$, $\sigma \geq 0$ (see Fig. 1). The boundary conditions are thus:

$$\psi = 0\,, \quad \omega = 0 \begin{cases} \text{on the axis of symmetry, } \eta = 0 \\ \text{and} \\ \text{on the plane of symmetry, } \eta = 1 \end{cases} \tag{3}$$

$$\psi \sim \frac{1}{2}x\sigma^2; \quad \omega \to 0 \text{ at } \infty\ (\xi \to 0) \tag{4}$$

plus conditions at the surface of the bubble $\xi = 1$. These are the kinematic condition

$$\psi = 0 \text{ at } \xi = 1\,, \tag{5}$$

the condition of vanishing tangential stress

$$\omega - 2\kappa_{(\eta)}u_\eta = 0 \tag{6}$$

where $\kappa_{(\eta)}$ is the normal curvature of the surface in the η-direction, and the balance between normal stress and forces due to surface tension

$$\tau_{\xi\xi} - \frac{4}{W}\left(\kappa_{(\eta)} + \kappa_{(\varphi)}\right) = 0 \tag{7}$$

where $\kappa_{(\varphi)}$ is the normal curvature of the surface in φ-direction and $W \equiv 2\rho(Ea)^2a/\gamma$ is the Weber number.

Expressions for the normal curvatures in terms of $x(\xi,\eta)$ and $\sigma(\xi,\eta)$ are given in Part 2. The normal stress $\tau_{\xi\xi}$ can also be taken directly from Part 2, with the only change being that hydrostatic pressure variations are neglected in the present

problem, i.e.

$$\tau_{\xi\xi} = -p_{dyn} + \frac{8}{R} e_{\xi\xi} \tag{8}$$

where

$$p_{dyn} = -u_\eta^2 - \frac{4}{R} \int \frac{f}{\sigma} \frac{\partial}{\partial \xi} (\sigma\omega) d\eta \tag{9a}$$

and

$$e_{\xi\xi} = -\frac{1}{\sigma h_\eta} \frac{\partial}{\partial \eta} (\sigma u_\eta) . \tag{9b}$$

This essentially completes the statement of the problem. The method of solution has been described in Parts 1 and 2. We used a 40x40 grid in the ξ,η coordinates; each solution took 15 to 45 min of CPU time on the VAX-11/780 computer that was used in the present work.

3. Numerical Results and Discussion

We have done computations for R = 0.1, 1, 10, 100, gradually increasing W in each case until a value of W was reached at which either a converged solution could not be obtained or became excessively expensive.

The computed shapes are shown in Fig. 2. At low Reynolds numbers there is an apparent trend, predicted by the creeping flow theory and observed in experiments (see Acrivos and Lo, 1978, and references therein) for a bubble to elongate monotonically with increase in the capillary number $\mu Ea/\gamma = W/R$. In the process of this elongation, the curvature of the surface becomes very large at the tips of the bubble. As noted in the preceding Parts I and II, our numerical method in its present form is not well-suited to the treatment of bubble shapes with locally very large curvature. Accordingly, when convergence either cannot be achieved or becomes excessively slow in cases with very large curvature somewhere on the surface, this fact does not necessarily signify the nonexistence of steady axisymmetric solutions for bubble shape.

Indeed, the slender-body theory at R = 0 due to Taylor (1964), Buckmaster (1972) and Acrivos and Lo (1978) predicts no breakup and is in good agreement with experiment. This slender-body regime (which requires $\mu Ea/\gamma >> 0.23$, see Hinch and Acrivos, 1979, p. 405) is beyond the scope of the present study.

Our results at R = 0.1 are in good agreement with the creeping flow solution of Youngren and Acrivos (1976), which was obtained using the boundary-integral technique (see Fig. 3). It can be seen that our solution predicts a slightly higher deformation for R = 0.1 than Youngren and Acrivos's (1976) for R = 0. A qualitatively similar result was obtained in the slender-body analysis for a bubble by Acrivos and Lo (1978) which predicts no breakup at R = 0, but greater deformation and breakup for $R \neq 0$. At R = 1, our results show that the deformation follows the same general "low Reynolds number patttern", with the bubble becoming strongly elongated. It can be seen, for $R \leq 1$ and $\mu Ea/\gamma \leq 0.25$, that the influence of Reynolds number is mainly to increase the magnitude of deformation without a radical change in its character.

A qualitative change in the nature of the deformation does take place at some Reynolds number between 1 and 10. At R = 10 and 100, the bubble does not become elongated. As can be seen from Fig. 2, the bubble first assumes the shape of an oval, but with further increase of W the side surface approaches a circular cylindrical shape. We could not obtain a converged solution for R = 10 and W = 1 and for R = 100 and W = 2.2, even though solutions for the same Reynolds numbers and W less by 0.1 were readily obtained (see Fig. 2). In these cases, there are no surface points where the curvature is much higher than O(1), and so it is unlikely that purely numerical difficulties could be a source of divergence. Monitoring the shape of the bubble during an attempt to compute these diverging solutions, we observed that after some number of iterations the side surface of the bubble became cylindrical at the equator (i.e. $\kappa_{(\eta)}$ became zero there), then a "waist" appeared and divergence followed. Though our numerical procedure in its present form does not simulate a real transient (unsteady) flow, it is intuitively clear from the sequence of shapes for R = 10 and 100 in Fig. 2 that further

increase in Weber number would lead to appearance of the "waist" in a real flow. Again intuition suggests that a bubble with a waist is unlikely to be stable and should burst into two parts (indeed, such is the ease for a slender bubble with a waist at R = 0 as shown by Hinch, 1980).

We do not present the streamline plots corresponding to the shapes in Fig. 2 since there is no flow separation and accordingly the streamlines provide little additional insight. It is quite unlikely that separation will appear at higher Reynolds numbers since the only source of vorticity is boundary curvature which seems to be approaching an O(1) limit as R is increased for any fixed W (see Part II for a discussion of the connection between vorticity production and separation). Also, the velocity and pressure fields in an extensional flow differ from those in the uniform flow in a way which makes flow separation much less likely, e.g. there is no separation in an extensional flow past a solid sphere at Reynolds numbers up to $O(10^3)$ (see Ryskin, 1980, section 7). If separation does not occur, a solution under the assumption of irrotational flow should provide a good approximation to the real flow for $R \to \infty$. Therefore, we have computed such inviscid irrotational solutions by setting the vorticity equal to zero everywhere and neglecting those terms which include a factor 1/R in the expression for normal stress, which thus becomes

$$\tau_{\xi\xi} = - p_{dyn} = u_\eta^2 \ .$$

The problem becomes quite easy in this case and takes only about 5-10 min of CPU time on the VAX-11/780. The results presented in Fig. 2 show that the trend which is already apparent at R = 10 continues to $R \to \infty$. The Weber number W = 2.7 is the highest (in steps of 0.1) for which a converged solution could be obtained in the potential flow limit; for W = 2.8 the "waist" appears at some stage of the iteration process and then keeps contracting without converging to an equilibrium solution.

We thus conclude that bubbles in an extensional flow for $R \geq O(10)$ do not become elongated but burst at W = O(1) after a relatively small deformation. In particular, our

results suggest strongly that bubble breakup or burst will occur at $W \approx 1$ for $R = 10$, at $W \approx 2.2$ for $R = 100$, and at $W \approx 2.8$ as $R \to \infty$.

It should be emphasized that our results are valid only for bubbles (whose density is negligible) but not for inviscid drops. These two cases are identical only if the Reynolds number is zero or if the shape is fixed (spherical). Otherwise, one must take into account the variation of pressure inside the inviscid drop. In particular, if the drop is neutrally buoyant, the u_η^2 term in the expression for the normal stress (9) will be exactly cancelled by a similar term inside the drop. This u_η^2 term is the dominant contribution to the normal stress and thus the shapes of *bubbles* at high R. In particular, the strong deformation at the equator of the bubble for $R > 0(10)$ (and eventually, the development of the "waist" and subsequent bursting of the bubble) is apparently due to the high stagnation pressure at this point. The complete cancellation of the u_η^2 term in the case of a neutrally buoyant (viscous or inviscid) drop is certain to have a profound effect on the deformation. We note in passing that the above remarks are also applicable to Acrivos and Lo's (1978) solution at nonzero Reynolds number in the slender-body regime, which is therefore valid only for a bubble and not for an inviscid drop as suggested by Acrivos and Lo (1978).

4. Comparison with Rising Bubble

In a certain sense, the deformation of a bubble in an extensional flow is a much simpler phenomenon than the deformation of a rising bubble in a quiescent fluid. In particular, the surface values of the hydrostatic and dynamic pressure and the viscous normal stress balance exactly in an integral sense in the case of a rising bubble (see part 2) since the resultant force on the bubble is zero. Thus, deformation in this case is a consequence of local *differences* in stress and pressure distributions, which are extremely difficult to anticipate, balanced against capillary forces. On the other hand, the balance of forces to achieve zero net force in the extensional flow is satisfied due entirely to the fore-aft symmetry of the bubble. Thus, one or the other of the pressure

and normal stress contributions can become dominant over the others, and then deformation occurs as a result of this one distribution balanced against capillary forces. Because of this, the qualitative mode of deformation is much more accessible to intuition in the latter case. For example, the tendency for a bubble in extensional flow at low Reynolds number to extend in the direction of the principal axis of strain is easily anticipated from the viscous stress and pressure distribution at the surface of a spherical bubble in the same flow. Similarly, at high Reynolds number, the dynamic pressure is the dominant contributor to the stress balance at the bubble surface, and it is evident that the bubble should be pushed inward at all stagnation points due to the higher pressure there, as was indeed observed.

The above discussion also clarifies the difference between the two problems in terms of the importance of the dimensionless groups for estimating the degree of deformation. In the most general sense (i.e. not referring to any particular problem), one would expect the degree of deformation at low Reynolds number to depend upon the capillary number W/R, which is a measure of the magnitude of viscous stresses relative to capillary pressure. For example, when $W/R = O(1)$, one should normally expect large scale deformation and possibly even breakup on the basis of the order of magnitude estimate of viscous "deforming" forces relative to the surface tension "restoring" forces which is inherent in W/R. Likewise, the Weber number would be expected to play a similar role at higher R, since it is a measure of the order of magnitude of dynamic pressure forces relative to capillary forces. These expectations are fully borne out in the case of an extensional flow, as can be seen from the results of Fig. 2. However, in the case of a rising bubble, these expectations prove completely wrong. The capillary number does not play any role at all. Furthermore, though the Weber number does determine the deformation at nonzero Reynolds numbers, the deformation is rather small at $W = O(1)$ and, indeed, extremely high Weber numbers can be reached experimentally for spherical-cap bubbles without breakup, the shape of a bubble becoming essentially independent of W above some value of order 15-20 (see part 2). Unlike the

extensional flow problem where W/R and W do provide a direct measure of the strength of the *dominant* deforming forces relative to the restoring tendency of surface tension, the overall "integral" balance between static and dynamic pressures and the viscous normal stress means that no single one of these deforming forces can become dominant at any W/R or W.

This work was supported by a grant from the Fluid Mechanics Program of the National Science Foundation.

References

Acrivos, A. and Lo, T. S. 1978 Deformation and breakup of a single slender drop in an extensional flow. J. Fluid Mech. **86**, 641-672.

Barthes-Biesel, D. and Acrivos, A. 1973 Deformation and burst of a liquid droplet freely suspended in a linear shear field. J. Fluid Mech. **61**, 1-21.

Buckmaster, J. D. 1972 Pointed bubbles in slow viscous flow. J. Fluid Mech. **55**, 385-400.

Hinch, E. J. and Acrivos, A. 1979 Steady long slender droplets in two-dimensional straining motion. J. Fluid Mech. **91**, 401-414.

Hinch, E. J. 1980 The evolution of slender inviscid drops in an axisymmetric straining flow. J. Fluid Mech. **101**, 545-553.

Ryskin, G. 1980 The extensional viscosity of a dilute suspension of spherical particles at intermediate microscale Reynolds numbers. J. Fluid Mech. **99**, 513-529.

Ryskin, G. and Leal, L. G. 1983a Orthogonal mapping. J. Comput. Phys. (in press).

Ryskin, G. and Leal, L. G. 1983b Large deformations of a bubble in axisymmetric steady flows. Part 1. Numerical technique. J. Fluid Mech. (submitted).

Ryskin, G. and Leal, L. G. 1983c Large deformations of a bubble in axisymmetric steady flows. Part 2. The rising bubble. J. Fluid Mech. (submitted).

Taylor, G. I. 1934 The formation of emulsions in definable fields of flow. Proc. Roy. Soc. A **146**, 501-523.

Taylor, G. I. 1964 Conical free surfaces and fluid interfaces. Proc. 11th Int. Cong. Appl. Mech., Munich (H. Gortler, ed.), pp. 790-796.

Youngren, G. K. & Acrivos, A. 1976 On the shape of a gas bubble in a viscous extensional flow. J. Fluid Mech. **76**, 433-442.

Figure Captions

Figure 1. The boundary-fitted coordinate system.

Figure 2. Shapes of a bubble in uniaxial extensional flow as a function of Reynolds and Weber numbers; $R = \infty$ corresponds to the potential flow solution.

Figure 3. Comparison of the present results for $R = 0.1$ (points) with the results of Youngren and Acrivos (1976) for $R = 0$ (solid line), plotted in terms of the deformation parameter $D \equiv (l - b)/(l + b)$ as a function of the capillary number $\mu Ea/\gamma$. Here l and b are, respectively, lengths of the major and minor axes of the bubble profile.

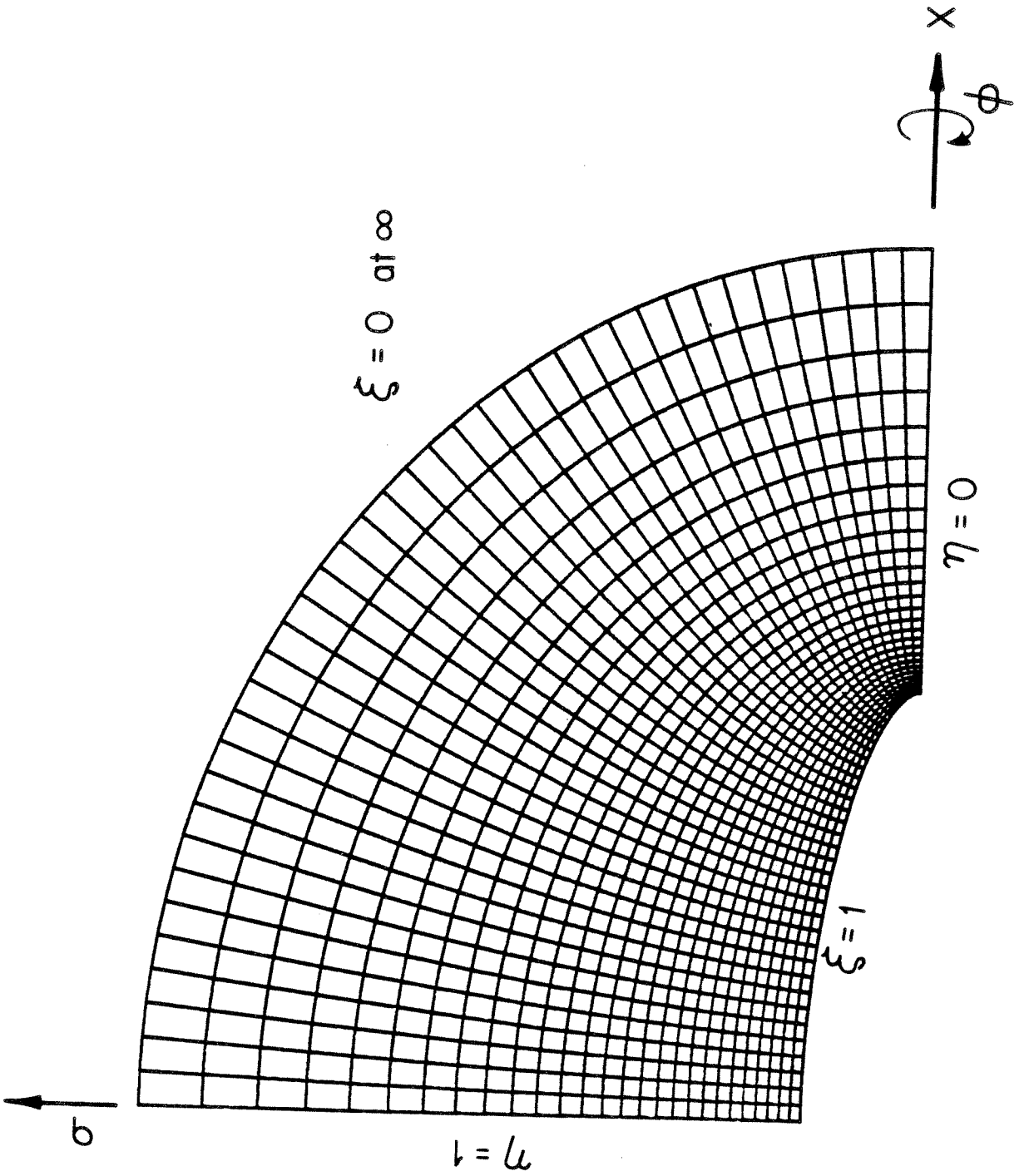

Figure 1

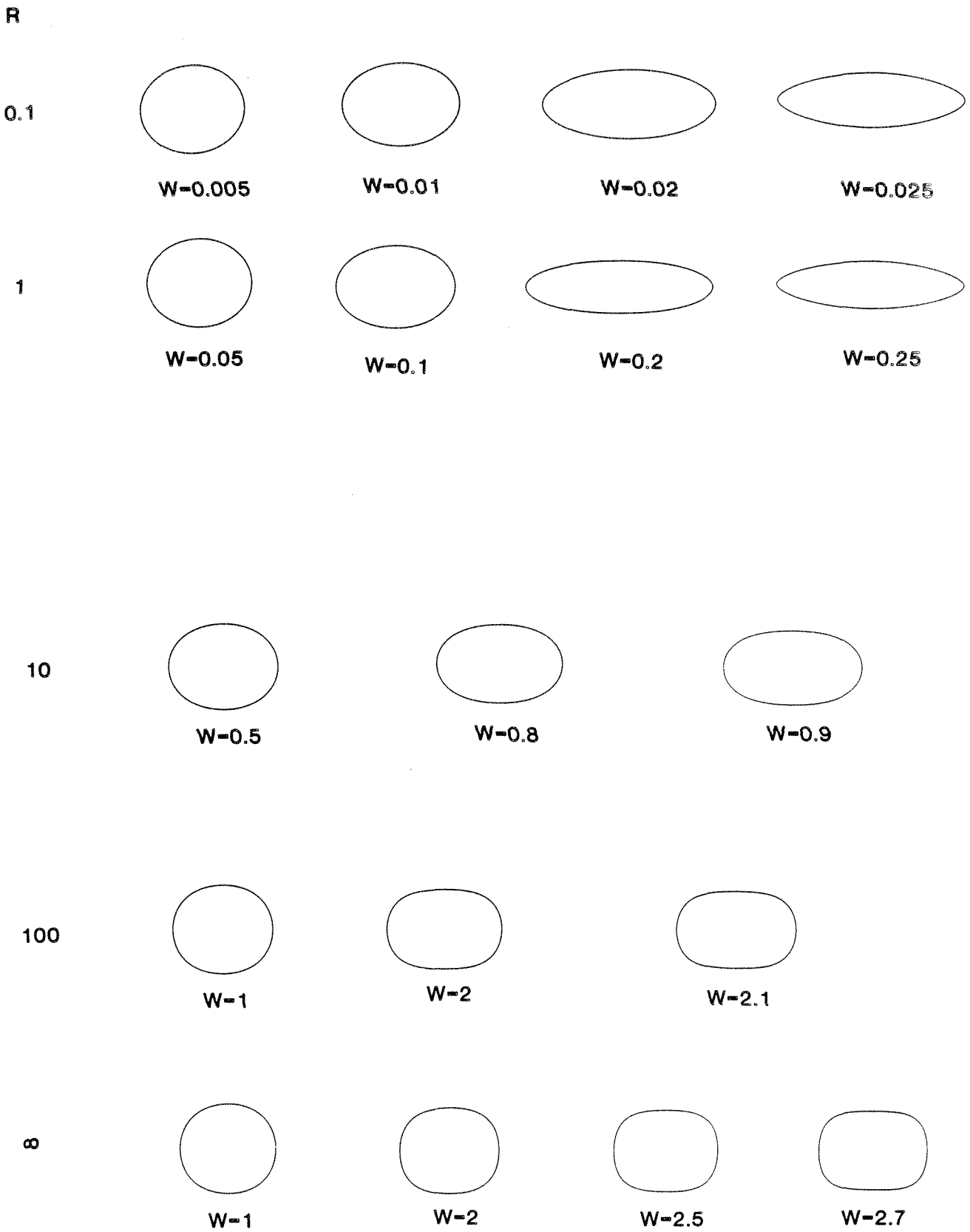
R
0.1
W=0.005
W=0.01
W=0.02
W=0.025
1
W=0.05
W=0.1
W=0.2
W=0.25
10
W=0.5
W=0.8
W=0.9
100
W=1
W=2
W=2.1
∞
W=1
W=2
W=2.5
W=2.7

Figure 2

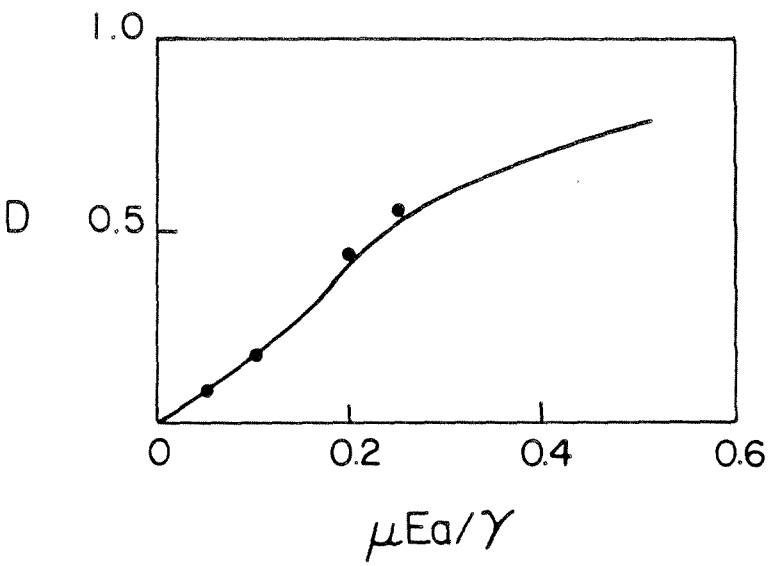

Figure 3